NTNU
Norwegian University of
Science and Technology

The relation between microstructure and thermoelectric properties in Ta-substituted A-site deficient $CaMnO_3$

Katinka Ervig Ledezma

Chemical Engineering and Biotechnology
Submission date: June 2017
Supervisor: Kjell Wiik, IMA
Co-supervisor: Sathya Prakash Singh, IMA
Mari-Ann Einarsrud, IMA

Norwegian University of Science and Technology
Department of Materials Science and Engineering

Declaration

I hereby declare that the work presented in this document has been performed independently and in accordance with rules and regulations of the Norwegian University of Science and Technology (NTNU).

Trondheim, 17 June 2017

Katinka Ervig Ledezma

Preface

The work described in this master's thesis has been performed at the Department of Materials Science and Engineering at the Norwegian University of Science and Technology (NTNU) during the spring 2017. The master's project is a part of the national coordinated THELMA project, within the Nano2021 program.

During this project work several people have provided me with their assistance and deserve my gratitude. First of all, I would like to thank my supervisor Professor Kjell Wiik for his time and guidance throughout this project. Your advice and valuable input have been most helpful. I would also like to show my gratitude to my co-supervisor PhD Sathya Prakash Singh. Your patience and help with the experimental work have been greatly appreciated. I would also like to thank you for conducting the thermoelectric measurements.

Further, I would like to thank PhD Nikola Kanas and Senior Engineer Eli Beate Larsen for operating the SPS with me, and all the technical staff at the Department of Materials Science and Engineering at NTNU for experimental help and apparatus training. Lastly, I would like to acknowledge my co-supervisor Professor Mari-Ann Einarsrud and the rest of the members of Inorganic Materials and Ceramics Research Group at the Department of Materials Science and Engineering for helpful advice during the semester.

Thank you all for your help.

K.E.L.

Abstract

Calcium manganite, $CaMnO_3$, is an n-type semiconductor with promising thermoelectric (TE) properties. However, for commercial applications the performance of the material, described by the thermoelectric figure of merit (zT), needs to be enhanced. In this study, Mn is substituted with 2% Ta (donor doping) to significantly increase the electrical conductivity, whereas the overall composition is Ca-deficient to promote exsolution of a secondary phase, resulting in the composition $Ca_{0.931}Mn_{0.98}Ta_{0.02}O_{3-\delta}$ (CMTO). This nanosized powder was spark plasma sintered (SPS) in its reduced rock-salt phase of CaO-MnO(ss) between 850°C and 1250°C, and then annealed in air at 1100°C to obtain the oxidized phase of CMTO with the secondary phase $CaMn_2O_4$ (marokite). Structural and thermoelectric properties of the material were investigated in order to determine correlations between material's microstructure, composition and TE properties.

Sintering resulted in dense samples with 98% of the theoretical density even at 850°C, and increasing grain size with increasing sintering temperature. After annealing in air, relative density of 95% was obtain. In addition, significant grain growth was observed in the samples sintered at the lowest temperatures, and estimated grain sizes were between 600 nm and 1.9 μm. In addition to the secondary phase, marokite, a third Ta-rich phase ($CaTa_2O_6$) was observed.

Increasing amount of marokite resulted in a significant reduction in electrical conductivity, as a result of marokite's insulating behaviour. Consequently, the absolute value of the Seebeck coefficient increased. The secondary phase lowered the thermal conductivity. However, high thermal conductivity was obtained as the grains were large. Nanosized grains enhance the phonon scattering at grain boundaries and a reduction of thermal conductivity with reduced grain size is anticipated. Due to grains in the micrometer range, this effect was not observed.

High thermal conductivity in combination with low electrical conductivity resulted in relatively low zT, with highest value of 0.028 at 900°C. From investigated samples, the one sintered at 850°C is most promising, and improved results are achievable if the amount of marokite is reduced and the annealing temperature lowered.

Sammendrag

$CaMnO_3$ er en n-halvleder med lovende termoelektriske (TE) egenskaper, men for kommersielt bruk må yteevnen til materialet, beskrevet med zT (thermoelectric figure of merit), forbedres. I dette arbeidet, er Mn substituert med 2% Ta (donordoping) for å betydelig øke den elektriske ledningsevnen, mens den totale sammensetningen er Ca-fattig for å fremme utfelling av sekundærfase. Den resulterende sammensetningen er dermed $Ca_{0.931}Mn_{0.98}Ta_{0.02}O_{3-\delta}$ (CMTO). Dette nanopulveret ble sintret ved bruk av "spark plasma sintering" (SPS) i dens reduserte fase CaO-MnO (ss) mellom 850°C og 1250°C, for så å bli varmebehandlet i luft ved 1100°C for å oppnå den oksiderte perovskittfasen CMTO med $CaMn_2O_4$ (marokitt) som sekundærfase. Struktur og termoelektriske egenskaper ble undersøkt for å forstå sammenhengen mellom materialets mikrostruktur, sammensetning og TE egenskaper.

Sintringen resulterte i prøver med høy tetthet, rundt 98% av teoretisk tetthet, selv ved laveste sintringstemperatur på 850°C. Kornstørrelsen økte med økende sintringstemperatur. Etter varmebehandling av prøvene i luft ble en relativ tetthet på 95% oppnådd. I tillegg oppstod betydelig kornvekst i prøvene som var sintret ved de laveste temperaturene, og kornstørrelser ble estimert til å være mellom 600 nm og 1.9 μm. I tillegg til sekundærfasen, marokitt, ble en tredje Ta-rik fase ($CaTa_2O_6$) observert.

Økende mengde sekundærfase resulterte i betydelig reduksjon av den elektriske ledningsevnen, noe som kommer av at marokitt er ikke-ledende. Følgelig økte Seebeck koeffisienten i absoluttverdi med mengde marokitt. Sekundærfasen senket den termiske ledningsevnen. Likevel var den oppnådde termiske ledningsevnen høy, som følge av store korn i materialet. Med korn i nanometer forventes det reduksjon av termisk ledningsevne med minkende kornstørrelse. På grunn av korn i micrometer ble dette ikke observert.

Høy termisk ledningsevne i kombinasjon med lav elektrisk ledningsevne resulterte i relativt lav zT, med høyeste verdi lik 0.028 ved 900°C. Av de undersøkte prøvene er den som er sintret ved 850°C den mest lovende for å øke zT, dersom mengden sekundærfase blir redusert og varmebehandlingstemperaturen senket.

Contents

1 | Introduction

1.1 Background

Pollutant emissions and global warming, combined with ever increasing energy demands are problematic issues for the society. Energy production from current technologies, particularly fossil fuels, have negative impact on the environment and their abundance is limited. This has led to increased activity in developing alternative renewable energy sources and to improve the energy conversion technologies.

A promising technology is thermoelectric (TE) devices, which provide us with the ability to directly convert heat into electricity. Heat is an abundant energy source and is emanated from various sources mostly in form of solar radiation, geothermal heat or waste heat. Actually, more than half of all the energy generated by mankind is lost as waste heat.[1] Because thermoelectric systems can harvest thermal energy for generating electrical power, they make it possible to utilize this waste heat, and therefore have the potential to enhance the sustainability of our energy demands.

The conventional design for TE devices, which is shown in Fig.1.1, consists of many thermoelectric couples, where each couple is made up of one n-type and one p-type thermoelectric material. The two semiconductors are electrically connected in series and thermally in parallel by sandwiching them between electrical insulators.[2] A thermoelectric generator uses heat flow across a temperature gradient to power an electric load through the external circuit. While the heat flow drives the electrical current, the temperature difference provides the voltage from the *Seebeck effect*.[3] As thermoelectric generators are solid state devices with no liquid fuel, no toxic gas emissions and no moving parts, they are silent, reliable and easily scalable for domestic

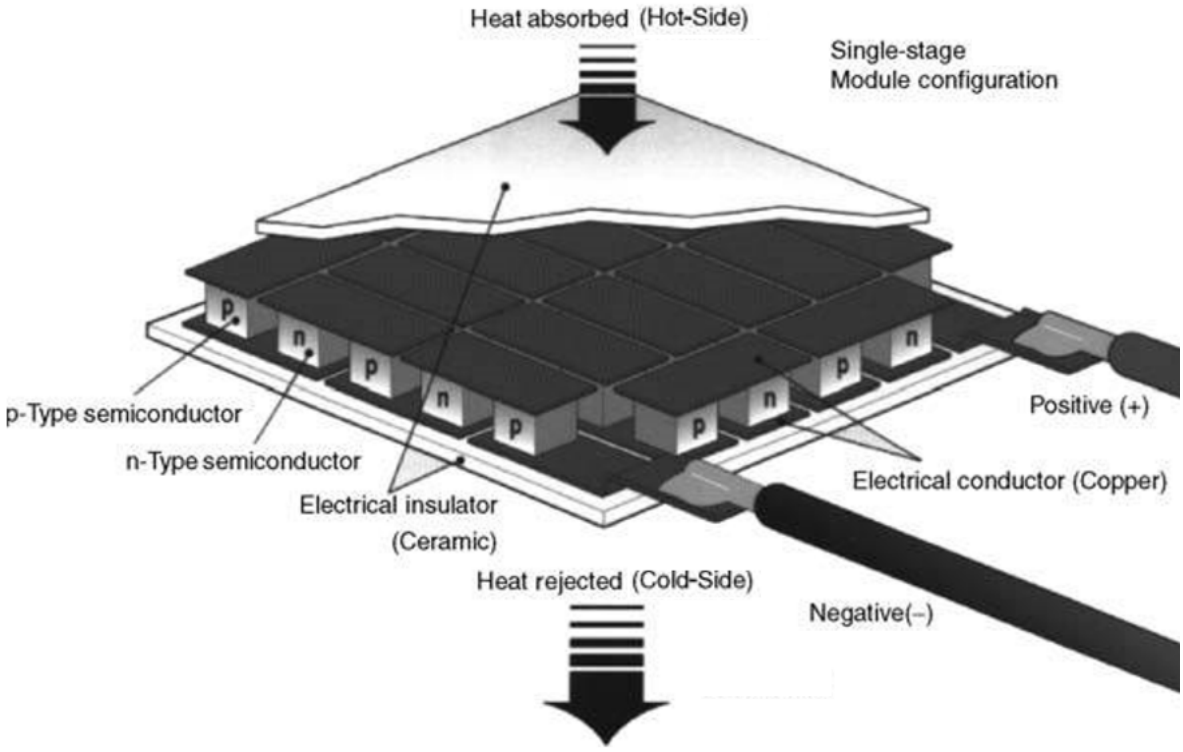

Figure 1.1: Thermoelectric device consisting of thermoelectric couples (n-type and p-type)[4].

use as well as for industrial applications[1].

However, to meet the role as the future energy production, TE devices need to be more efficient, as they currently have low efficiency compared to classical devices. In order to achieve this, efficient thermoelectric materials that are suitable for high-temperature applications are needed. The maximum efficiency of a TE material is determined by the dimensionless thermoelectric figure of merit, zT. zT comprises the electrical conductivity, σ, the Seebeck coefficient, S, the thermal conductivity, κ, and the absolute temperature, T, and is expressed as [2]:

$$zT = \frac{\sigma S^2 T}{\kappa} \tag{1.1}$$

This states that a thermoelectric material with high performance should exhibit a high σ, large S and low κ. The search for new promising TE materials, i.e. with high zT values, therefore relies on optimizing these interdependent properties.

Currently, there are many well developed state-of-the-art TE materials with high zT, but these are often toxic, unstable in air and expensive, which limit the usability. Thus, the main

focus now is to search for alternative materials, which are environmentally friendly, cheap and thermally and chemically stable in oxidizing atmosphere at high temperatures. For this reason, oxides as TE materials are of great interest. Fig.1.2 shows the advantages of oxides compared to state-of-the-art metal-based TE materials.

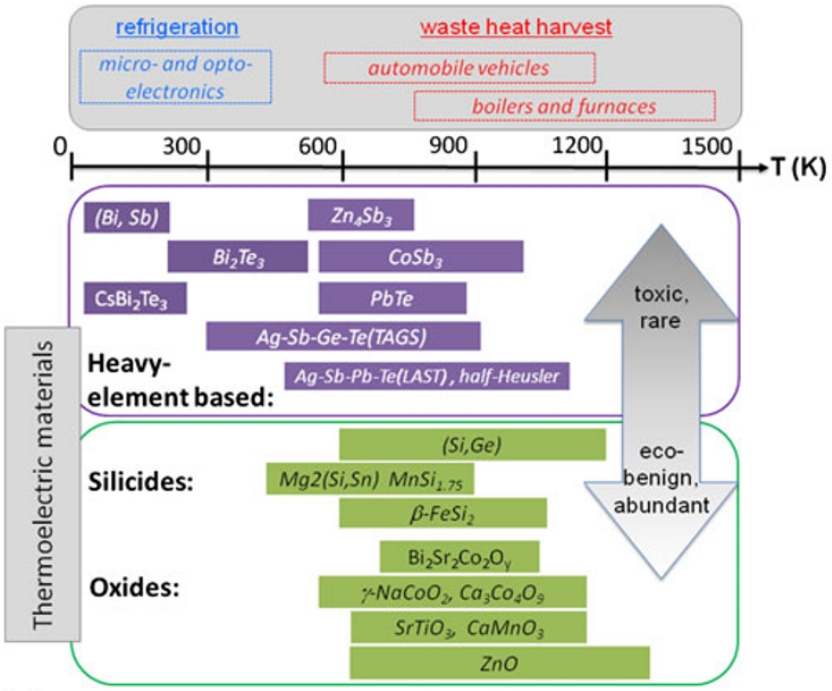

Figure 1.2: Schematic comparison of various thermoelectric (TE) materials for applications of waste heat harvest and refrigeration, in terms of the temperature range of operation and the abundance and environmental friendliness of constituent elements.[1]

One of the most promising n-type TE oxides is calcium manganite, $CaMnO_3$. In addition to the general advantages related to oxides, doped $CaMnO_3$ shows good thermoelectric properties with high electrical conductivity and reasonable high Seebeck coefficient. However, the thermal conductivity is too high, and lowering this, without affecting the electrical conductivity, is challenging.

1.2 Objectives

The focus of this master project is to characterize and improve the properties of the n-type thermoelectric oxide, $CaMnO_{3-\delta}$ substituted with tantalum (Ta). The goal is to enhance the thermoelectric properties, i.e. increase the thermoelectric figure of merit zT, by lowering the thermal conductivity. This can be achieved by increasing the scattering of heat carriers (phonon scattering) through different approaches: i) Reduce the grain size to increase the amount of grain boundaries, as they work as scattering centers. This is the reason the precursor powder used in this study is produced by spray pyrolysis, where the particle size becomes significantly smaller than those produced with conventional solid state method. ii) Substitute with a heavy element, such as Ta. In addition to contributing to the phonon scattering, it will also enhance the electrical conductivity. iii) Introduce a secondary phase to increase the amount of interfaces, by producing a A-site deficient material. Thus, the overall composition of the studied material is $Ca_{0.931}Mn_{0.98}Ta_{0.02}O_{3-\delta}$ (CMTO).

In this work, spark plasma sintering (SPS) will be used to promote sintering at moderate temperatures and short time, allowing a much better control of the resulting microstructure compared with traditional pressure-less densification. The main objective is therefore to produce well-defined micro (nano)- structures by spark plasma sintering and establish the correlation between structure and thermoelectric properties, such as thermal conductivity, electrical conductivity and Seebeck coefficient.

Both single-phase calcium manganite with rock-salt structure and perovskite CMTO with a secondary spinel-phase will be characterized with respect to density and porosity (Archimedes method), phase composition (XRD), crystallite size (XRD/Debye-Scherrer) and microstructure (SEM,EDS). Of particular interest is the resulting microstructure with focus on the nucleation, growth and distribution of the secondary phase. Finally, the thermoelectric properties will be assessed for some chosen samples with well-defined microstructure.

2 | Theory

2.1 Thermoelectric effects

2.1.1 Seebeck effect

In 1821, Thomas J. Seebeck discovered the phenomenon that is now known as the Seebeck effect. He observed that a circuit formed from two dissimilar conductive materials (metal or semiconductor) with the junctions kept at different temperatures generates an electric potential.[5]

When one end of the electric conductor is heated, a temperature difference and a temperature gradient from the cold end (T_c) to the hot end (T_h) of the conductor will be generated. The temperature gradient in the thermoelectric material causes a potential gradient. The charge carriers diffuse through the material from the hot to the cold side, leading to an electric diffusion current. In a n-type material, negative charges will build up at the cold side, as the charge carriers are electrons, while in a p-type material, positive charges, i.e. holes, will be established at the cold side.[6] The effect is illustrated in Fig.2.1.

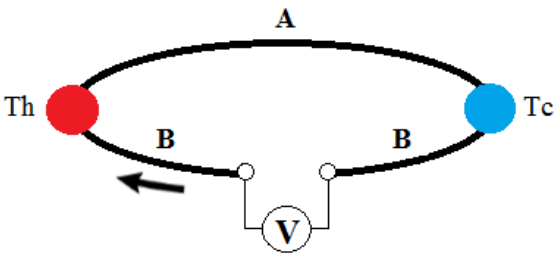

Figure 2.1: Illustration of the Seebeck effect between two dissimilar materials, A and B. The junctions are held at different temperatures, T_h>T_c.[7]. Arrow indicates the direction of the current.

The voltage generated due to the temperature difference is expressed by Eq. 2.1:

$$V = \int_{T_c}^{T_h} S(T)\, dT \tag{2.1}$$

where T_c and T_h are the temperatures at the cold and the hot side, respectively, and S is the Seebeck coefficient. The Seebeck coefficient is negative for n-type materials and positive for p-type materials, and can be expressed as [7]:

$$S = \frac{V}{(T_h - T_c)} = \frac{V}{\Delta T} \tag{2.2}$$

The principle of thermoelectric generators is based on the Seebeck effect. Two other thermal phenomenons give rise to the Seebeck effect; the Peltier and Thomson effects.

2.1.2 Peltier effect

In 1834, a second thermoelectric phenomenon was discovered by Jean Charles A. Peltier. This effect, called the Peltier effect, is the reversed situation of the Seebeck effect; if an external current is applied to a couple of dissimilar semiconductors, heat transport through the material will be induced. This causes cooling of one junction and heating of the other. The direction in which the current flows, determines whether the heat, Q, is released or absorbed. The heat is proportional to the electric current, I, and can be expressed as [5, 8]:

$$Q = \Pi \cdot I \tag{2.3}$$

where Π is the Peltier coefficient, and is defined as the ratio between Q and I.

2.1.3 Thomson effect

The last of the thermoelectric effects is the Thomson effect, recognized by W. Thomson. The effect describes the reversible heating (absorption of heat) or cooling (generation of heat) when there are both a flow of electric current and a temperature difference [8]. The rate of heat generation dQ is proportional to the temperature gradient and the applied current according to Eq. 2.4:

$$dQ = \beta I \, dT \tag{2.4}$$

where β is the Thomson coefficient.

2.1.4 Relations between the thermoelectric coefficients

By applying thermodynamics, Thomson also established a relationship between the Seebeck coefficient and the Peltier coefficient, and between the Seebeck coefficient and the Thomson coefficient [8, 9]:

$$\beta = T \cdot \frac{dS}{dT} \tag{2.5}$$

$$\Pi = S \cdot T \tag{2.6}$$

Eq. 2.5 and Eq. 2.6 are known as Kelvin relationships.

The Seebeck and the Peltier coefficients cannot be measured for a single material, therefore they have to be measured against reference materials. The Thomason cofficient on the other hand, can be measured directly from a single material, making it possible to calculate the Seebeck and the Peliter coefficients by the use of the Kelvin relations.[10]

2.2 Thermoelectric figure of merit

Thermoelectric devices allow for the direct conversion of heat into electrical energy, by applying heat on one side of the device. Thermoelectric generators enable this energy conversion based on the Seebeck effect, as shown in Fig.2.2. The heat will "push" electrons in the n-type material and holes in the p-type material from the hot side to the cold side. In effect, heat drives an electrical current, which can be used to perform work.

The maximum theoretical efficiency for conversion of heat transferred from hot temperature, T_h, to cold temperature, T_c, through a material with thermoelectric figure of merit, zT, is given by Eq.2.7, where η_{max} is called the power generation efficiency[2]:

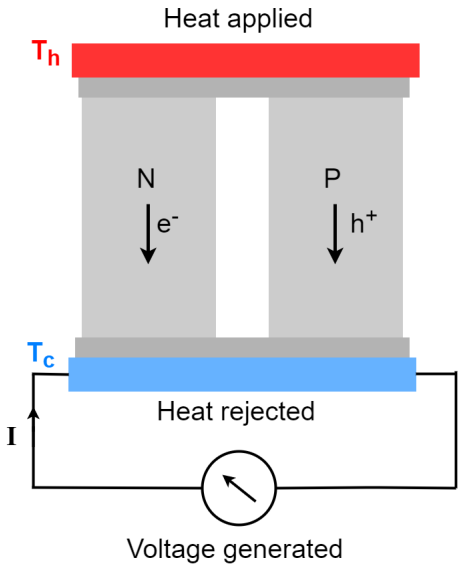

Figure 2.2: Illustration of thermoelectric generator based on the Seebeck effect. Based on figure in [11]

$$\eta_{max} = \frac{T_h - T_c}{T_h} \cdot \frac{\sqrt{1+zT}-1}{\sqrt{1+zT}-(T_c/T_h)} \tag{2.7}$$

The dimensionless thermoelectric figure of merit, zT, describes the performance of a TE material and provides a basis for comparing materials because it describes the relationship between the quantities determining the TE properties of a material[2]:

$$zT = \frac{\sigma S^2 T}{\kappa} \tag{2.8}$$

σ is the electrical conductivity, S is the Seebeck coefficient, κ is the thermal conductivity and T is the absolute temperature. σS^2 is often referred to as the power factor, PF.

It is desired to have as high zT as possible. As seen from Eq. 2.8, a large Seebeck coefficient, high electrical conductivity and a low thermal conductivity are required in order to maximize zT. The power factor should also be large, as it implies high zT. The reasons for these desired conditions are (i) the voltage generated by a thermoelectric material placed in a temperature gradient is related to the Seebeck coefficient, which therefore should be high, (ii) electrical current must pass through the thermoelectric material, so its electrical conductivity should be high to minimize the ohmic losses, and (iii) the thermal conductivity should be low in order to maintain a large temperature gradient.[2]

One of the challenges in increasing the figure of merit is that improvements of one property often are offset by changes in another property, as the three parameters comprising z all are functions of carrier concentration[7]. The relations will be described further in subsection 2.2.3.

2.2.1 Seebeck coefficient and electrical conductivity

The Seebeck coefficient, which sometimes is referred to as the thermopower, is defined as the relation between the induced voltage and the temperature difference, Eq.2.2. It can also be expressed as[3]:

$$S = \frac{8\pi^2 k_B^2}{3eh^2} m^* T \left(\frac{\pi}{3n}\right)^{\frac{3}{2}} \tag{2.9}$$

where k_B is Boltzmann's constant, e is the electron charge, h is Planck's constant, m^* is the effective carrier mass, T is the absolute temperature and n is the charge carrier concentration. As seen from this equation, the Seebeck coefficient decreases with increasing carrier concentration, and at constant temperature, n is the only variable.

In contrast to the Seebeck coefficient, the electrical conductivity increases with increasing carrier concentration [7]. It is derived from Ohm's law and is expressed as [12]:

$$\sigma = \frac{1}{\rho} = ne\mu \tag{2.10}$$

where ρ is the electrical resistivity, n is the carrier concentration, e is the electron charge and μ is the carrier mobility. Therefore, the electrical resistivity decreases with increasing carrier concentration.

The different dependencies of carrier concentration make it difficult to optimize the power factor, σS^2, thus the best compromise between large S and high σ needs to be pursued to reach a high PF.

2.2.2 Thermal conductivity

While the Seebeck coefficient and the electrical conductivity should be high to achieve a high zT, the thermal conductivity, κ, should be low[2]. Heat is conducted through a solid by electron

conduction and lattice phonon conduction. Hence, there are two contributions to the thermal conductivity; a lattice component, κ_l, and an electronic component, κ_{el}. This can be expressed by the following equation [13]:

$$\kappa = \kappa_l + \kappa_{el} \tag{2.11}$$

The electronic thermal conductivity depends on the carrier concentration and is related directly to the electronic conductivity, σ, according to Wiedemann-Franz law [12]:

$$\kappa_{el} = \left(\frac{\pi^2 k_B^2}{3e^2}\right)\sigma T = L\sigma T \tag{2.12}$$

where k_B is Boltzmann's constant, e is the charge of an electron, and L is the Lorenz number. This relationship shows that an improvement in electronic conductivity leads to an increase in the electronic contribution to the thermal conductivity.

The lattice thermal conductivity, on the other hand, is independent of the carrier concentration and can be lowered without decreasing the electrical conduction. Thus, materials in which thermal conduction is dominated by the lattice phonon component are more promising for thermoelectric application. The heat conduction process in insulators is dominated by the lattice phonon conduction, while this becomes less significant the more metallic the material is, as seen from figure 2.3[7].

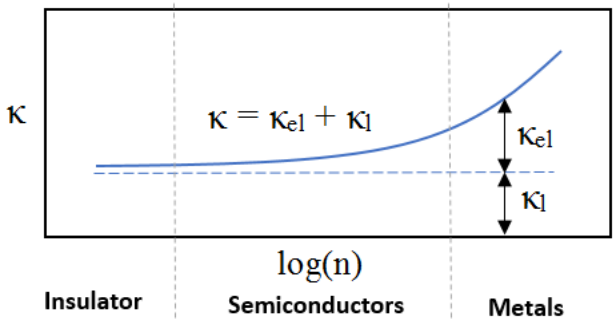

Figure 2.3: Thermal conductivity dependence on carrier concentration, n. The illustration is based on a figure in reference [11].

The lattice thermal conductivity corresponds to the propagation of phonons in the three

space dimensions through the crystal lattice and is defined as [12]:

$$\kappa_l = \frac{1}{3} C_v \, v \, l \tag{2.13}$$

where C_v is the heat capacity per unit volume, v is the average phonon velocity, and l is the phonon mean free path, which is defined as the average distance a phonon travels before colliding with another particle[12]. How κ_l evolves with temperature, depends on the dominating interactions occurring in the lattice. At high temperatures, the collisions between phonons dominate, which is a phenomenon known as the Umklapp process. The thermal conductivity is proportional to 1/T because at high temperatures the total number of excited phonons is proportional to T, and the collision frequency of a given phonon should be proportional to the number of phonons with which it can collide. Hence, $l \, \alpha$ 1/T.[12] At low temperatures, the Umklapp process becomes ineffective in limiting the thermal conductivity, and the phonon mean free path is limited by grain size and defect concentration. This means that grain boundary scattering and mass defect scattering, where a phonon hits an impurity within the system, are the dominating phonon scattering mechanisms that lowers the thermal conductivity. In addition, at low temperatures κ_l is dominated by C_v, which is proportional to T^3, resulting in a variation of the thermal conductivity with T^3.[12]

2.2.3 Relations between the thermoelectric properties

As mentioned, it is difficult to increase the figure of merit, because by changing one of the properties, another one will be affected as well. This is due to the fact that the electrical conductivity, the Seebeck coefficient and the thermal conductivity of the material are all functions of carrier concentration, as illustrated in Fig. 2.4.

As seen from the figure, insulators have large Seebeck coefficients, low thermal conductivity and low electrical conductivity due to low carrier concentration. Metals are good electrical conductors but represent small Seebeck coefficients, resulting in low power factors. Besides, the thermal conductivity is high. Evidently, figure of merit optimizes at carrier concentration which corresponds to semiconductors. Consequently, semiconductors are the best options as TE materials. The peak in power factor typically occurs where the carrier density is between 10^{19} and

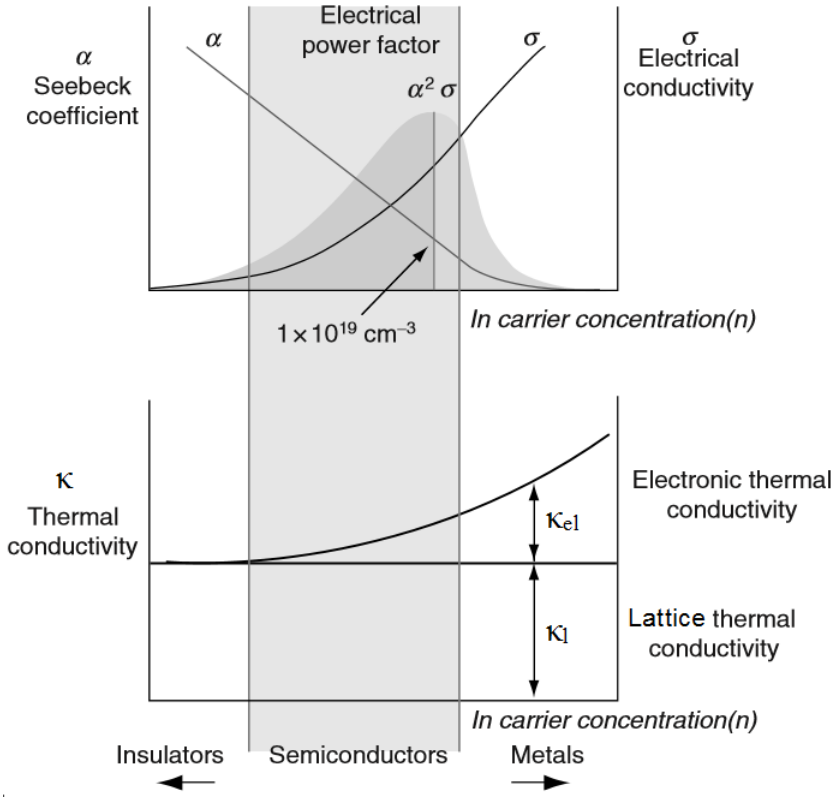

Figure 2.4: Schematic dependence of electrical conductivity, Seebeck coefficient, power factor and thermal conductivity on concentration of free carriers. [7]

10^{21} carriers per cm^3 (depending on the material system), which corresponds to concentrations found in doped semiconductors[3]. Due to these interrelated material properties, there will always be a trade-off when designing new TE materials, and optimization is fundamental in this field.

Ideally, the TE materials should have lattice thermal conductivity close to those of amorphous materials, i.e. glass, and electrical conductivity as in crystalline material, as this would maximize zT. This concept is called "phonon glass electron crystal".[14] One strategy to improve the figure of merit is therefore to lower the lattice thermal conductivity while keeping the electronic properties undisturbed. By replacing the thermal conductivity κ with the electronic and the lattice contribution and applying Wiedemann-Franz law in Eq.2.8, the figure of merit can also be expressed by[9]:

$$zT = \frac{\sigma S^2 T}{LT\sigma + \kappa_l} = \frac{S^2}{L} \cdot \frac{\kappa_{el}}{\kappa_{el} + \kappa_l} \tag{2.14}$$

This emphasizes that zT can be enhanced when $\kappa_l/\kappa_{el} << 1$. How to reduce the lattice thermal conductivity will be discussed further in the end of Section 2.3.3.

2.3 Thermoelectric materials

2.3.1 State-of-the-art materials

Currently, the materials that have been shown to have the best thermoelectric properties are tellurium-, antimony- and selenium- based compounds[2, 7]. These compounds in combination with bismuth represents good thermoelectric figure of merit, zT, at low temperatures (T < 450 K). In the intermediate temperature range (T < 850 K), materials based on lead telluride have highest zT, while at the highest temperatures (T > 900 K) silicon germanium (SiGe) alloys are applied, both as n-type and p-type materials.[7] Figure 2.5 presents zT of different state-of-the-art materials as function of temperature. It shows that several conventional p-type materials exhibits zT above one, which is generally considered to be needed for practical applications[2]. Most n-type materials, however, do not exceed unity, which is an important drawback.

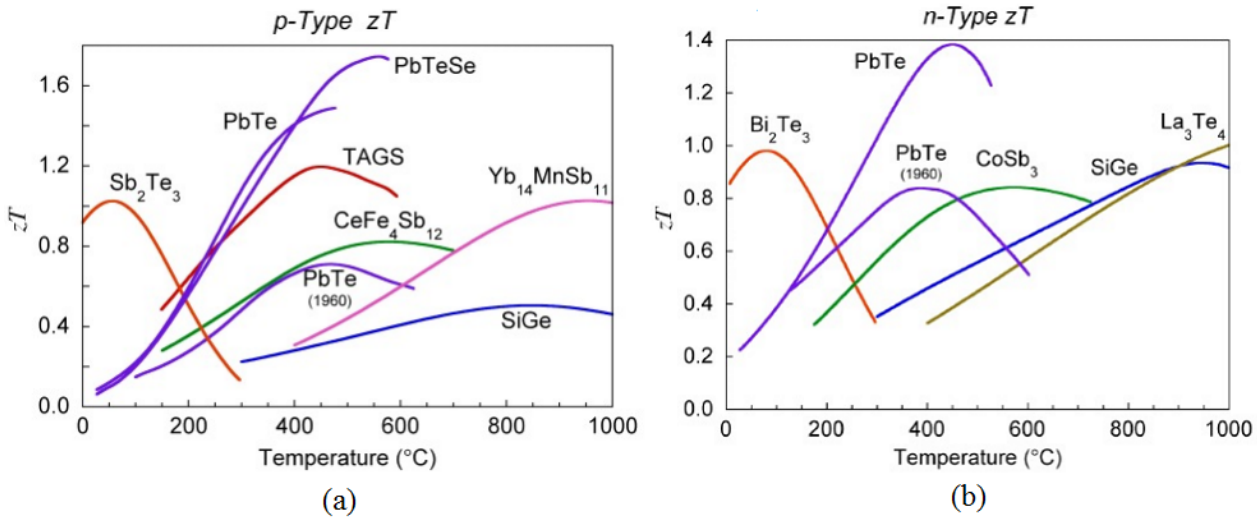

Figure 2.5: Figure of merit zT of some conventional thermoelectric materials. a) p-type materials. b) n-type materials. (TAGS: $((AgSbTe_2)_{1-x}(GeTe)_x)$) [15]

Besides, the established TE materials have poor stability at high temperatures and oxidizing conditions, combined with low abundance and high cost. The toxicity of these compounds is

also an issue.[11] These are problems related to most conventional materials used in applications, hence the motivation for finding alternative materials, such as thermoelectric oxides.

2.3.2 Thermoelectric oxides

Oxides are investigated as potential thermoelectric materials, both as n-type and p-type materials. Despite considerable scientific activity in the field and many promising candidates, the reported values for zT are still lower than most state-of-the-art materials.[16]

The highest figure of merit among oxides is reported for p-type conducting materials. So far, layered cobaltite compounds are the p-type oxides with the best thermoelectric properties[2], where some of them exhibit zT just above one. This place them very close to the zT-value of the state-of-art materials. zT for n-type oxides, however, is significantly lower, making it challenging to develop an efficient oxide based TE device. This difference in zT between p-type and n-type oxides are illustrated in figure 2.6.

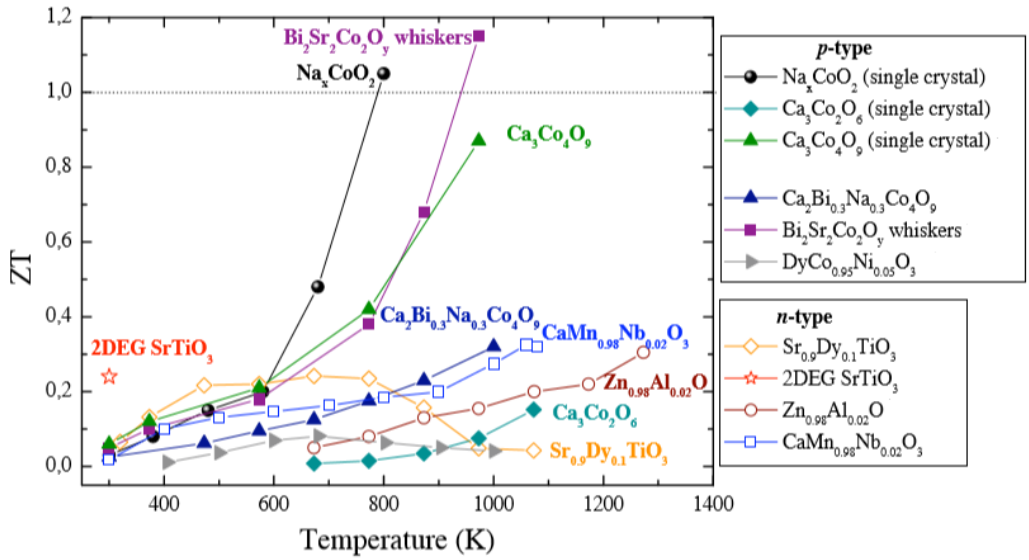

Figure 2.6: Figure of merit zT of some p-type and n-type oxides [9].

In spite of relatively low figure of merit, thermoelectric oxides have many advantages. Oxides are chemically and thermally stable under oxidizing conditions even at high temperatures, making them more usable in industry because it allows for a large temperature gradient to be applied across the materials in air. This leads to a high Carnot efficiency that somewhat compensates the low zT[1]. TE oxides are also cost efficient and non-toxic compared to conventional

TE materials, and they have minimal negative impact on the environment.[11] Additionally, oxides are featured by their chemical versatility and structural intricacy. This offers a great flexibility of structural and compositional tailoring.[1] Oxides also have some drawbacks that result in low zT. First, the large electronegativity difference among the constituent elements leads to more ionic bonding, strong tendency for carrier localization, and strong scattering of carriers by optical phonons. Second, the Seebeck coefficient is often found to be small, and third, the thermal conductivity is high. A small S is due to the cancellation between the electron and hole band contributions, while the large bonding energy and the small mass of oxygen lead to a high velocity of sound and therefore high κ.[1]

2.3.3 Calcium Manganite

$CaMnO_3$-based perovskites are some of the most promising n-type semiconductors, and as oxides they have many advantages compared to conventional TE materials. At oxidizing conditions (air), $CaMnO_3$ is a line compound, as seen from Fig.2.7(a), presenting the phase relation in the Ca–Mn–O system. A small deviation from a Ca–Mn–ratio of one causes formation of new phases. In Ca-deficient $CaMnO_3$ at high temperatures, this secondary phase is marokite ($CaMn_2O_4$). At reducing conditions there is complete solid solution between CaO and MnO at all mole fractions CaO, as shown in Fig.2.7(b).

Crystal structure

$CaMnO_3$ has the perovskite structure. The perovskite structure has the general formula ABO_3, where A is typically a rare-earth, alkaline earth or alkali cations and B represents a 3d, 4d or 5d transition metal. Many of the perovskites are cubic and are referred to as ideal perovskites. However, the perovskite structure often distorts from the ideal cubic structure to other crystal forms such as tetragonal, orthorhombic and rhombohedral, where orthorhombic is the most common symmetry. In case of calcium manganite, the structure depends on the temperature, as shown in Tab.2.1.

The orthorhombic unit cell of $CaMnO_3$ perovskite, space group Pnma, is illustrated in Fig.2.8 and shows that each Mn^{4+}-ion is coordinated by six oxygen anions, forming corner-sharing MnO_6 octahedra with Ca-cations in between.

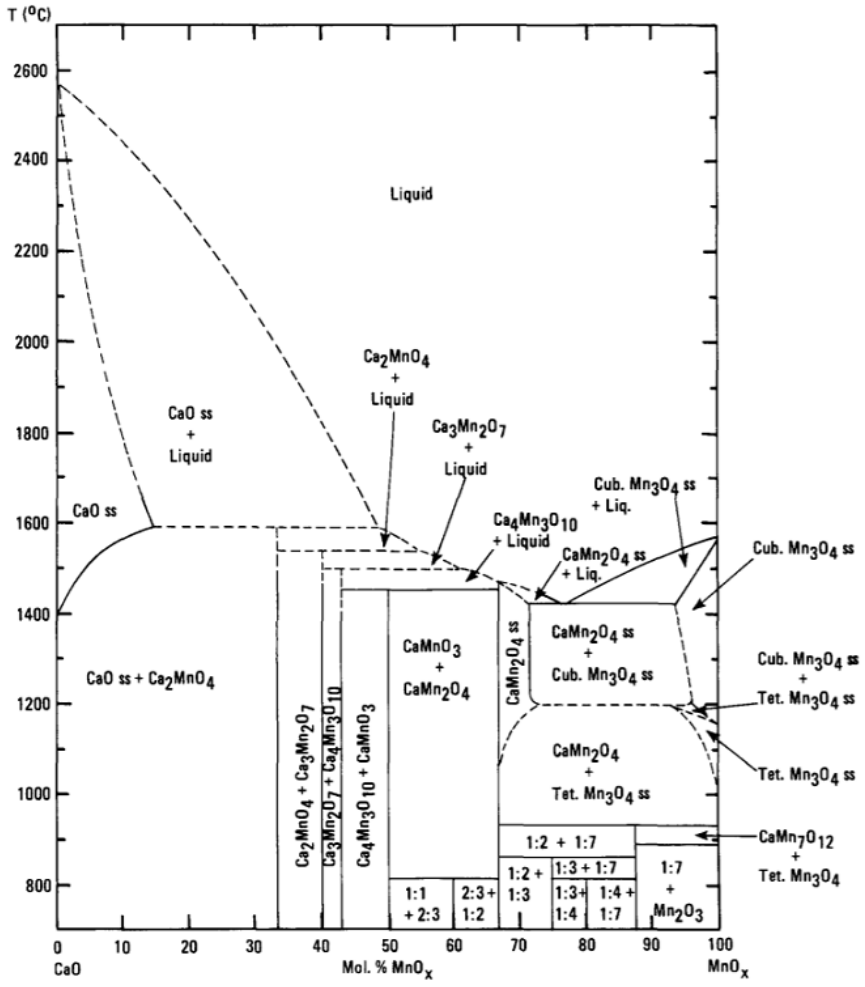

(a)

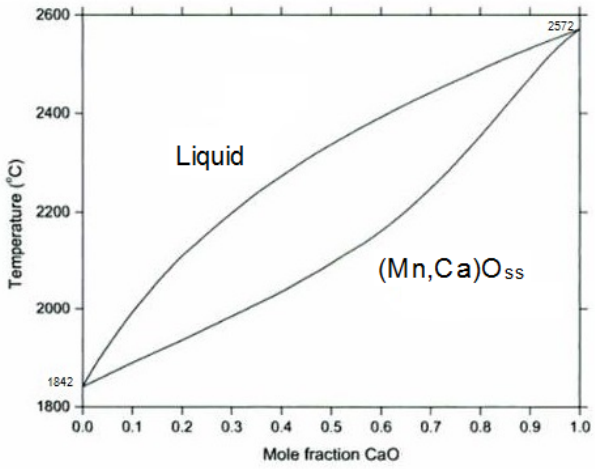

(b)

Figure 2.7: (a) Phase relations for the Ca–Mn–O system in air[17]. (b) CaO–MnO phase diagram in reducing atmosphere.[18]

Table 2.1: Phase transitions in $CaMnO_{3-\delta}$[19].

Structure	Temp. range [°C]
Cubic	> 913
Tetragonal	896–913
Orthorhombic	< 896

Even though perovskites are not initially strong potential TE materials, as they are normally good insulators with high Seebeck coefficients[20], good TE properties are achievable because of the versatile and flexible crystal structure. In the perovskite family, the metal ions accommodate a variable oxidation state (Mn^{4+} and Mn^{3+} in $CaMnO_{3-\delta}$) and the oxygen sublattice can have a large amount of vacancies[21]. Thus, properties can be modified and fined-tuned by introducing cation substitution on A or B site or change in oxygen content.[22] Due to the possibility of tailoring the functional properties, perovskite is one of the most important structures to advanced technology applications[23].

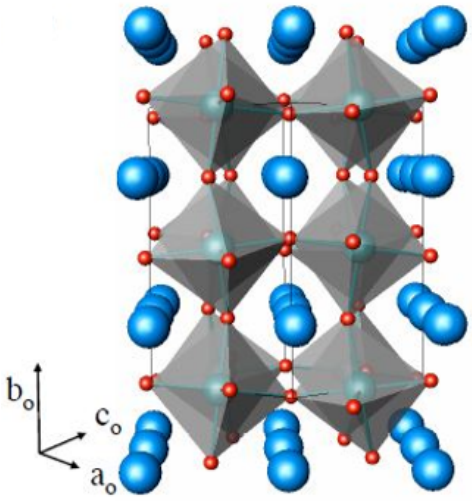

Figure 2.8: Schematic representation of the orthorhombic crystal structure of $CaMnO_3$ (Pnma). Blue spheres corresponds to Ca-sites, turquoise spheres to Mn-sites, and red spheres to oxygen. Mn^{4+}-ion is coordinated by six oxygen anions, forming corner-sharing MnO_6 octahedra with Ca-cations in between.[9]

Defect chemistry and conduction mechanism in $CaMnO_{3-\delta}$

In ionic crystals such as oxides, conduction electrons polarize the surrounding crystal lattice by strong electron-lattice interactions, localizing themselves at the lattice point and inducing

lattice distortion. Such localized electrons are called small polarons, and travel by a hopping mechanism accompanied by the surrounding lattice distortion. It is reported that the conduction mechanism in $CaMnO_{3-\delta}$ is small polaron hopping with thermally activated carrier mobility.[11] In Mn^{3+}/Mn^{4+} mixed-valence manganates, such as $CaMnO_{3-\delta}$, the hopping mechanism can be described as a simultaneous transfer of an electron from Mn^{3+}-site to an oxygen anion, and an electron from the oxygen anion to the Mn^{4+}-site[9]. The concentration of Mn^{3+} increases with increasing oxygen vacancy concentration, δ, in order to maintain charge neutrality, thus leading to increase in electrical conductivity.[16]

The defect properties of $CaMnO_{3-\delta}$ can be described by two chemical reactions (in Kröger-Vink notation):

$$\frac{1}{2}O_{2\ (g)} + V_{\ddot{o}} + 2Mn'_{Mn} = O_o^x + 2Mn_{Mn}^x \tag{2.15}$$

$$2Mn_{Mn}^x = Mn'_{Mn} + Mn^{\cdot}_{Mn} \tag{2.16}$$

where the first reaction corresponds to the filling of oxygen vacancies accompanied by oxidation of Mn-site, and the second reaction is the thermal excitation of electronic charge carriers across the band-gap.[16] As seen from these equations, removal of an oxygen atom results in an oxygen vacancy($V_{\ddot{o}}$) and two free electrons, denoted as $2Mn'_{Mn}$. This suggests that oxygen deficiency might be desired as it will increase the mobility and the charge carrier concentration. However, after the threshold of δ=0.25 the conductivity decreases due to lack of charge neutrality with so many free charge carriers[16].

The oxygen stoichiometry will also affect the structure of the perovskite, and it becomes more orthorhombic as δ increases. When the Mn^{4+} content increases and δ decreases, the structural distortion decreases and a more cubic structure is obtained.[24]

Schrade *et al.*[16] studied oxygen nonstoichiometry, and showed that δ increases with increasing temperature, and decreases with increasing pO_2 at constant temperature. He also stated that even when measuring in air, oxygen vacancies will form in $CaMnO_{3-\delta}$ and lead to a significant variation in thermoelectric properties at high temperature. In addition to affecting the electronic properties, oxygen vacancies affect the bulk of the material leading to an expansion of the crystal lattice, so-called chemical expansion.

Thermoelectric properties

The electrical conductivity and the Seebeck coefficient depend on the charge carrier concentration, which in this case is affected by oxygen stoichiometry, δ. For each oxygen that is removed from the lattice in a reducing atmosphere, two charge carriers will be introduced to the sample and the charge carrier concentration increases. This means that the Seebeck coefficient decreases with increasing δ, while the electrical conductivity increases. In addition, it is observed that the Seebeck coefficient decreases in absolute value and electrical conductivity increases as the temperature increases.[16]

While bulk electron-doped $CaMnO_3$ has fairly high PF values, the zT values are low. This is primarily due to high thermal conductivity[1, 14]. As presented in Section 2.2.2, the thermal conductivity is defined as the sum of a lattice component (κ_l) and an electronic component (κ_{el}). In oxide materials κ_l dominates, because phonons are the predominant heat carriers. For some doped calcium manganite compounds it is reported a κ_l of 80-95% of the total κ[22, 25]. Therefore, it is necessary to lower the lattice heat conduction in order to reduce the thermal conductivity and enhance the figure of merit of $CaMnO_3$-based compounds.

Doping, on either site, will also affect the figure of merit, and is a normal approach to enhance the thermoelectric properties of materials. While undoped $CaMnO_3$ is a poor n-type semiconductor, electron doped $CaMnO_{3-\delta}$ is very promising. The most common substituents for $CaMnO_3$ are yttrium, niobium, samarium and lanthanum[2], but ytterbium[2], tungsten[26] and tantalum[27, 25] are also studied. Substitution of cations has been found to reduce the electrical resistivity[28, 27], but the resulting higher carrier concentration affects the Seebeck coefficient adversely, and the best compromise for reaching a high power factor needs to be pursued.

A study of several lanthanide dopants summarizes some reported figure of merits of doped $CaMnO_3$ in Fig.2.9[2]. Another study, by Bocher *et al.*[22], reports zT=0.32 for $CaMnO_{3-\delta}$ doped with 2% Nb on Mn-site, which is the highest value obtained for $CaMnO_3$.

Donor doping of $CaMnO_3$ on Mn-site introduces surplus electrons to the material. As Mn in the structure have the ability to change oxidation sate from +4 to +3, the additional charge of the substituent is compensated by changing the ratio of Mn^{3+}/Mn^{4+} [29]. Mn^{3+} can then be utilized

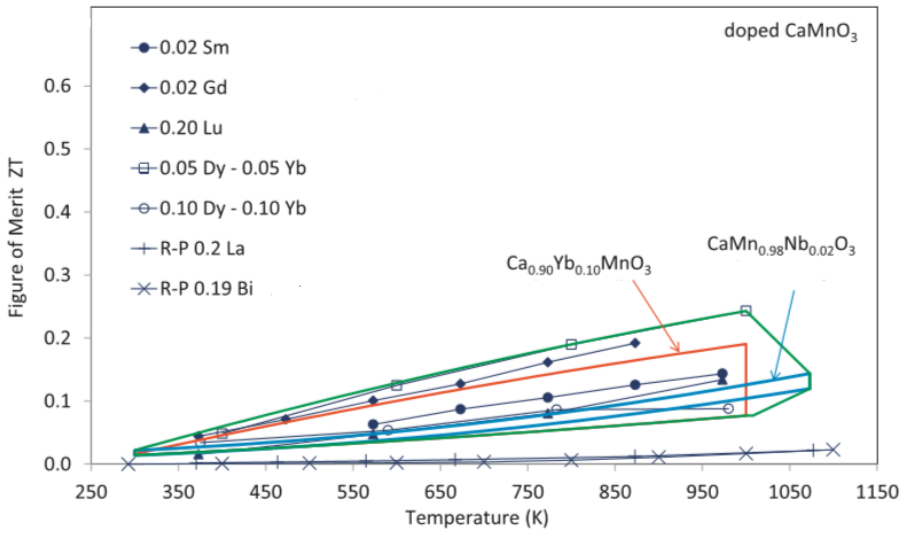

Figure 2.9: Figure of merit, zT, for doped $CaMnO_3$ [2].

as an electronic conduction center in its location by temporarily going back to Mn^{4+}, before it receives an electron again and transfers to Mn^{3+} once more. It is reported that introduction of a pentavalent cation, such as Nb^{5+} and Ta^{5+}, generates Mn^{3+} cations in the Mn^{4+} matrix and increases the electrical conductivity.[22]

Phonon scattering agents - substituents and structuring

As already stated, the lattice component of the thermal conductivity must be reduced in order to lower the total thermal conductivity in $CaMnO_3$. This can be achieved through mechanisms based on phonon scattering.

One strategy is donor doping, as presented above. In addition to increase the electrical conductivity, substitution of cations lowers the unfavorably high thermal conductivity because the substituent provide mass difference. Mass difference creates inharmonious lattice vibrations, which can suppress phonon transport and hence reduce the lattice thermal conductivity.[29]. Imperfections, such as impurities, play an important role in suppressing phonon transport especially at low temperatures[30]. By substitution on Mn-site in $CaMnO_3$, the introduced atom should be large and heavy, with oxidation state higher then that of Mn, i.e. hexavalent or pentavalent atoms.[14]

Another approach is structuring, where a material with grains of nanosize is being synthesized. By increasing the number of grain boundaries, the phonon scattering at the disordered

boundaries is enhanced. In general, the phonon mean free path cannot be shorter than the average inter-atomic spacing, but nanostructured material such as nanoparticles, nanowires or superlattices can shorten the phonon mean free path when the grain size is in the range of l, i.e. in the nanometer scale. This lowers the lattice thermal conductivity as l dominates the κ_l at high temperatures (Eq.(2.13)). Thus, nanocrystalline materials have lower thermal conductivity compared to conventional bulk materials. The effect of grain boundary scattering is reported by several studies on different ceramics[30, 31, 32, 33, 34, 35]. Fig.2.10, reported by Wang *et al.*[30], shows effective thermal conductivity of $SrTiO_3$ polycrystalline ceramic as a function of temperature, and illustrates how nanograins exhibit significantly lower thermal conductivity than bulk crystals.

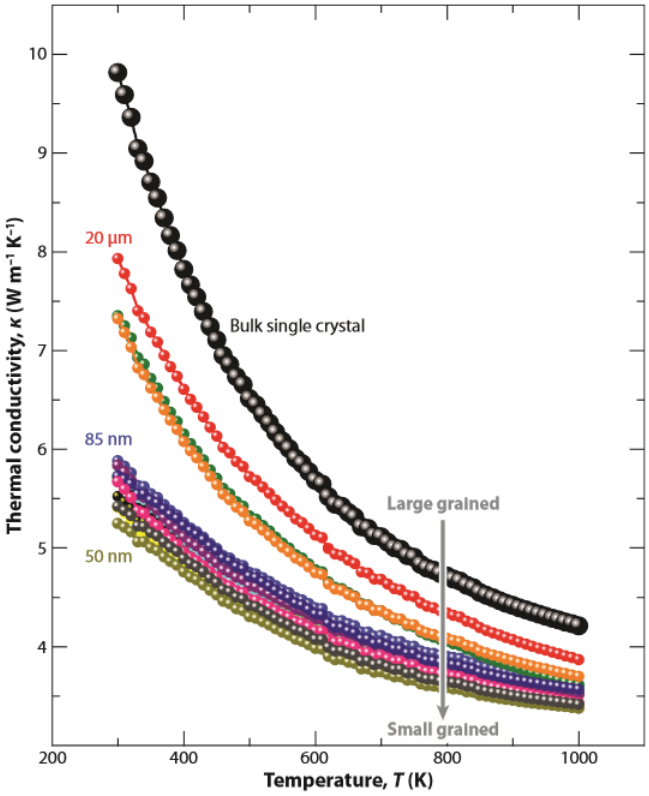

Figure 2.10: Effective thermal conductivity of $SrTiO_3$ polycrystalline ceramic as a function of temperature. The average grain sizes of some representative samples are shown to the left of the corresponding curves.[30].

Phonons can additionally be scattered by interfaces of different phases. Introducing suitable precipitates in the matrix, preferably in nanoscale, is therefore also a part of the structuring approach. The effect of secondary phase segregation is proposed to reduce the thermal con-

ductivity by creating more scattering centres due to difference in crystal structures. This means variation in inter-atomic spacing, which can scatter phonons with phonon mean free paths of multiple lengths.[36, 31] Hence, a substituted material with nanosized grains and a secondary phase of nanograins would be ideal to lower thermal conductivity.

CMTO

In CMTO, $CaMnO_{3-\delta}$ is substituted with tantalum (Ta) on Mn-site, resulting in electron doping. Ta substitution influences the electrical conductivity mainly in two aspects: First, it enhances the conductivity, as it increases the charge carrier concentration, as Ta^{5+} generates Mn^{3+} cations in the Mn^{4+} matrix according to $CaMn^{4+}_{1-2x}Mn^{3+}_{x}Ta^{5+}O_3$[9]. Second, it introduces scattering centers in conducting plane. At low doping level, the change of carrier concentration dominates the conducting behavior, but at high doping level, strong scattering may dominate, and the electron doping becomes less effective.[27] To avoid the latter case, the Ta doping in CMTO is in this work kept at 2%. Fig.2.11 presents electrical conductivity as a function of temperature of stoichiometric $CaMnO_3$ doped with 2% Ta and undoped $CaMnO_3$, and shows that the substitution of Ta significantly increases the conductivity.[37] This effect is reported in several studies[25, 27, 29].

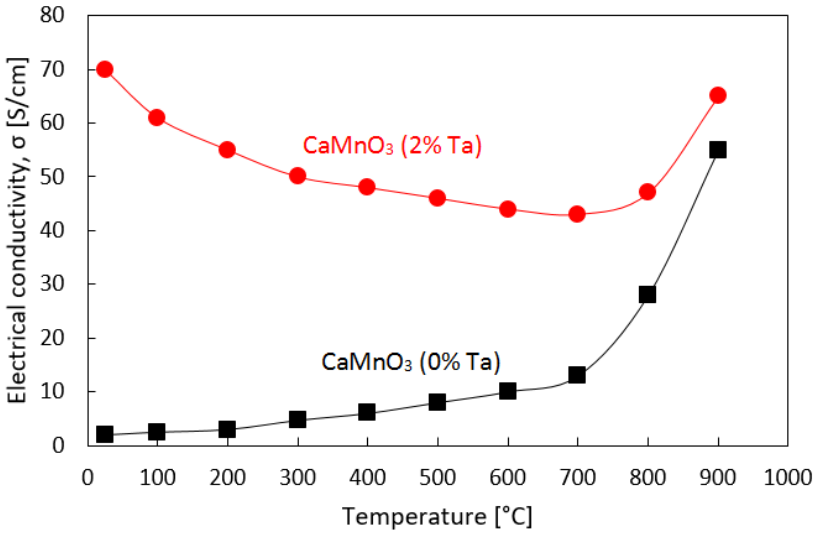

Figure 2.11: Electrical conductivity, σ, as a function of temperature. Undoped CMO vs. CMO substituted with 2% Ta.[37]

Substitution of Ta will in addition reduce the thermal conductivity. By substitution on Mn-site by using cations with oxidation state greater than four, the phonon propagation will be

limited[14]. Ta, a heavy element with oxidation state +5, is therefore a good substituent.

As secondary phases also contribute to the reduction of the thermal conductivity, 10 vol% of marokite ($CaMn_2O_4$) is introduced in the calcium manganite in this work. By studying the phase diagram in Fig. 2.7, it can be calculated that Ca-deficiency with a stoichiometry of 0.931 corresponds to 10 vol% marokite. This gives the total stoichiometry $Ca_{0.931}Mn_{0.98}Ta_{0.02}O_{3-\delta}$, when the material is substituted with Ta. A previous study on this composition achieved a zT of 0.12[25].

$\mathbf{CaMn_2O_4}$

With calcium deficient $CaMnO_3$ at oxidizing conditions, two phases will be present: the main phase perovskite $CaMnO_3$ and a secondary spinel phase $CaMn_2O_4$, known as marokite. This is seen in the phase diagram in Fig.2.7 above ≈820°C and with MnO content between 50 and ≈66%.

In marokite, illustrated in Fig.2.12, manganese is octahedrally coordinated with MnO_6 octahedra sharing edges and corners. The three-dimensional network of octahedra provides 8-coordinated sites for the larger calcium atoms. There is a high degree of Jahn-Teller distortion of MnO_6 octahedra, resulting in a distorted spinel structure with space group Pbcm, and not the cubic structure which is more common in AB_2O_4 compounds.[38]

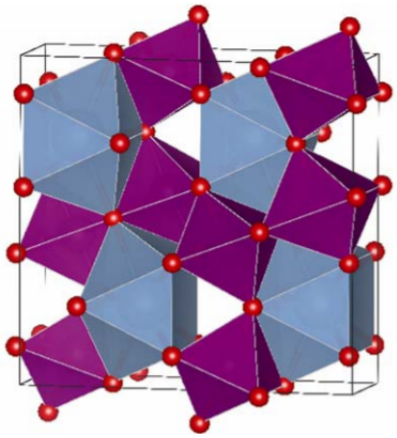

Figure 2.12: Structure of marokite, $CaMn_2O_4$. 6-fold coordinated Mn^{3+} and 8-fold coordinated Ca^{2+} is represented with violet octahedra and grey polyhedra, respectively [38].

Marokite is composed entirely of Mn^{3+} ions rather than a mix of Mn^{3+} and Mn^{4+} as in $CaMnO_{3-\delta}$, resulting in high electrical resistivity. As shown in Fig.2.13(a), the material shows

insulating behavior below 600°C, according to a study by Singh[37]. Insulating behavior at room temperature is supported by White *et al.*[39]. Fig.2.13(b) shows the thermal conductivity, which is between 3.2 and 2.65 $Wm^{-1}K^{-1}$. The theroetical density of marokite is 4.68 g/cm^3[40].

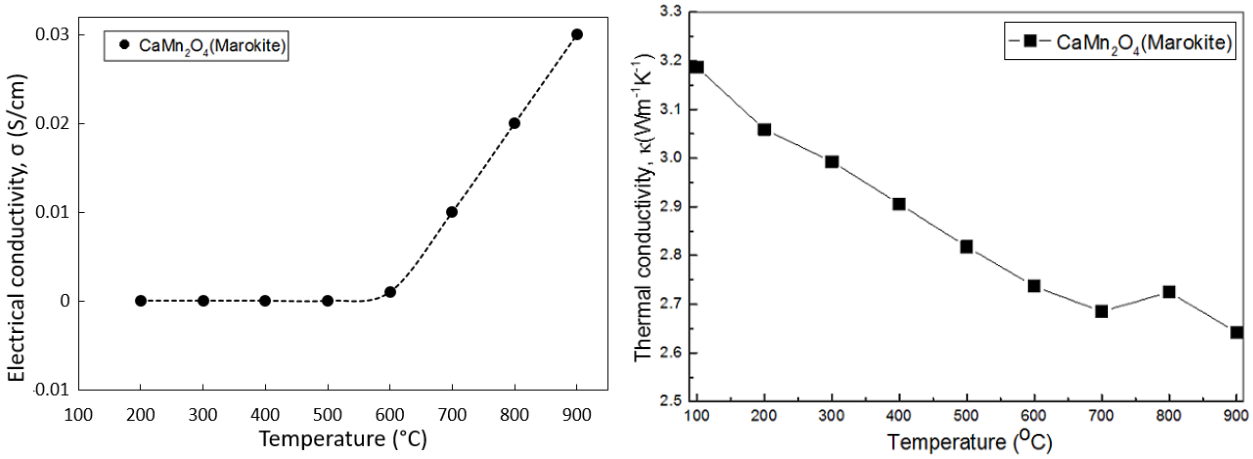

(a) Electrical conductivity

(b) Thermal conductivity

Figure 2.13: Conduction properties of marokite, $CaMn_2O_4$.[37]

$Ca_{0.5}Mn_{0.5}O$

The material formed in reducing atmosphere is $Ca_{0.5}Mn_{0.5}O$, also denoted $CaMnO_2$[41]. $Ca_{0.5}Mn_{0.5}O$ has a rock-salt crystal structure with Ca and Mn occupying every second corner and center-face sites, and oxygen atoms occupying all edges, as illustrated in Fig.2.14. The formation of the rock-salt structure is due to the solid solubility between CaO and MnO, Fig.2.7(b). In the crystal structure, Ca and Mn both have oxidation state +2 and almost similar ionic radii[42], which enables Ca- and Mn-ions to occupy the same sites. This means that the solid solution can be formed along the whole range of composition, and there are only one homogeneous phase present and no secondary phase as there is in oxidizing atmosphere. The theoretical density is 4.25 g/cm^3[43].

Phase transformation

If sintering of $CaMnO_3$ is conducted in oxidizing atmosphere, there will be no structural rearrangements during the sintering, and in case of Ca-deficient $CaMnO_{3-\delta}$, the two phases perovskite and marokite, will be present from the start to the end. On the other hand, if the mate-

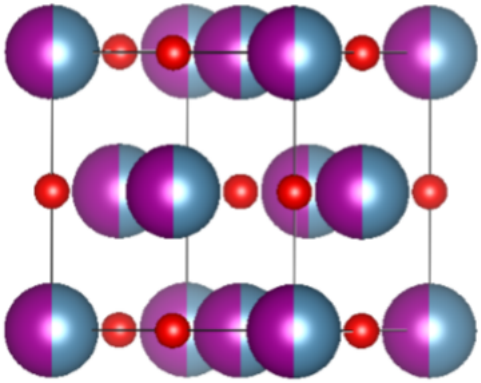

Figure 2.14: Crystal structure of $Ca_{0.5}Mn_{0.5}O$. Ca and Mn atoms are shown with 50% occupancy rate just for illustrative purposes. [10]

rial is heated in reducing atmosphere, structural transformations appear, and $CaMnO_2$ will be formed.

The $CaMnO_3$–$CaMnO_2$ reduction-oxidation process proceeds through oxygen diffusion while the cationic sublattice remains nearly unaltered[44]. The change in oxygen stoichiometry upon reduction is schematically presented in Fig.2.15 and shows that the framework of the perovskite structure is essentially maintained when δ<0.5 (b). In comparison, $CaMnO_{2.5}$ adopts a different structure (a brownmillerite structure[41]), in which all MnO_6 octahedra are transformed into MnO_5 square pyramides (c). Regardless of the elimination of some oxygen atoms the cation structural framework and remaining anionic sublattice are basically preserved[21, 20] Further reduction will finally result in a rearrangement of the atoms and $CaMnO_2$ is formed.[41] This shows that $CaMn^{4+}O_3$ is reduced to $CaMn^{2+}O_2$ through several metastable perovskite-related phases with Mn in different oxidation states.

This is also shown by the reversed reduction process, described by the following reactions:[45]

$$CaMn^{2+}O_2 \rightarrow Ca\mathrm{Mn}^{2+}_{1-2x}O_{2.5-x} \rightarrow CaMn^{3+}O_{2.5} \tag{2.17}$$

$$CaMn^{3+}O_{2.5} \rightarrow Ca\mathrm{Mn}^{4+}_{1-2x}O_{3-x} \rightarrow CaMn^{4+}O_3 \tag{2.18}$$

When the reduced material is re-oxidized, the perovskite structure is recovered, as the phase transformation of $CaMnO_3$ to $CaMnO_2$ is fully reversible. Eq.2.18 has several intermediate states with well-ordered oxygen vacancies and therefore well defined stoichiometries, which shows

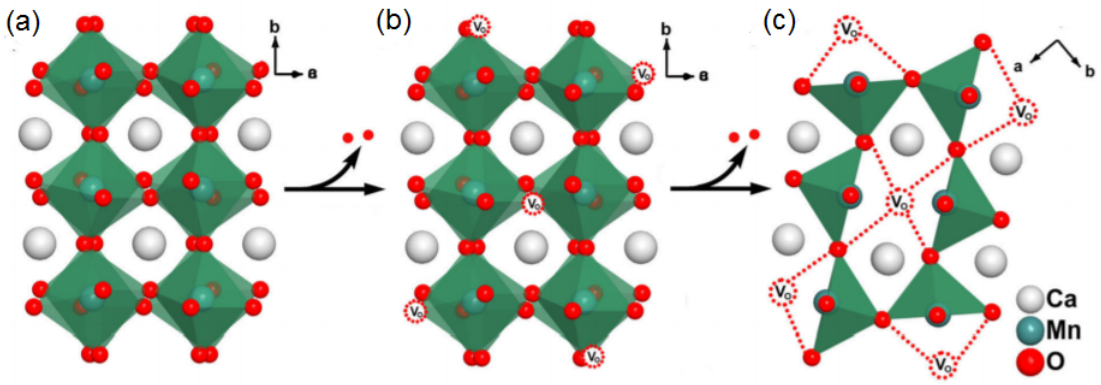

Figure 2.15: Schematic representation of the crystal structure frameworks of pristine and oxygen-deficient perovskite oxides showing a transition from stoichiometric $CaMnO_3$ (perovskite) (a) to nonstoichiometric $CaMnO_{2.76}$ (perovskite) (b) and $CaMnO_{2.5}$ (brownmillerite) (c). V_O represents oxygen vacancy. [21]

that intermediate phases with lower oxygen stoichiometry is formed before the desired perovskite is recovered. The phase transformation follows a topotactic reaction mechanism and is thus a very fast reaction[21, 44].

The first step in the oxidation process is oriented nucleation. $Ca_{0.5}Mn_{0.5}O$ is being used as a "substrate" for formation of nuclei, resulting in formation of small crystals with the perovskite structure on the surface of the rock-salt structure. In this way, stand alone nuclei do not have to be formed, which makes the process much easier as the nuclei can cross the critical size much easier and grow at a much faster rate.[10]

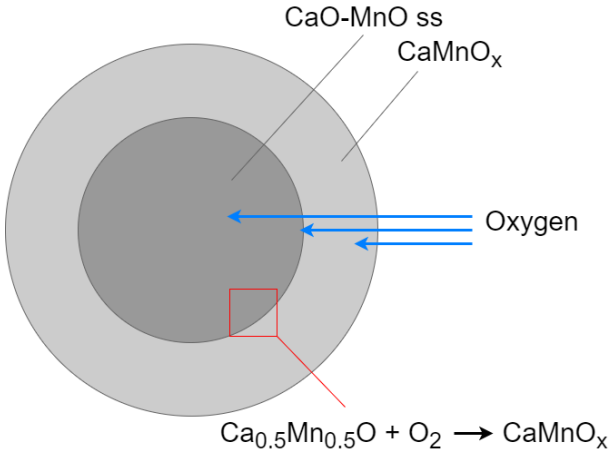

Figure 2.16: Illustration of the oxidation process from rock-salt to perovskite. The unreacted core consists of $Ca_{0.5}Mn_{0.5}O$, while the surface is of oxidized material, $CaMnO_{3-\delta}$. Inspired by figure in reference [10].

The second step is growth of the nuclei. In the transformation from $Ca_{0.5}Mn_{0.5}O$ to $CaMnO_3$, oxygen is needed. The oxygen atoms are coming from the atmosphere, and in the beginning of the reaction they are in close contact with the reduced phase through the sample surface. However, as the perovskite starts to form, oxygen will have to diffuse further into the sample through already formed perovskite layers. Hence, the initially very fast growth will slow down with time as the diffusion length will increase. This slows down the oxidation speed and results in formation of so-called shrinking core.[10] The process is illustrated in Fig.2.16.

When calcium deficient $CaMnO_3$ with composition $Ca_{0.931}MnO_{3-\delta}$ is formed from the rock-salt structure, the secondary phase marokite is exsoluted. Thus, a slightly different reaction occurs, described by the following oxidation reaction:

$$Ca_{0.931}MnO_{2-\delta} + \frac{\delta}{2}O_2 = 0.863CaMnO_3 + 0.0686CaMn_2O_4 = Ca_{0.931}MnO_{3-\delta} \tag{2.19}$$

where δ=0.14 and 10 vol% marokite is formed. The oxidation state of Ca and O is always +2 and -2, respectively, whereas Mn changes oxidation state from +2 in rock-salt to +3 and +4 in Ca-deficient $CaMnO_{3-\delta}$.

Introducing 2% Ta on Mn-site results in following reaction, assuming Ta is dissolved in the pervoskite phase and with δ=0.12:

$$\begin{aligned} Ca_{0.931}Mn_{0.98}Ta_{0.02}O_{2-\delta} + \frac{\delta}{2}O_2 &= 0.862CaMnTa_{0.023}O_3 + 0.049CaMn_2O_4 \\ &= Ca_{0.931}Mn_{0.98}Ta_{0.02}O_{3-\delta} \end{aligned} \tag{2.20}$$

2.4 Densification of ceramics

2.4.1 Sintering parameters

Densification and grain growth are two occurring phenomena during sintering. Densification is normally favored, while grain growth should generally be opposed or at least controlled.

Particle diameter and sintering temperature have a major effect on the rate of sintering, hence are the most important parameters enhancing the density. High temperature increases the sintering rate. So do smaller particles, which means that powder with finer particle size can be sintered more rapidly and at a lower temperature than coarser powder. The sintering time also affects the density in the way that longer times increase the shrinkage. In addition, high temperature and long holding time promote grain growth, which is driven by surface energy. To minimize the surface free energy, surface area must be reduced, which hence is the driving force for grain boundary elimination and grain growth.[23]

To obtain high density, some grain growth is necessary. However, when sintering nanostructured powders, it is crucial to restrict extensive grain growth in order to preserve the nanostructure in the final material, and consequently, in case of thermoelectric materials, obtain low thermal conductivity. Hence, it is essential to keep sintering times and temperatures as low as possible.

2.4.2 Spark plasma sintering (SPS)

One approach to achieve dense materials with fine grain structure, is to sinter under pressure and electric discharge. The sintering method called spark plasma sintering (SPS), promotes densification of ceramics and powdered metals at moderate temperature and short time. The sintering temperature in SPS is normally 200 to 500°C lower than the temperature used in conventional sintering processes, and the time is reduced from hours to minutes[46]. This allows a much better control of the resulting microstructure compared with traditional pressure-less densification. Due to the strong densification and the grain size control, better thermoelectric properties are achievable, as demonstrated by Noudem *et al.*[47], who investigated calcium manganite doped with samarium.

The process is similar to conventional hot pressing, where the precursors are placed in a die and a uniaxial pressure is applied during sintering. However, instead of using external heating source, the sample is heated from the inside by applying a large pulsed current that passes through the sample. The current also passes through the electrically conducting pressure die, which implies that the die also acts as a heating source and heats the sample from the outside.[48, 46] A schematic drawing illustrating the setup for spark plasma sintering is shown in Fig.2.17.

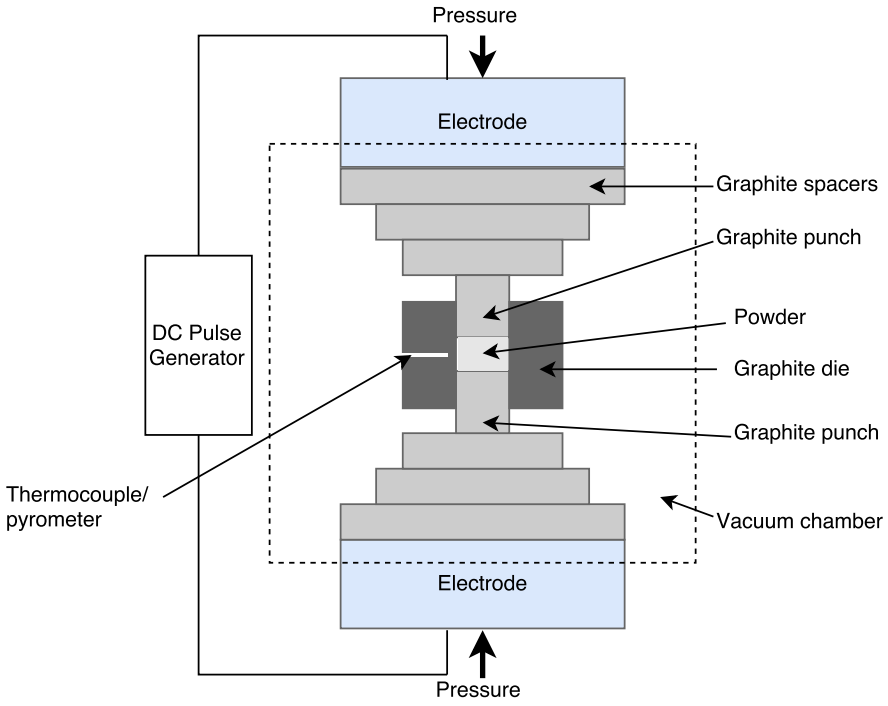

Figure 2.17: Schematic drawing illustrating features of an SPS apparatus.

Thus, the unique features of the process are the possibilities of using very fast heating rates and very short holding times to obtain fully dense samples. According to M. Tokita[49], this is possible due to a spark plasma generated between grains. By repeatedly applying a low-voltage pulsed current, electrical discharge will be produced between neighboring particles. The discharge will first generate a spark plasma, then an impact pressure due to the sparks and heating by the Joule effect.

3 | Experimental

3.1 Chemicals and Apparatus

The precursor powder investigated in this study is $Ca_{0.931}Mn_{0.98}Ta_{0.02}O_{3-\delta}$, referred to as CMTO. The powder was produced by spray pyrolysis and delivered by CerPoTech AS. The chemicals and gases used during procedure and the characterizations are presented in Tab. 3.1.

Table 3.1: List of chemicals and gases

Chemical	Formula	Supplier	Purity
CMTO	$Ca_{0.931}Mn_{0.98}Ta_{0.02}O_{3-\delta}$	CerPoTech	High purity
Isopropanol	C_3H_8O	VWR International AS	>99.8%
Ethanol	CH_3CH_2OH	VWR International AS	96%
5% Hydrogen in Argon	5% H_2 in Ar	Yara Praxair	5.0
Nitrogen	N_2	AGA AS	5.0
Synthetic air	Air	AGA AS	5.0

5 % hydrogen in argon was used to reduce the precursor powder prior to the sintering and to thermally etch the samples after sintering. The pellets were annealed in nitrogen (inert atmosphere) and synthetic air (oxidizing atmosphere). The apparatus and instruments used in this work are listed in Tab. 3.2.

Table 3.2: List of apparatus used in the characterization, the sintering procedure and thermoelectric measurements, in addition to their model and application area

Apparatus	Model	Application
SPS	Dr. Sinter SPS 825	Sintering
XRD	Bruker D8 Advance DaVinci	Phase composition
HTXRD	Bruker D8 Advance	Annealing program
SEM	Zeiss Supra 55 VP	Microstructure and phase distribution
Dilatometer	Netzsch DIL 402C	Annealing analysis
TGA	Netzsch STA 449C	Oxidation analysis
Vacuum desiccator	-	Density and porosity
Alumina tube furnace	Super kanthal	Heat treatments
Grinder	Struers LaboPol-21	Polishing of samples
Grinder	Struers RotoPol-31	Diamond polishing of samples
Electrical conductivity	Home built 4-point probe design	Electrical conductivity measurements
Seebeck measurement	NorECs Probostat	Measurement of Seebeck coefficient
Thermal conductivity	Netsch LFA 457 MicroFlash	Thermal conductivity measurements

3.2 Procedure

The procedure can be divided into four main steps:

1. **Powder processing** Heat treatment of as-received CMTO-powder in reducing atmosphere to produce single phase $Ca_{0.5}Mn_{0.5}O$ (rock-salt structure).

2. **Sintering** Establish a program for spark plasma sintering (SPS) to obtain a dense material of $Ca_{0.5}Mn_{0.5}O$ with well-defined microstructure. Structural characterization was carried out by XRD, SEM and Archimedes' method.

3. **Annealing** Oxidation in air to form $CaMnO_3$ and desired secondary phase. Structural characterization was carried out by XRD, SEM/EDS and Archimedes' method.

4. **Characterization of thermoelectric properties** Assess the thermoelectric properties (electrical conductivity, thermal conductivity and Seebeck coefficient) for some chosen samples with a well-defined microstructure.

Fig.3.1 gives an overview of the project work. It does not include all procedure details, such as thermal etching or the necessity to make new samples in SPS for the characterization of thermoelectric properties.

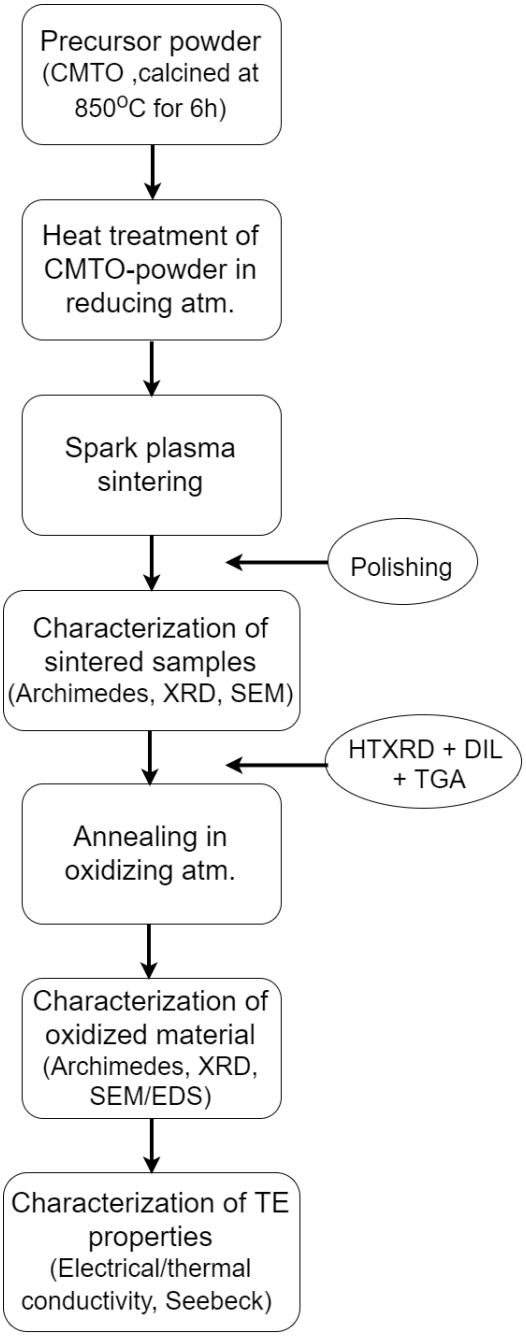

Figure 3.1: Flowchart illustrating the main parts of the work.

It should be noted that the details provided in following sections are the optimized conditions to obtain desired material. Optimization of the parameters was a big part of the work and the results of different approaches are described in Section 4 or in appendices.

3.2.1 Powder processing

As-received powder

The CMTO-powder from CerPoTech AS was produced by spray pyrolysis, in order to obtain particles in the nanometer range. It was calcined in air at 850 °C for 6 hours, dry and wet ball-milled, sieved and burnt prior to delivery.[50]

The composition, $Ca_{0.931}Mn_{0.98}Ta_{0.02}O_{3-\delta}$, shows calcium deficiency, which is introduced to form 10 vol% secondary phase of marokite. The diffractogram in Fig.3.2 shows the presence of the main phase, $CaMnO_{3-\delta}$, and the secondary phase, $CaMn_2O_4$. In addition, it shows a small amount of $Ca_2Mn_3O_8$, the 2:3-phase presented as the secondary phase at lower temperatures in the phase diagram, Fig.2.7. The crystallite size of the main perovskite phase is approximately 40 nm, and 30 nm in the secondary marokite phase. Particle size based on SEM images, is approximately 200 nm, shown in Fig.3.3. Characterization of the CMTO-powder was conducted during the specialization project fall 2016[25].

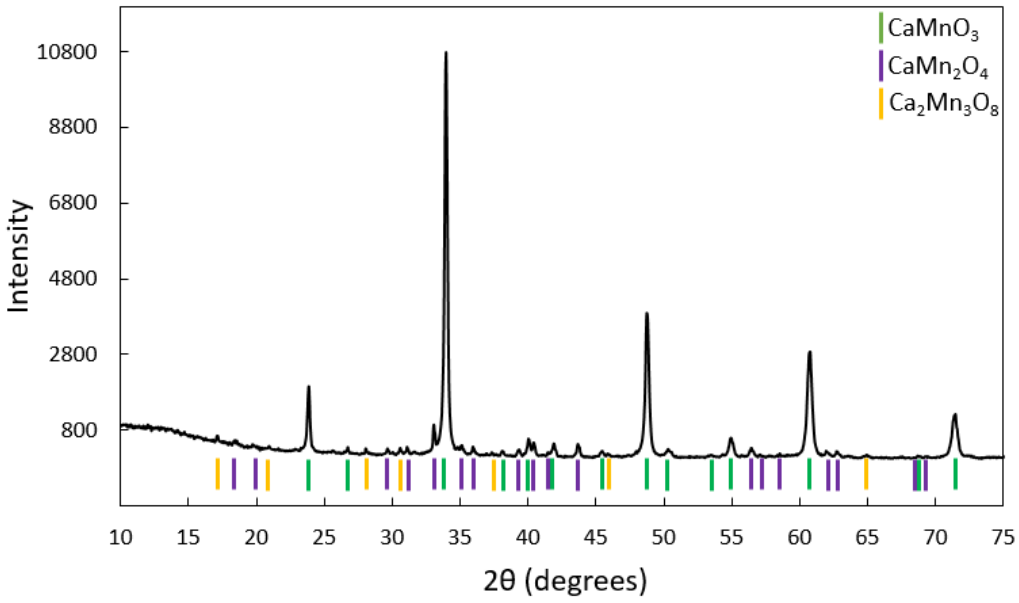

Figure 3.2: XRD pattern of as-received CMTO-powder[25]. The perovskite phase (PDF 01-070-7306) is marked in green, the secondary marokite phase (PDF 04-014-8192) is marked in purple and the 2:3-phase (PDF 04-009-4202) is marked in yellow.

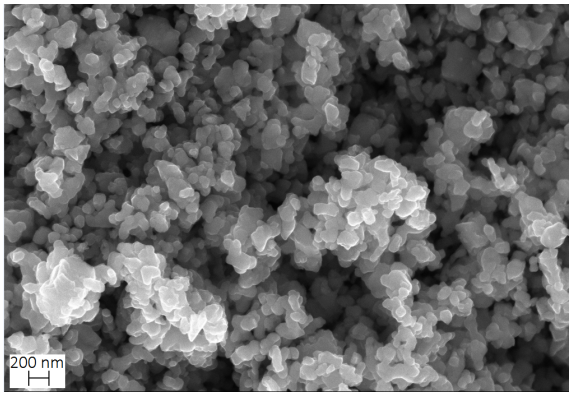

Figure 3.3: CMTO precursor powder with particle size approximately 200 nm. [51]

Heat treatment

The calcination of the precursor powder promoted precipitation of a secondary phase of spinel structure. The first part of the project was therefore to investigate heat treatment procedure in reducing atmosphere to produce single-phase $Ca_{0.5}Mn_{0.5}O$ with rock-salt structure. It is desired to sinter the material in its reduced phase, as a previous study performed by Ledezma[25] showed that this will reduce the grain size in the re-oxidized material.

The heat treatment of the powder was conducted in an alumina tube furnace with 5% H_2 in Ar as reducing gas. Five different heating programs, presented in Tab.3.3, were investigated. In the programs with dwell time of six hours, three temperatures were applied: 600°C, 700°C and 800°C. Dwell time of three hours was also investigated, in order to study the dwell time's impact on crystallite size. In these programs, 600°C and 800°C were chosen as maximum temperatures. T=800°C and dwell=3h was chosen as the optimal heating program, and is presented in Fig.3.4. This heat treated and reduced CMTO-powder, with single phase rock-salt structure was used as a precursor for the remaining part of the study.

Table 3.3: Parameters in the investigated heating programs. Heating and cooling rate of 200°C/h in all programs.

Program #	Temperature [°C]	Dwell [h]
1	600	6
2	700	6
3	800	6
4	600	3
5	800	3

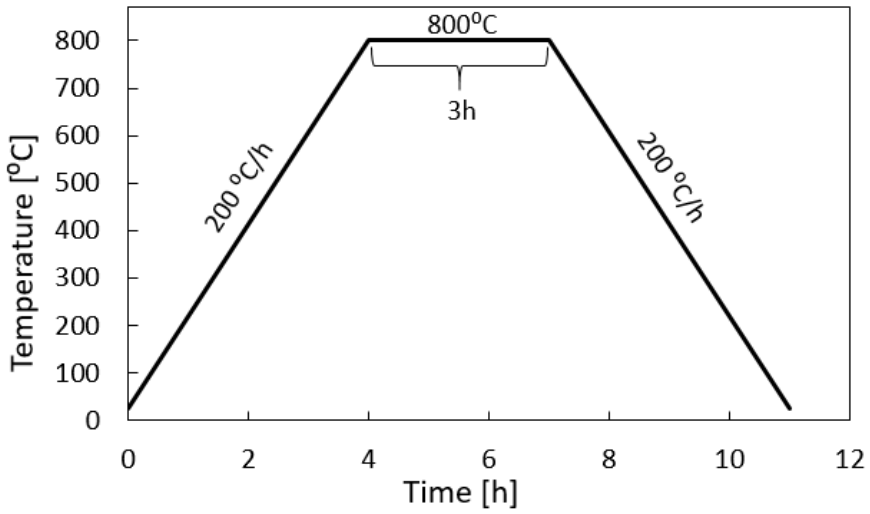

Figure 3.4: Chosen heat treatment programs: max temperature = 800°C and dwell = 3h. Reducing atmosphere (5% H_2 in Ar) during the whole program. Heating- and cooling rate of 200°C.

The maximum temperature used in the heat treatment was chosen based on the sintering properties of CMTO, investigated in the specialization project fall 2016[25]. Sintering curve conducted from dilatometry measurements is shown in Appendix B.

Characterization

X-ray diffraction (XRD) analysis was used to study phase compositions in the samples. With the X-ray Diffractometer Bruker D8 Advance DaVinci the presence of two phases in the received precursor powder was confirmed, and obtained phases after the heat treatment were established. This instrument has CuK_α radiation, however, additional peaks caused from CuK_β may be present in the pattern. Scans were performed between 10 and 75 2θ. EVA software[52] were used to analyze the obtained XRD patterns. Because the diffraction pattern is considered as the fingerprint of a crystalline material, the phase composition and compounds can be identified by comparison with a database of known materials. The database used is the International Centre for Diffraction Data (ICDD).

Crystallite size was conducted from the diffractiograms and by the use of the XRD software TOPAS[53]. TOPAS uses Rietveld refinement to calculate mean crystallite sizes. It applies Lorentzian convolution and calculates FWHM (Full Width at Half Maximum from Scherrer

equation) and Integral breadth for all peaks in the profile.

3.2.2 Spark Plasma Sintering

CMTO-powder reduced to a single phase rock-salt structure, $Ca_{0.5}Mn_{0.5}O$, was sintered by the use of spark plasma sintering (SPS). Different programs, including pressure, temperature and sintering time, were investigated, in order to produce a dense sample with well defined microstructure. The as-produced pellets were characterized with respect to density, porosity, phase composition, crystallite size and microstructure.

Sample preparation

When using SPS, sample preparation is important, and some steps need to be performed before the sample is placed in the chamber of the SPS. Wanted amount of powder to be sintered is weighed out and placed in a cylindrical graphite die of chosen diameter. When filling the die it is important to evenly distribute the powder and try to obtain a flat surface. Before the filling, the walls inside the die need to be covered with graphite foil. Graphite foil should also be placed between the powder and the punches at each end, such that the powder is completely surrounded by graphite. When placing the punches it is important to not damage the graphite foil. In addition, the outside of the die should be covered with carbon wool.

When the preparation is completed, the die can be placed into the working chamber in the SPS between graphite spacers, as illustrated in Fig.2.17. It is crucial that the die is placed in the center, to evenly distribute the applied load.

SPS program

When the sample is placed correctly, the vacuum is set. While the pressure and dwell time were the same throughout the experiments, the temperature was varied. The parameters are programmed before the SPS is started, and the program runs automatically. As presented in Tab.3.4, six samples were investigated. Load, load point displacement (material's thickness variation) and temperature were recorded as a function of time during sintering, by the SPS controller program.

Table 3.4: Program parameters for spark plasma sintering.

Sample #	Pressure [MPa]	Dwell [min]	Temperature [°C]
1	50	5	850
2	50	5	950
3	50	5	1000
4	50	5	1050
5	50	5	1150
6	50	5	1250

In order to find the optimal program, the cooling rate and the application and release of load were varied. The curves for the applied program is presented in Fig.3.5. This shows that the pressure was increased to maximum pressure in a couple of minutes, while the temperature was increased from 400°C to maximum temperature in five minutes. The pressure start to increase from approximately 18 MPa (2.2 kN) to maximum pressure. Pressure (MPa) is converted to load (kN), which varies with the diameter of the die.

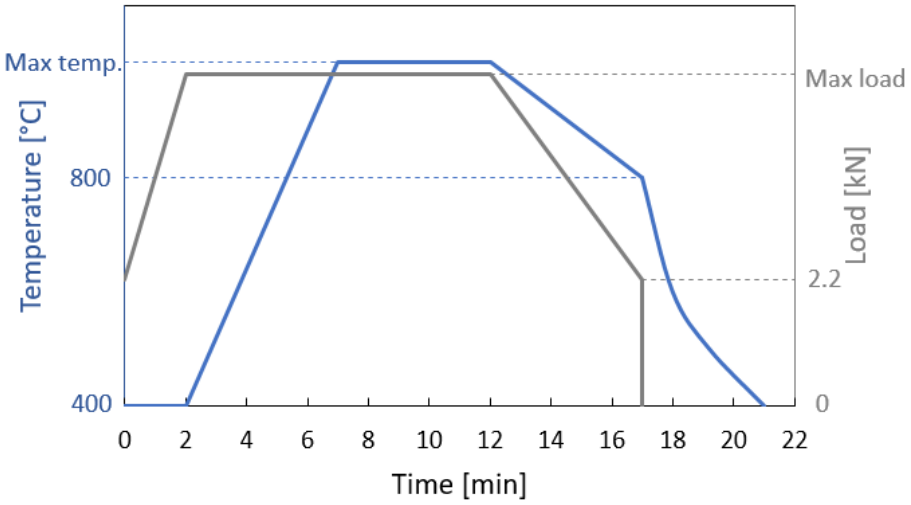

Figure 3.5: Optimal program used for spark plasma sintering (SPS) of all six samples, showing temperature and load as a function of time.

The temperature was decreased to 800°C in five minutes after the holding time at max temperature, and then dropped as the sintering program is turned off. The load was also reduced in five minutes, from maximum value to the starting load of 2.2 kN. When pressure and temperature are dropped, it is important to release the graphite spacer from the electrode when working with ceramics, to avoid cracking as a result of too rapid cooling. Hence, there are noe load data from this point, which is the reason the load curve drops directly to zero from 2.2 kN.

The sample temperature was monitored with a pyrometer, which detects temperatures above 400°C. For this reason, temperature data below 400°C are not available.

The as-prepared thick samples were polished with SiC polishing cloths to remove the graphite foil used to prevent the compact to stick onto bearings.

3.2.3 Characterization of sintered samples

Preparations

In order to achieve good characterization results of the sintered pellet, some preparations were necessary. Prior to XRD-analyses, pellets were polished by the use of SiC polishing cloths of grit sizes 800 to 4000. They were then cleaned in an ultrasonic bath. After XRD, further polishing was performed, and diamond-polishing with a polishing cloth of 1 μm grit was chosen. In addition to the polishing, thermal etching of the samples was necessary to be able to see grain boundaries in SEM. The temperature was set to be 50°C below the sintering temperature and heating and cooling rate to 200°C/h. Different dwell times were investigated, and the best results were obtained with 30 minutes dwell time.

Schematics of heating programs for thermal etching of each sintered sample are presented in Appendix.E.

Phase composition and crystallite size

X-ray diffraction (XRD) was used to determine the phase composition of the sintered samples. Bruker D8 Advance DaVinci X-ray Diffractometer, which has CuK_α radiation, was used, and scans were performed between 10 and 75 2θ. EVA software was used to analyse the obtained XRD patterns, and International Centre for Diffraction Data (ICDD) was the database used to compare the diffraction patterns. TOPAS[53] was used to find mean crystallite size and the relative amount of phases. The software provides phase amount-results in weight%, which are then converted into volume% by using the theoretical densities.

Microstructure

The microstructure, with respect to density, porosity, grain size, grain boundaries and phase distribution, were investigated by the use of different methods and measurements.

Scanning Electron Microscopy (SEM) imaging was performed to obtain information about pores, grains and secondary phases. All SEM images presented in this thesis were taken with Zeiss Supra 55 VP.

Pellets were broken to get a cross-sectional view of the fracture, making it possible to study density and pores. To see the grain size and grain boundaries, the polished and thermally etched surface of the samples were studied. Average grain intercept (AGI) method was utilized to calculate the grain size with more than three images per specimen and more than ten lines per image.

Archimedes' method, performed in accordance to the ISO 5017 procedure, was used to determine the density and the porosity of the compacted samples. This density measurement is based on sample weight when the sample is dry, immersed and wet. To replace the air in the pores with liquid, a vacuum desiccator was used. Isoropanol was chosen to be the immersion liquid. The theoretical density of the material used in the calculations is calculated from crystallographic data. The value is 4.35 g/cm^3 for the reduced material and 4.70 g/cm^3 for the oxidized structure. Equations to perform the calculations are presented in Appendix C, and calculations of theoretical densities are found in Appendix D.

3.2.4 Annealing

As the sintering will take place at reducing conditions, the as received samples from SPS will still be a single phase rock-salt structure. In order to obtain the perovskite- and spinel phases, which were present in the original CMTO-powder, the samples were annealed in oxidizing atmosphere (synthetic air).

HTXRD

The transformation between rock-salt and the perovskite/spinel-phases was investigated by high temperature XRD (HTXRD) in air. By scanning at different temperatures between room

temperature and a given maximum temperature, it is possible to register at approximately what temperature the rock-salt structure transforms to perovskite structure. It also provide information about the temperature and time necessary to form the secondary phase. In this case, the maximum temperature was 900°C and scans of ten minutes were conducted at every 100°C, from 2θ=20° to 2θ=75°. $Ca_{0.5}Mn_{0.5}O$ precursor powder was used in the analysis.

DIL

Dilatometry (DIL) is a method used to measure sample's dimension change at given temperatures. Netzsch DIL 402C with preprogrammed alumina standard was used in all analyses. The measurements were performed in synthetic air, with flow rate of 30mL/min, heating and cooling rate of 2 K/min, 1300°C as maximum temperature and one hour dwell time. DIL was used to investigate the oxidation properties of the material and to find the thermal expansion coefficient (TEC), which can be calculated from the obtained curve (dimension change as a function of temperature), using following equation:

$$TEC = \frac{\Delta dl/l_0}{\Delta T} \tag{3.1}$$

In addition, DIL was used to find TEC of the reduced sample, following the same method and parameters, but with N_2 instead of synthetic air.

Sintered samples were used in the measurements.

TGA

Thermogravimetric analysis (TGA) was used to determine oxidation properties of $Ca_{0.5}Mn_{0.5}O$ and gain insight into the phase transformation. Netzsch STA 449C with preprogrammed alumina standard was used in the analysis. Maximum temperature and dwell time, as well as heating and cooling rate were the same as in the DIL measurements, i.e. maximum temperature of 1300°C, dwell time of one hour and 2 K/min rate. Synthetic air at flow rate of 30mL/min was the selected atmosphere. A pellet of sintered $Ca_{0.5}Mn_{0.5}O$ was pulverized and used in the analysis.

Annealing program

Based on the results from HTXRD, DIL and TGA, a program for annealing the pellets in oxidizing atmosphere was worked out. The most suitable heating program, presented in Fig.3.6, involved heating up the dense sintered pellet in inert atmosphere (N_2) up to 1100°C at the rate of 200°C/h. The inert gas was kept for 30 minutes of the total dwell time of 6.5 hours before the atmosphere was shifted to oxidizing by introducing synthetic air. The annealing process starts when synthetic air is introduced. The cooling rate was 50°C/h.

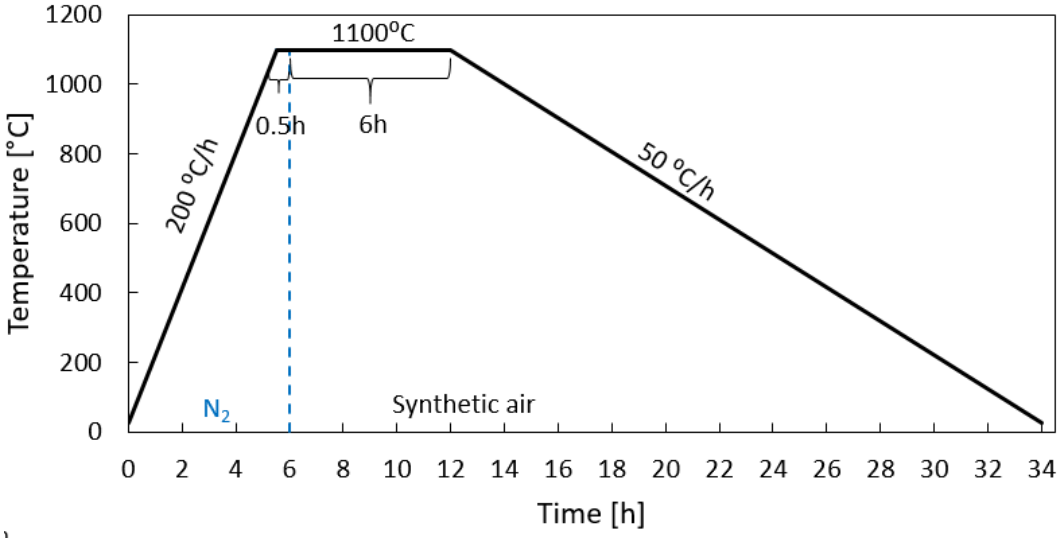

Figure 3.6: Heating program for annealing the sintered samples. Heating in inert atmosphere with rate of 200°C/h. Maximum temperature of 1100°C and dwell time of 0.5h in N_2 and 6h in synthetic air. Cooling rate of 50°C.

3.2.5 Characterization of annealed samples

Phase composition and microstructure were characterized with same techniques as used for the sintered samples: XRD to find phase composition and crystallite size, SEM to investigate microstructure and Archimedes to measure density (Section 3.2.3). Of particular interest was the resulting microstructure with focus on the distribution of the secondary spinel-phase. Therefore, **Energy Dispersive X-ray Spectroscopy (EDS)** was used in addition to SEM, as EDS provides detailed information of chemical composition and distribution. Hence, EDS was used to detect the different phases in the oxidized samples, and to study where in the microstructure they are

located. Both line scans and point analyses were conducted. SEM-images using signals from backscatter electrons (BSE) were collected in addition to secondary electron (SE) images, for the same purpose as EDS. In BSE images it is possible to distinguish between phases due to difference in contrasts, where heavier phases appear lighter as more electrons are scattered.

3.3 Thermoelectric properties measurements

3.3.1 Electrical conductivity

Electrical conductivity was measured in air through a four-point probe method, with a home-built set-up. In this method, the current is supplied by two voltage probes, while two other probes are measuring the potential drop over the sample. The conductivity is then calculated by[10]:

$$\sigma = \frac{I}{V}\frac{l}{A} \tag{3.2}$$

where I is the supplied current, V is the voltage drop, A is the cross section of the sample, and l is the distance between the voltage probes, which was set to 0.5 cm.

During the measurements, the temperature was increased from room temperature to 900°C with a heating rate of 80°C/h. The cooling was performed in steps with 3.5h dwell time every 100°C, allowing the temperature and σ-values to stabilize. At the end of the program, the temperature is increased to 900°C once more to confirm the registered value from the first measurement. The heating program is illustrated in Fig.3.7.

Special samples were prepared for the measurement. Dense bars with approximate dimensions 2mm (thickness)x 4mm (width) x 12mm (length) were cut out from the spark plasma sintered and annealed pellets.

3.3.2 Seebeck coefficient

The Seebeck coefficient measurements were performed with a Probostat device. Measurements were conducted every 100°C between 900°C and room temperature, in synthetic air. The heating program is identical to the program used for electrical conductivity measurements, and is

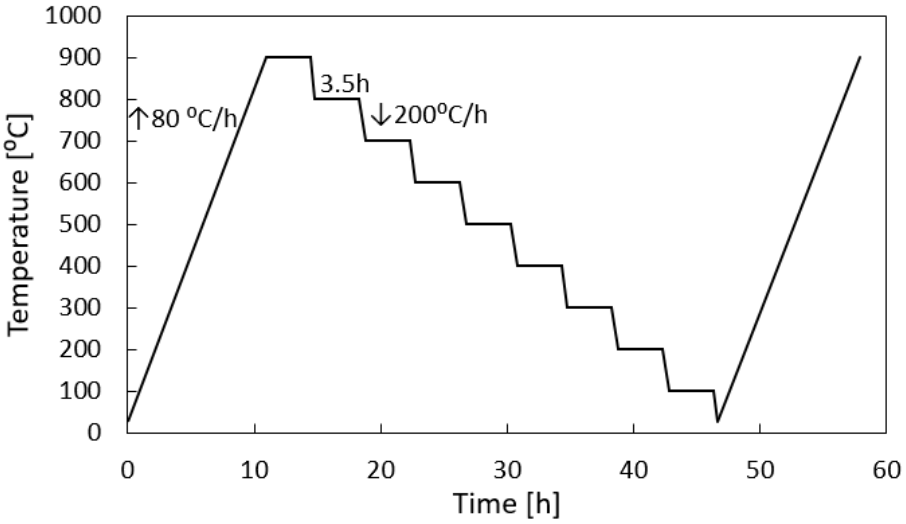

Figure 3.7: Schematic of heating program used for both the electrical conductivity and the Seebeck measurement.↑ indicates heating rate and ↓ indicates cooling rate. The dwell time at each temperature step is 3.5h.

illustrated in Fig.3.7. The 3.5h dwell time on each temperature increment allows the temperature and S-values to stabilize. Same bars as for electrical conductivity measurements were used for Seebeck measurements.

The Seebeck coefficient is determined by applying small temperature gradients over the sample and measuring temperature gradient and voltage at its cold and hot ends. Those values give $S_{measured}$ by the use of Eq.2.2. To obtain Seebeck coefficient for the material, S_{sample}, contribution from the thermocouple (Pt wire), S_{tc}, used as reference in the measurement must be subtracted[10], hence

$$S_{sample} = S_{measured} - S_{tc} \tag{3.3}$$

3.3.3 Thermal conductivity

The thermal conductivity was determined by the use of Netzsch LFA 457 MicroFlash instrument and the laser flash method. The measurements were conducted in air in the temperature range 100°C–900°C with three measurements at every 100°C increment.

By the laser flash method, the thermal diffusivity, α, and the heat capacity, C_p, can be measured. In this method, the front of the sample is irradiated by a short heating pulse caused by a

laser. The irradiation causes the temperature on the opposite surface to increase and the temperature change is measured, in addition to the time it takes for the pulse to reach the rear side. The thickness of the sample is hence important. The thermal diffusivity is then determined by the shape of the temperature versus time curve at the rear surface. The diffusivity is expressed as[54]:

$$\alpha = \frac{1.38d^2}{\pi^2 t_{1/2}} \tag{3.4}$$

where d is the sample thickness and $t_{1/2}$ is the "half time", which is the time required for the back surface to reach half of the maximum temperature rise.

The heat capacity of the material is determined by the maximum temperature indicated by the thermocouple, and can be used to calculate the thermal conductivity with following equation[54]:

$$\kappa = \alpha \rho C_p \tag{3.5}$$

where ρ is the density of the sample.

Netzsch Proteus LFA analysis software was used to obtain the thermal conductivity values, and Pyroceram 9606 supplied by Netzsch was used as a standard for the measurements.

To perform the measurements, special samples with 0.5" diameter and 1-2mm in thickness were prepared by polishing the samples from SPS.

4 | Results

4.1 Heat treatment of precursor powder

The first part of the procedure was to reduce the CMTO-powder to obtain a single-phase material instead of a two-phase material. Fig.4.1(a) shows the phase composition resulted from the heating program #1-3 presented in Tab.3.3. At 800°C, single phase rock-salt structure, $Ca_{0.5}Mn_{0.5}O$ (PDF 04-009-4202), is achieved.

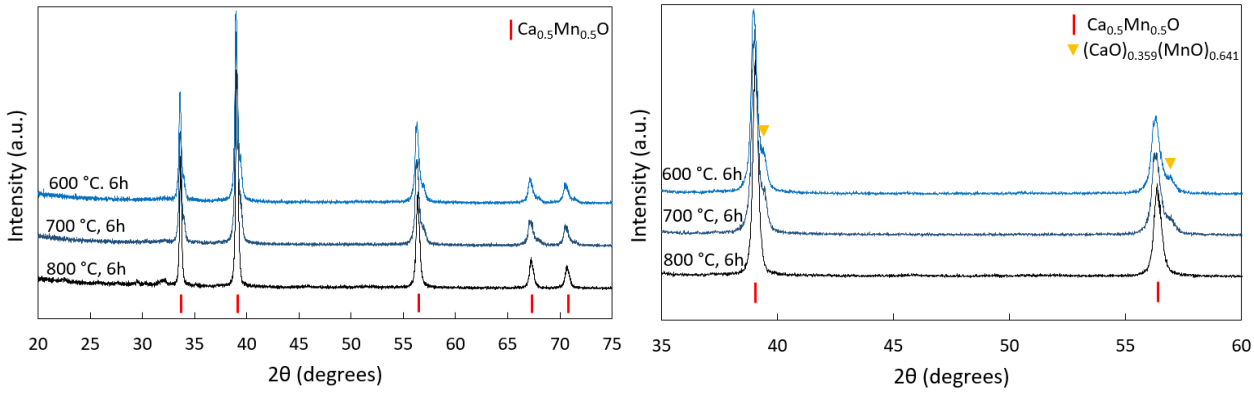

(a) Complete diffractogram.

(b) Focus on secondary rock-salt phase.

Figure 4.1: The XRD-results of the powders heat treated at 600°C, 700°C and 800°C for 6 hours. Undefined peak at 2θ=32 is due to tungsten radiation.

At 700°C and 600°C, the rock-salt structure is present, however, there are additional peaks at a higher 2θ. These indicate a rock-salt structure with different stoichiometry, caused by the spinel phase in the precursor powder. 600°C and 700°C are not high enough temperatures to fuse the two rock-salt structures together, hence two rock-salt phases are present. This is marked in Fig.4.1(b).

By applying the heating program with three hours dwell time (#4-5 in Tab.3.3), identical

result was obtained at 800°C. The diffractogram is presented in Fig.4.2(a). It is seen that the additional peaks at 600°C are more evident with this program. Two of them are presented in Fig.4.2(b), to clearly show that these peaks represent an additional phase and are not caused by $K_{\alpha 2}$ emission.

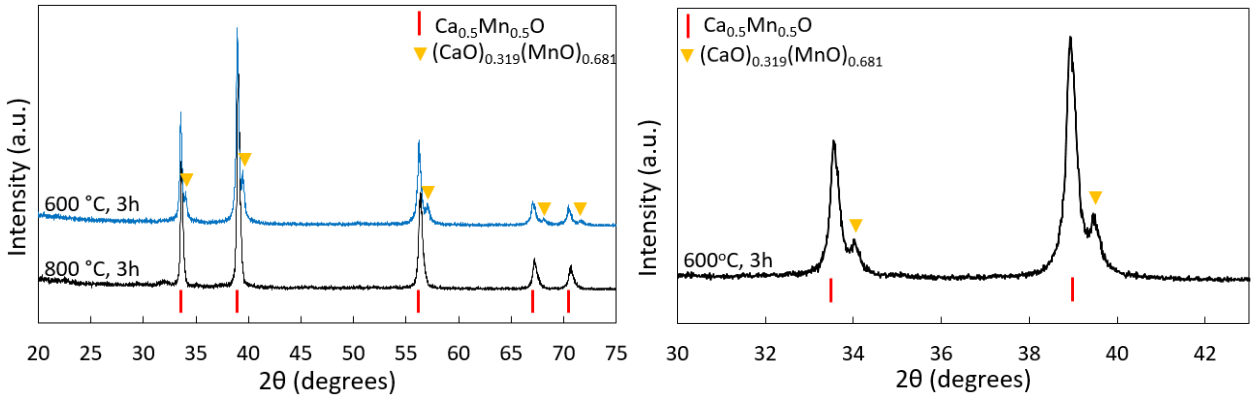

(a) Complete diffractogram of powders heat treated at 600°C and 800°C.

(b) Powder heat treated at 600°C. Focus on the secondary rock-salt phase.

Figure 4.2: The XRD-results of the powders heat treated for 3 hours. Undefined peak at 2θ=32 at 800°C is due to tungsten radiation.

Mean crystallite sizes were calculated using Rietveld analyses and Scherrer equation in TOPAS software. The average crystallite sizes of CMTO precursor powder before the heat treatment were ≈40 nm for the $CaMnO_3$-phase with perovskite structure and ≈30 nm for the secondary spinel-phase, $CaMn_2O_4$[25]. Mean crystallite sizes for the reduced powders are presented in Tab.4.1, which shows that the crystallites get smaller when the holding time is shorter, especially at 800 °C. Lower temperature also result in smaller crystallites, but the difference is rather small between 800 °C and 600 °C.

Table 4.1: Average crystallite size of the $Ca_{0.5}Mn_{0.5}O$ phase at different temperatures and dwell times. Powder was not heat treated at T=700 °C and dwell=3h. Calculated using TOPAS.

Temperature [°C]	Crystallite size [nm]	
	Dwell = 6h	Dwell = 3h
800	35	27
700	28	-
600	27	25

The powder heat treated at 800°C has a more defined phase composition compared to the

powder heat treated at 600°C. Due to this, and the insignificant difference in crystallite size, this powder was chosen as the best result. Hence, single-phase $Ca_{0.5}Mn_{0.5}O$ with rock-salt structure and mean crystallite size of approximately 30 nm was used as precursor for the remaining part of the investigation.

A SEM image of this powder is shown in Fig.4.3, where the particle size is observed to be approximately 200 nm. Due to poor conduction, the image is of low quality.

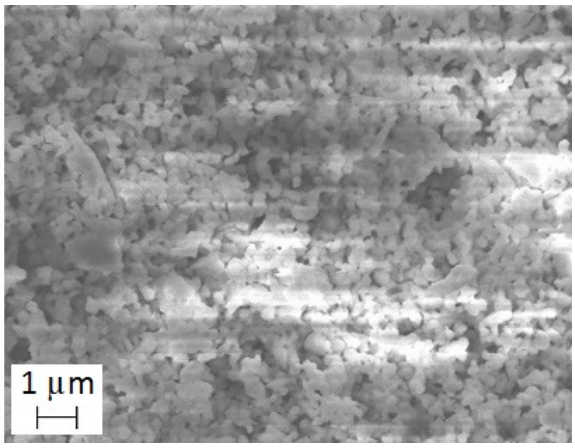

Figure 4.3: Powder heat treated at 800°C. Particle size approximately 200 nm.

4.2 Spark Plasma Sintering

4.2.1 SPS curves

Fig.4.4 shows load point displacement as a function of temperature of all sintered samples. Load point displacement gives the change in material's thickness, measured along z-axis, and is set to equal zero at the starting pressure, corresponding to applied load of 2.2 kN. When the sample shrinks during powder compaction and sintering, the value increases in absolute value as the change from initial thickness increases. The curves show fast densification as the temperature increases. Regardless of maximum temperature, the densification stops between 880°C and 930°C, where the curves flat out. Further, a moderate expansion is observed, which is due to thermal expansion in the graphite spacers placed between the sample and the electrodes. The 850°C-sample is an exception of this trend, indicating that this sample is not completely sintered.

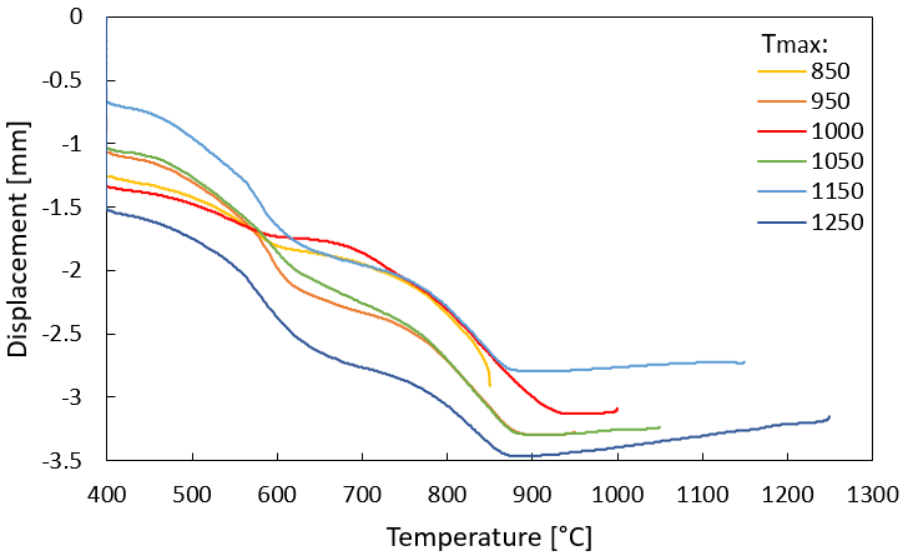

Figure 4.4: Load point displacement, representing variation in sample's thickness, as a function of temperature. One curve for each sample sintered at given T_{max}.

As there is thermal expansion in the graphite that affects the displacement values, there are not stationary conditions. Hence, these curves cannot be seen as sintering curves, however, they give an indication of the sintering behavior.

4.2.2 Phase composition

As the sintering takes place at reducing conditions, it is anticipated that the as received samples from SPS will still be a single-phase rock-salt structure. However, a secondary phase is additionally present at higher temperatures. The XRD-results, Fig.4.5, show that this is a calcium tantalum oxide-phase with composition $CaTa_2O_6$, marked in yellow. This is a cubic phase with pattern number PDF-00-036-0805 and space group Pm-3[52]. The intensity of this phase increases with increasing temperature, which is why it was not observed in the powder heat treated at 800°C. In addition, it is observed a shift to the right, which is a result of reduction in cell parameters.

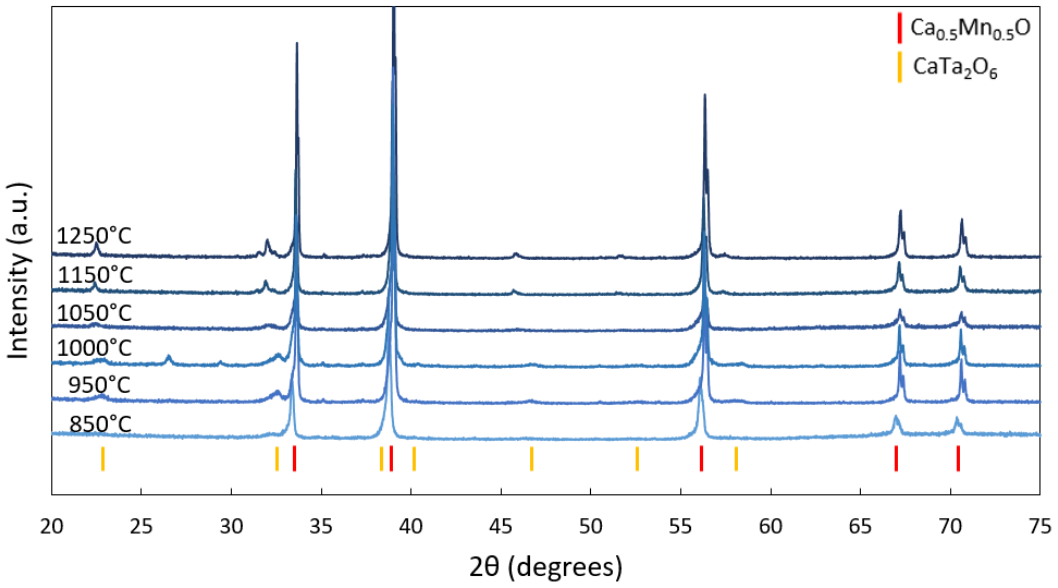

Figure 4.5: The XRD-results of the sintered samples. The main phase is the rock-salt structured $Ca_{0.5}Mn_{0.5}O$ (PDF 04-009-4202), and the secondary phase is $CaTa_2O_6$ (PDF 00-036-0805). Undefined peaks in the 1000°C-sample are due to carbon from the graphite foil used in the SPS. Sintering temperature is presented at corresponding pattern.

The split in some of the peaks are due to $CuK_{\alpha 2}$, and becomes more apparent at high temperatures.

4.2.3 Microstructure

Density and porosity

Tab.4.2 presents the density and porosity results obtained at different SPS-temperatures, determined using Archimedes' method. The theoretical density used in the calculations was found to be 4.35 g/cm^3 (calculations in Appendix D). It is observed that all samples have a relative density around 98%, showing that with dwell time of five minutes and pressure of 50 MPa a dense material is achieved even at the lowest temperature, 850°C.

Table 4.2: Overview of the density and porosity at different SPS programs. Theoretical density of the rock-salt structure is 4.35 g/cm^3 (Appendix D). The pressure was 50 MPa and the dwell time 5 minutes in all experiments.

T[°C]	ρ_{bulk}[g/cm^3]	π_{open}[%]	π_{closed}[%]	π_{total}[%]	ρ_{rel}[%]
850	4.25	2.74	ca. 0	2.32	97.7
950	4.31	1.31	ca. 0	1.06	98.9
1000	4.29	1.58	ca. 0	1.38	98.6
1050	4.29	2.19	ca. 0	1.53	98.5
1150	4.28	1.84	ca. 0	1.79	98.2
1250	4.30	1.52	ca. 0	1.32	98.7

SEM images of the fracture surface of the sintered samples, Fig.4.6, confirm the high densities measured by Archimedes' method as no closed pores are observed. In addition, they clearly show intergranular fracture.

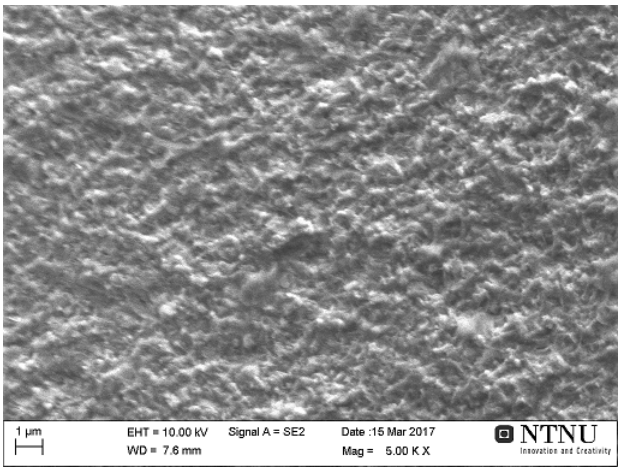

(a) 850°C, ρ=97.7%

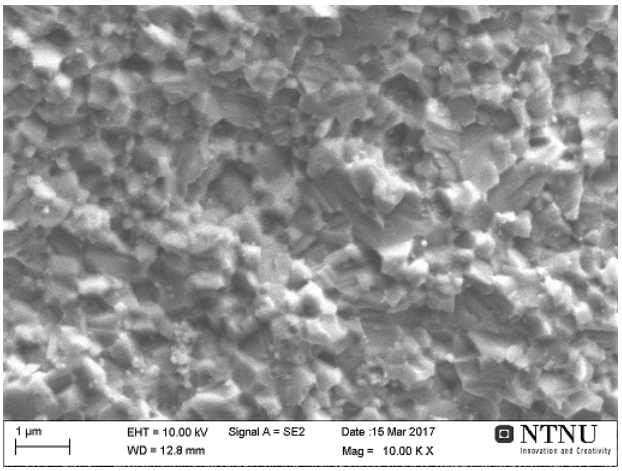

(b) 950 °C, ρ=98.9%

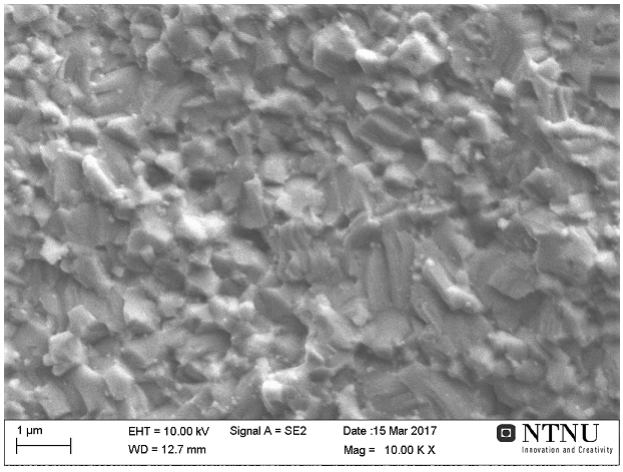

(c) 1000°C, ρ=98.6%

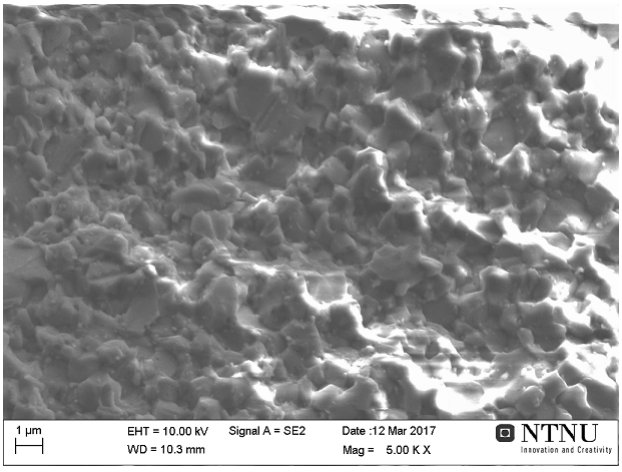

(d) 1050 °C, ρ=98.5%

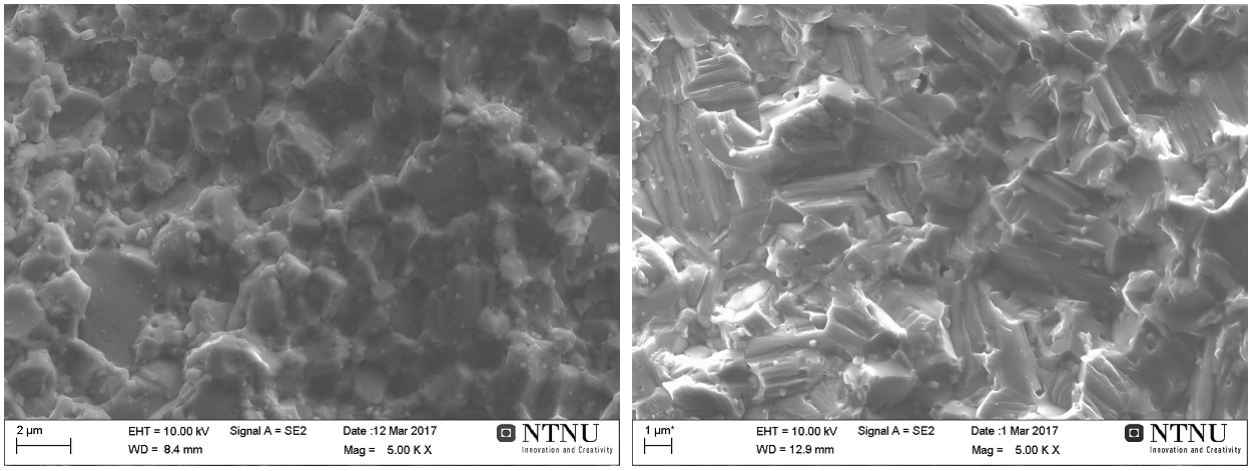

(e) 1150°C, ρ=98.2%

(f) 1250 °C, ρ=98.7%

Figure 4.6: SEM images of fracture surface, confirming high density samples. Sintering temperature and relative density are presented in each image.

Grain size

Grain size and grain boundaries were investigated in SEM on polished and thermally etched surfaces. Different etching programs were tested (Appendix E), which is why the samples sintered at 850°C, 950°C and 1250°C, Fig.4.7 (a), (b) and (f), are somewhat over-etched, making it challenging to see the grain boundaries. This is also the reason they do not look dense.

The images in Fig.4.7 (a) and (b) show a narrow particle size distribution, with grain sizes estimated to be 400 nm and 500 nm, respectively. The sample sintered at 1000°C, Fig.4.7 (c), also has relatively homogeneous grain size (approximately 700 nm), whereas the samples sintered at higher temperatures, Fig.4.7 (d), (e), (f), have a broader size distribution, with an average grain size of approximately 1.2 μm, 2.3 μm and 2.8 μm, respectively.

As expected, the grain size is larger at higher temperatures. The material is close to 100% dense even at the lowest sintering temperature, 850°C, which means that at higher temperatures, grain growth is the dominating phenomenon. The trend is presented in Fig.4.8. Some of the standard deviations illustrated in this graph are quite large as the size distributions are broad and the sizes are estimated based on images.

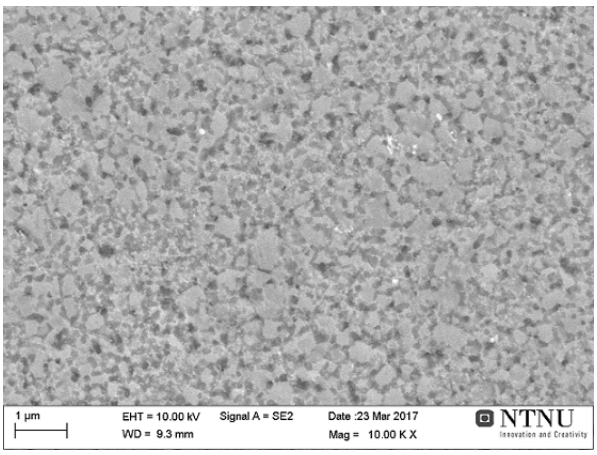

(a) 850°C, d=0.4μm

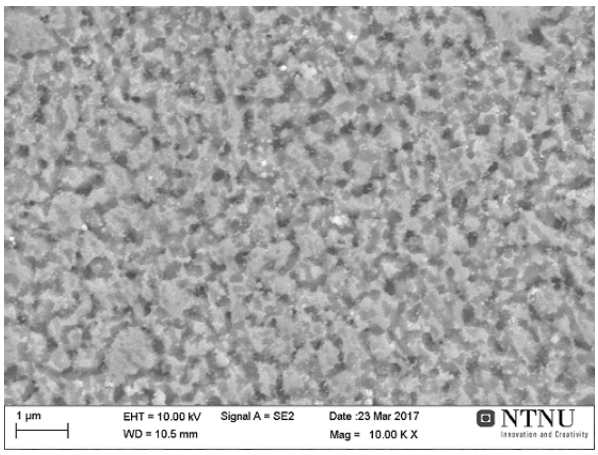

(b) 950 °C, d=0.5μm

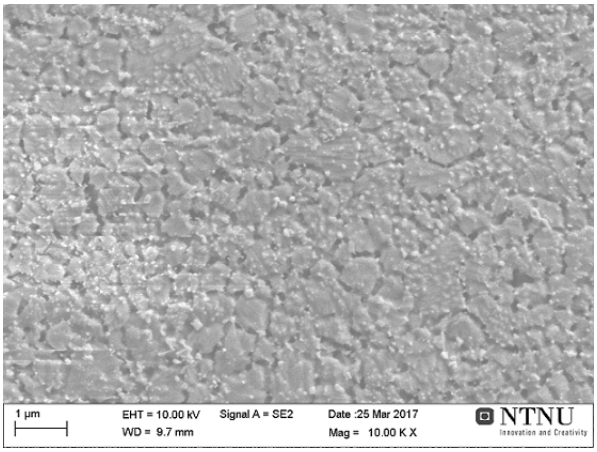

(c) 1000°C, d=0.7μm

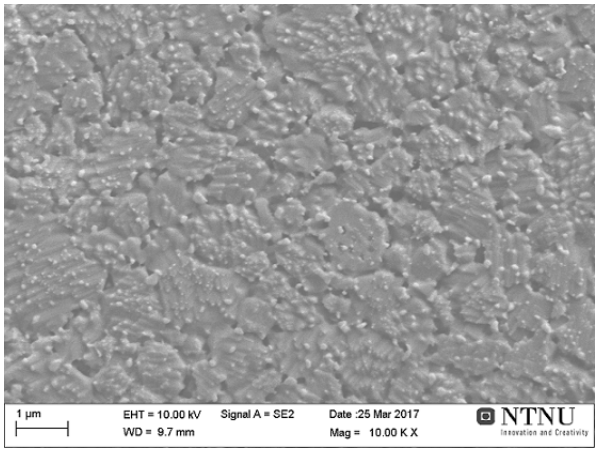

(d) 1050 °C, d=1.2μm

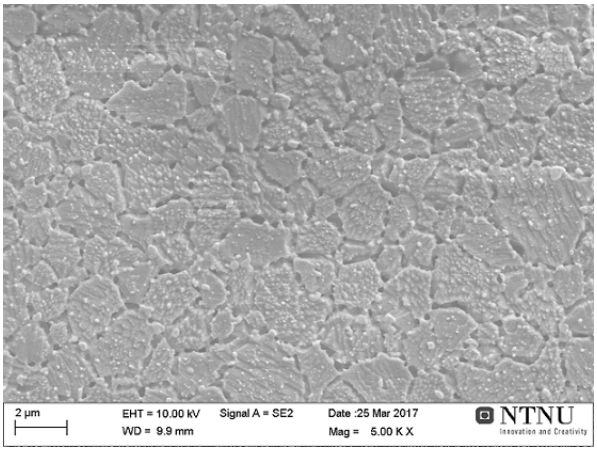

(e) 1150°C, d=2.3μm

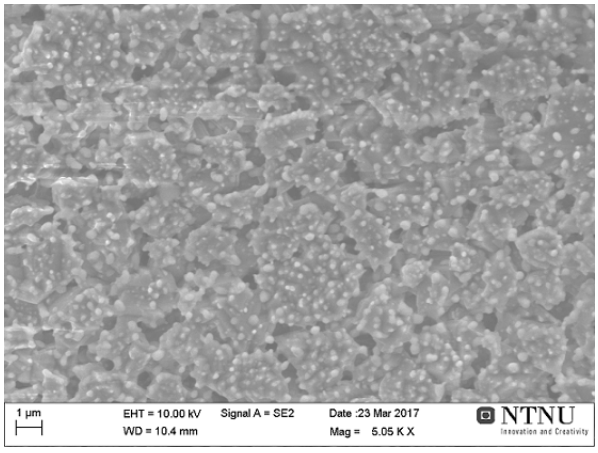

(f) 1250 °C, d=2.8μm

Figure 4.7: SEM images of polished and thermally etched surfaces. Sintering temperature and average grain size are presented in each image.

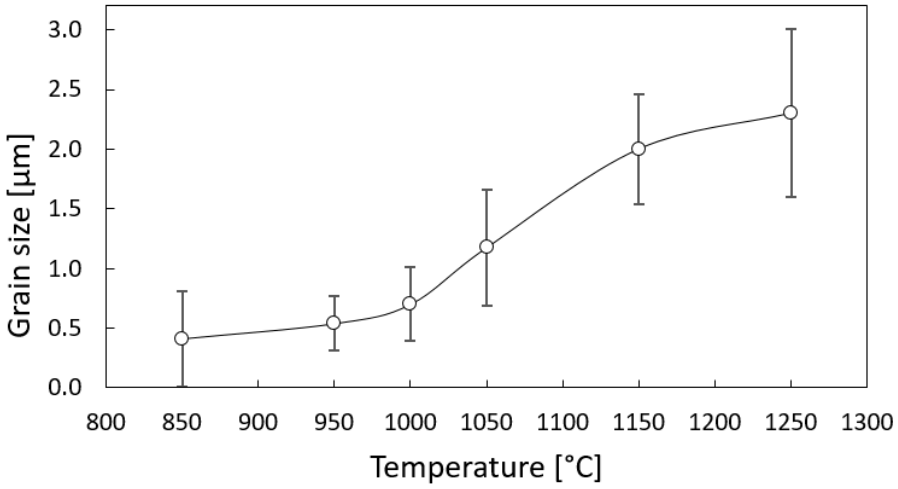

Figure 4.8: Average grain size in μm as a function of sintering temperature, including standard deviation bars.

Based on the XRD-results and calculations using TOPAS and Scherrer equation, the average grain sizes are found to be 49-101 nm for the main phase in the samples, which are much smaller than the observations from SEM images. This indicates that the observed grains are made up of smaller crystallites. The values of both phases are presented in Tab.4.3.

Table 4.3: Average crystallite size (d) in the samples sintered at given temperature. Pressure of 50 MPa and the dwell time 5 minutes in all experiment. Based on XRD-results and calculated using TOPAS Software. ±errors are calculated by the software.

T[°C]	d($Ca_{0.5}Mn_{0.5}O$) [nm]	d($CaTa_2O_6$) [nm]
850	49±1.2	8±0.5
950	101±2.7	12±0.4
1000	83±2.6	11±0.4
1050	67±2.7	14±0.9
1150	82±2.1	23±1.0
1250	95±2.3	26±1.1

Another interesting observation regarding the microstructure is the lamellar structure in each grain, which is also distinctly seen in Fig.4.6 (f). This is noticeable at all temperature except at 850°C and 950°C. There are also observed small white particles evenly distributed throughout the samples sintered at the four highest temperatures. In the samples sintered at 850°C and 950°C only a few white particles are seen.

4.3 Annealing

4.3.1 Determination of annealing program

HTXRD, DIL and TG analysis were conducted to investigate oxidation properties of $Ca_{0.5}Mn_{0.5}O$.

The HTXRD analysis were performed at temperatures between room temperature and 900°C, with scans at every 100°C increment. The results show rock-salt structure up to approximately 300°C, where the intensity decreases. Between 400°C and 500°C there are no intensity, indicating an amorphous structure. At a temperature between 500°C 560°C the perovskite structure starts to form, and at approximately 800°C the sample is fully oxidized and the perovskite structure complete. The secondary spinel-phase appears at the last scan at 900°C. The diffractograms at room temperature (start), 500°C, 800°C and 900°C (end) are shown in Fig.4.9. This analysis was performed on the CMTO-powder reduced at 800°C (hence the secondary phase with tantalum is not visible in the rock-salt as it start to appear at approximately 950°C).

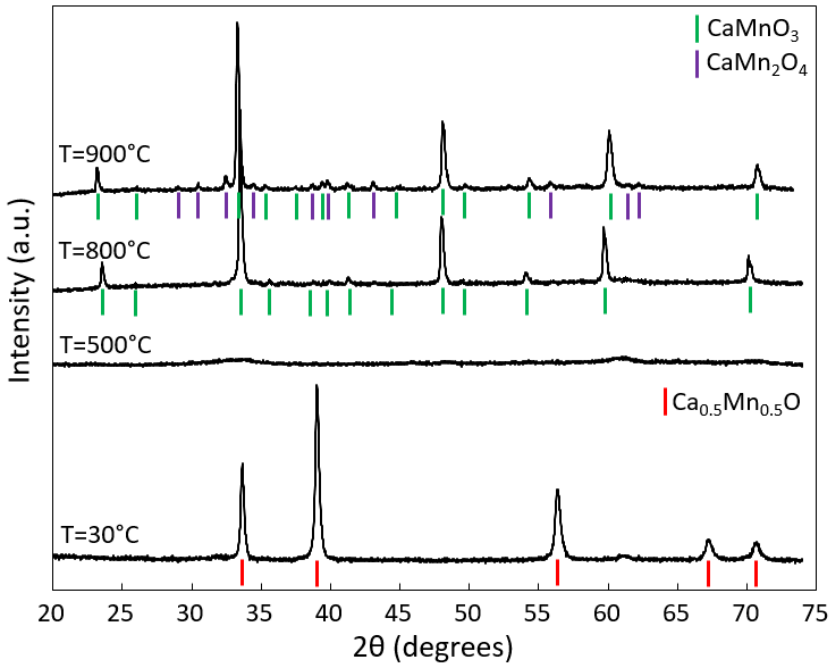

Figure 4.9: Selected results from the HTXRD analysis in air, showing transformation from reduced to oxidized material. At room temperature the material has rock-salt structure ($Ca_{0.5}Mn_{0.5}O$). At 500°C, the intensity has decreased and is almost zero. At 800°C the perovskite ($CaMnO_3$) has formed, and at 900°C the secondary spinel phase (marokite = $CaMn_2O_4$) has additional been formed.

In the **DIL measurements**, which were performed on sintered samples, 1300°C was chosen as maximum temperature, 2K/min as heating and cooling rate, and one hour dwell time. Analyses were performed on two samples, T_{sps}=950°C and T_{sps}=1250°C, but as the results were similar, 950°C-results are given in Appendix F and only the results from the sample sintered at highest temperature are presented in this section. Fig.4.10 displays these results. They show rapid expansion that starts at about 700°C, indicating the start of the oxidation process, and ends in fracture of the sample at 820°C. Inspection of the sample after the analysis clearly showed disintegration. The curve shows further expansion over T=820°C, but it takes place at much slower rate, that could be associated with introduction of secondary phase. No more cracks seem to be induced over 820°C or upon cooling. The change in slope upon cooling is due to the phase transition from cubic to tetragonal structure, which according to theory occurs at 913°C[19].

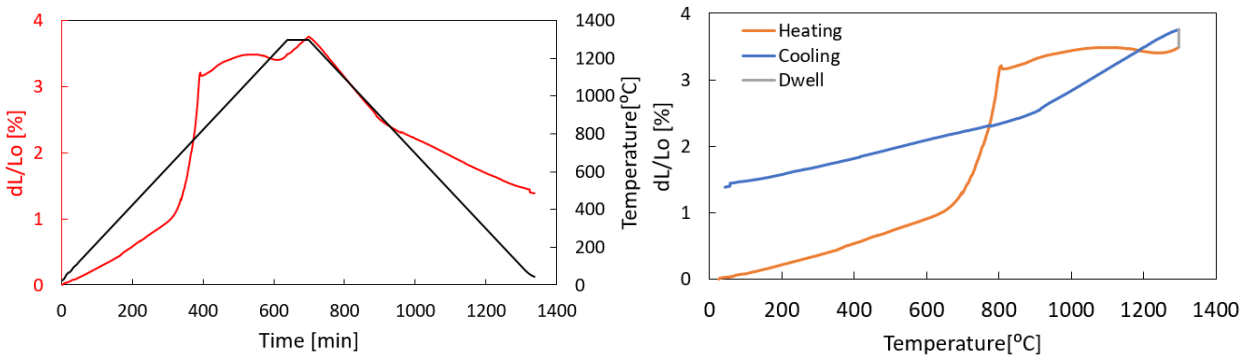

(a) (b)

Figure 4.10: Investigation of oxidizing properties of the sintered rock-salt structure. DIL–analysis in air with 1300 °C as maximum temperature, heating- and cooling rate 2°C/min, and 1h dwell time. The sample analyzed was sintered at 1250°C and was highly dense.

XRD analysis confirms that the samples from the DIL are fully oxidized, and both the perovskite and the spinel phase are present, as presented in the diffractogram in Fig.4.11.

For **TG analysis** the same heating program as applied in DIL measurements was used: maximum temperature of 1300°C, heating- and cooling rate of 2°C/min and one hour dwell time. The resulting curves are presented in Fig.4.12 and show that mass increase, i.e. oxidation, starts at 400°C. The mass increase is nearly stabilized between 730°C and 850°C, before it decreases as the temperature is further increased. At maximum temperature, equilibrium is reached. Upon cooling, the mass increases again, as the structure picks of oxygen, and at approximately 730°C,

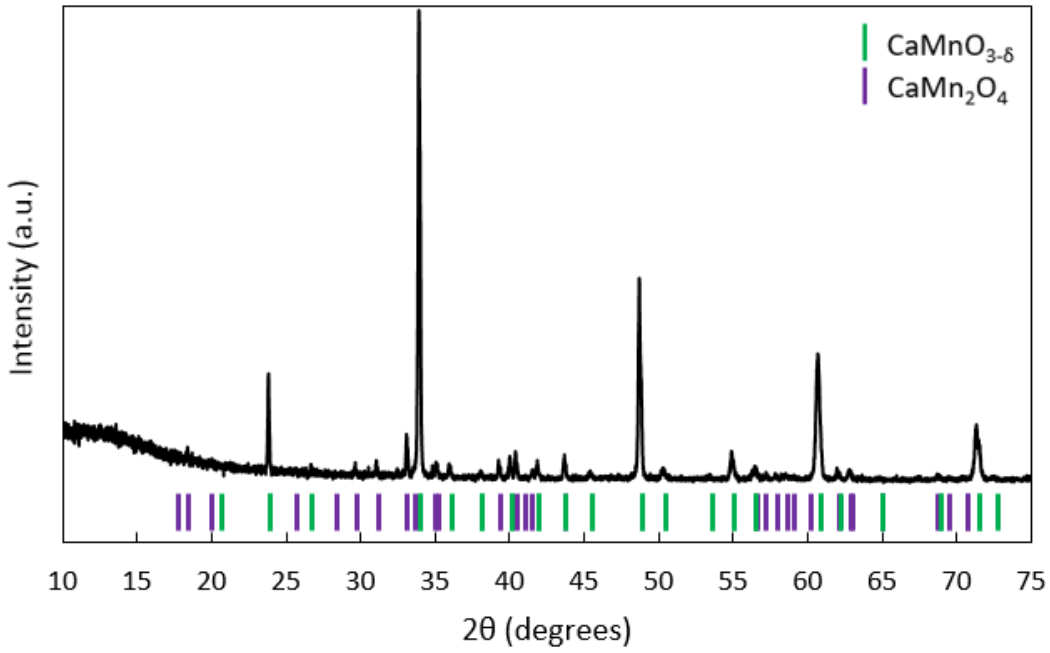

Figure 4.11: XRD result of the sample oxidized during DIL measurements in air with maximum temperature of 1300°C. The samples is completely oxidized with the perovskite phase (PDF 01-070-7306) marked in green and the secondary marokite phase (PDF 04-014-8192), marked in purple.

from where the mass-curve remains constant, the structure is completely filled with oxygen.

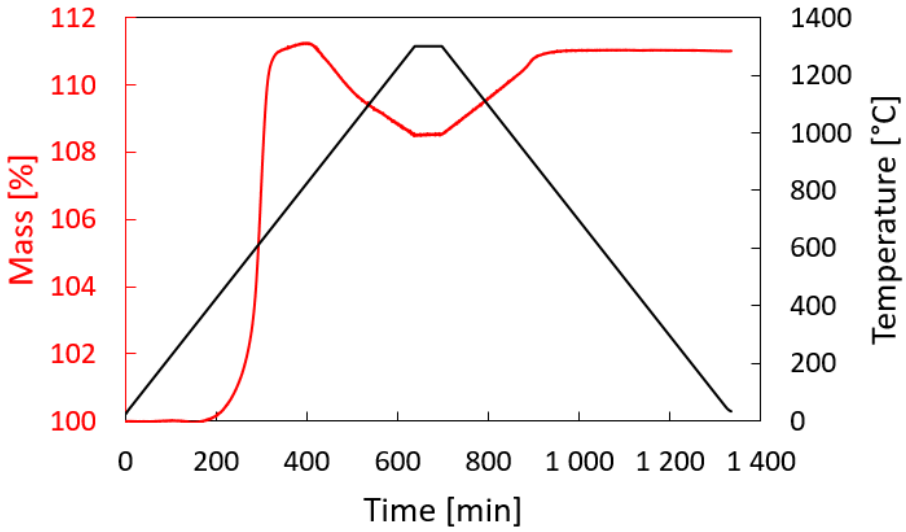

Figure 4.12: TG analysis of crushed pellet sintered at 1250°C, in air with 1300°C as maximum temperature, heating- and cooling rate 2°C/min, and 1h dwell time.

Based on HTXRD, DIL and TG results, an annealing program for the spark plasma sintered

samples were determined. It was established that annealing only in air is not possible and some additional treatment is required to prevent cracking. Hence, it was determined that the heating of the samples would take place in inert atmosphere, before changing the gas to synthetic air. Maximum temperature was chosen to be 1100°C for the all samples. As the HTXRD analysis showed that the secondary phase in the oxidized state forms at around 900°C, the temperature should be higher. In addition, by applying high temperature, the risk of cracking is lower as creep might be induced.

First, dwell of three hours was chosen, as the analysis results shows that the reaction occurs relatively fast, and the desired secondary phase is obtained shortly after reaching 900°C. However, after three hours XRD-analysis showed traces of the rock-salt phase, as presented in Fig.4.13, and the samples cracked. By inspecting the sample after annealing, it was possible to see a difference between the core and the structure around. Hence, the dwell time was increased to six hours, which resulted in complete oxidation, Fig.4.14. To lower the risk of cracking, slow cooling rate (50°C/h) was used. Microcracks were still observed in some samples.

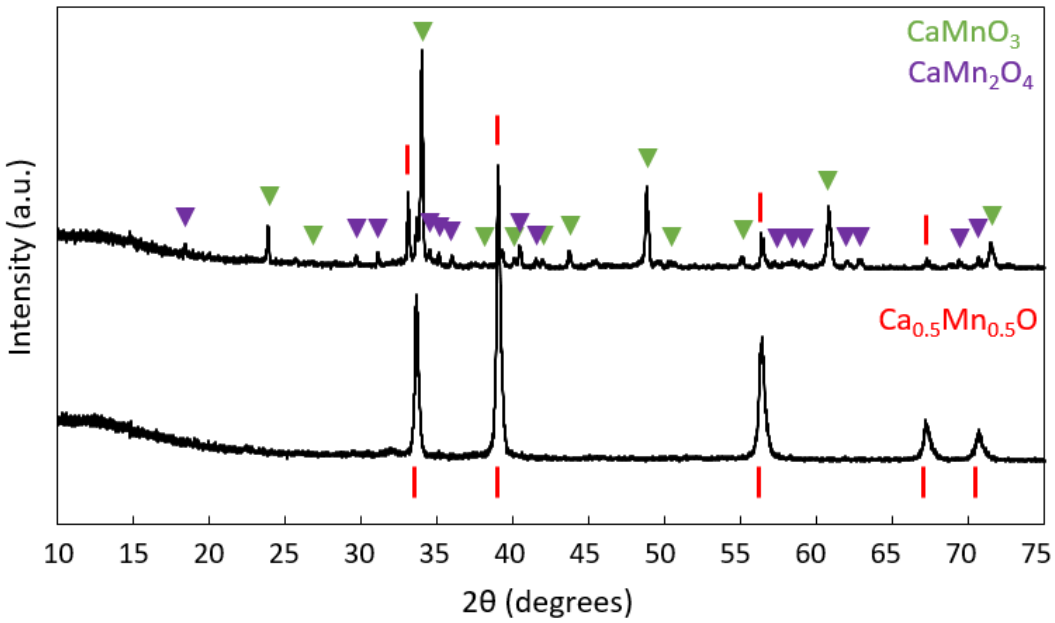

Figure 4.13: XRD-result of the sample sintered at 1250°C and annealed in air for 3 hours, showing incomplete oxidation as rock-salt (red marks) is still present in the pattern of the annealed sample (top diffractogram).

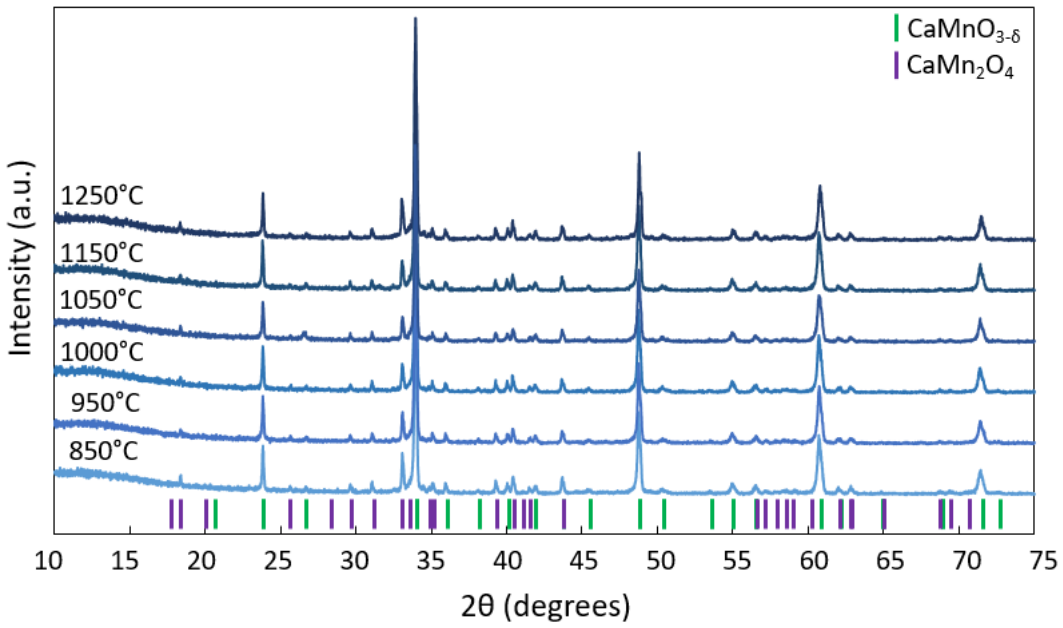

Figure 4.14: XRD-results of the samples annealed in air for 6 hours, showing complete oxidation with only $CaMnO_{3-\delta}$ (PDF 01-070-7306) and $CaMn_2O_4$ (PDF 04-014-8192) present. Sintering temperature is presented at corresponding pattern.

4.3.2 Density and porosity

The relative density of the annealed samples were determined by using Archimedes measurements and a theoretical density of 4.7 g/cm^3 (Appendix.D). Tab.4.4 presents an overview of densities and porosities of CMTO obtained after annealing of the samples sintered at different temperatures. The values show that all samples are still highly dense, with a relative density of 95%. However, this is a small decrease from the as-sintered samples with densities around 98%.

Table 4.4: Overview of the density and porosity of samples annealed at 1100°C for 6h. Theoretical density 4.70 g/cm^3 (Appendix.D).

T_{sps}[°C]	ρ_{bulk}[g/cm^3]	π_{open}[%]	π_{closed}[%]	π_{total}[%]	ρ_{rel}[%]
850	4.47	2.78	2.05	4.83	95.2
950	4.48	0.00	4.70	4.70	95.3
1000	4.47	1.77	3.08	4.85	95.1
1050	4.46	0.00	5.01	5.01	95.0
1150	4.44	0.90	4.58	5.48	94.5
1250	4.47	2.45	2.55	5.00	95.0

In addition to density calculations, pores were studied in SEM. Images of the fracture surfaces are presented in Fig.4.15, and they show a relative amount of pores consistent with ap-

proximately 5%, meaning that they support the high density measured by Archimedes' method.

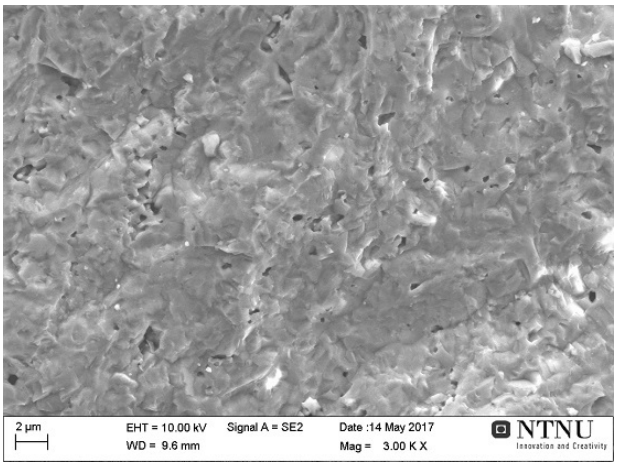

(a) 850°C, ρ=95.2%

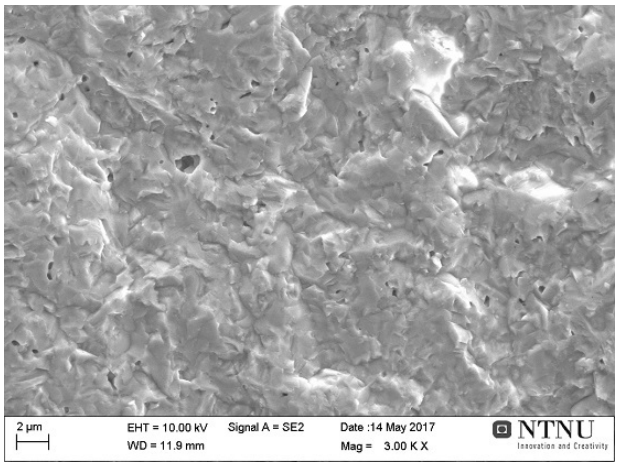

(b) 950 °C, ρ=95.3%

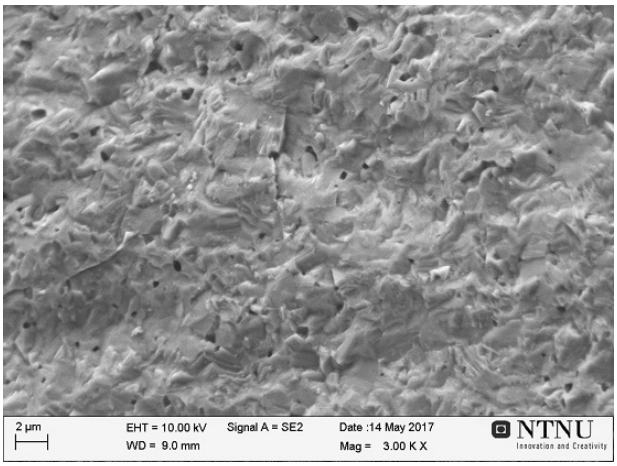

(c) 1000°C, ρ=95.1%

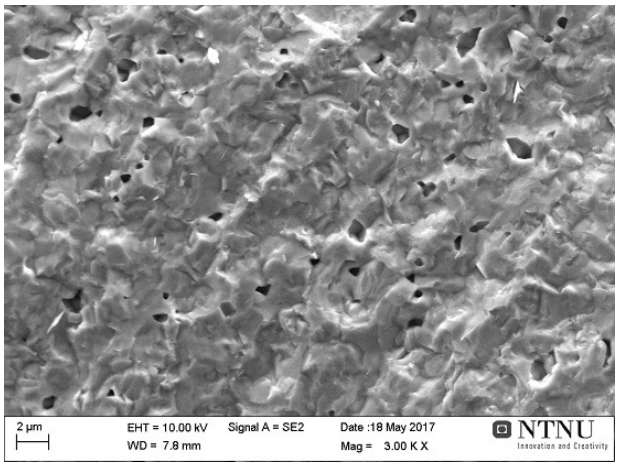

(d) 1050 °C, ρ=95.0%

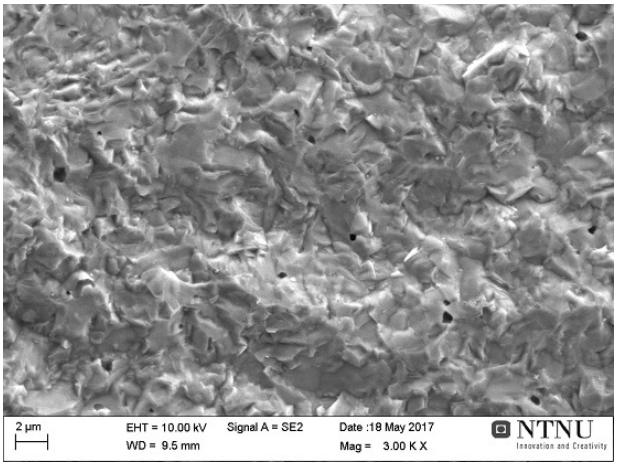

(e) 1150°C, ρ=94.5%

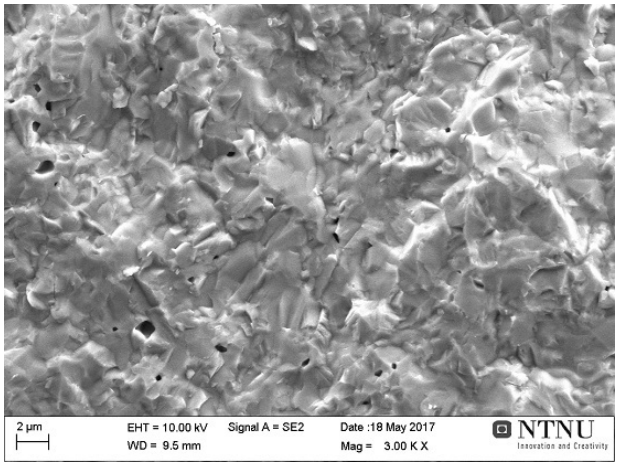

(f) 1250 °C, ρ=95.0%

Figure 4.15: SEM images of fracture surface of oxidized samples, showing high density. Sintering temperature and relative density are presented in each image.

4.3.3 Grain size

Grain size and grain boundaries of oxidized samples were studied in SEM. Fig.4.17 shows the results from SE images of thermally etched surfaces. From these images, a broad size distribution is observed in all samples, but the difference is most evident in Fig.4.17(f) showing the sample sintered at the highest temperature. In this sample, the grain size varies from approximately 440 nm to 3.3 μm, while the sample sintered at the lowest temperature shows sizes between 300 nm and 1.6 μm. The broad size distribution is due to the difference in grain growth between the secondary phase and the main phase. Hence, when estimating the average grain size, one size is given for CMO and one size for marokite, as in Fig.4.16, which presents grain size as a function of sintering temperature.

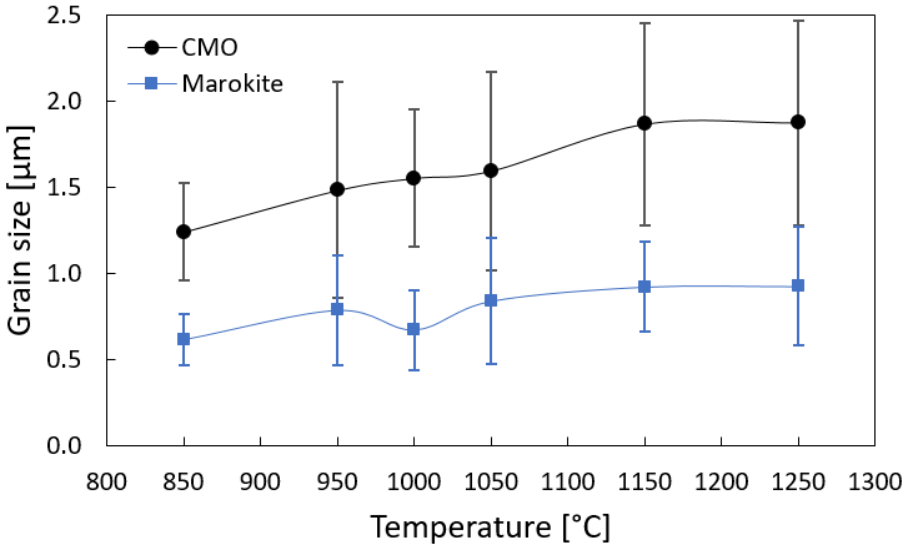

Figure 4.16: Average grain size of oxidized samples as a function of sintering temperature, including standard deviation bars. Black points: CMO. Blue points: secondary phase, marokite.

This plot shows that marokite has smaller grains than CMO at all sintering temperatures. In addition, it is observed that the grains generally grow with increasing temperature. The grains of CMO grow from the average grain size of 1.2 μm to 1.9 μm, while the grains of marokite grow from 0.6 μm to 0.9 μm, showing that the growth rate is slightly higher for CMO. The average grain sizes are estimated from both SE images, Fig.4.17, and BSE images, Fig.4.18, as it for some samples were difficult to distinguish between the two phases in the SE images. The plot in Fig.4.16

includes standard deviation bars, where some of them are relatively large as the size distribution is quite broad, even within the same phase, and the sizes are estimated based on images.

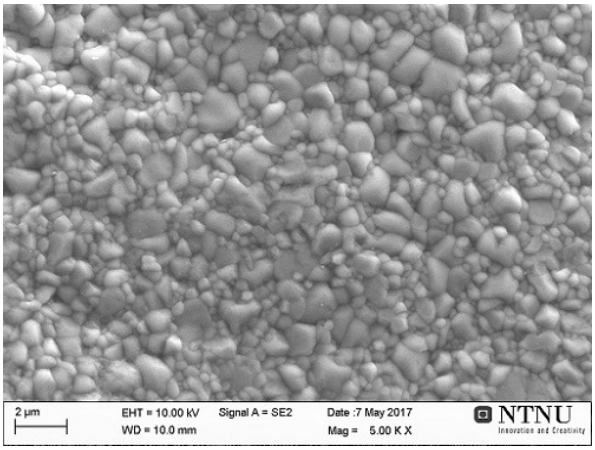

(a) 850°C

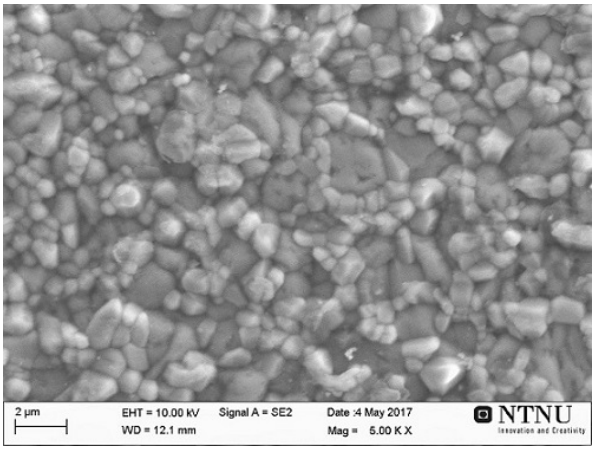

(b) 950°C

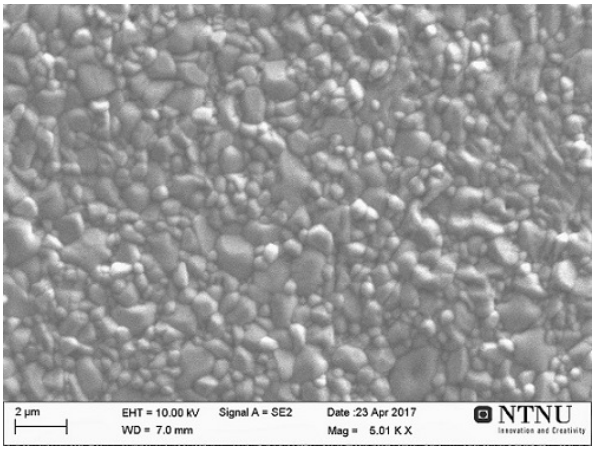

(c) 1000°C

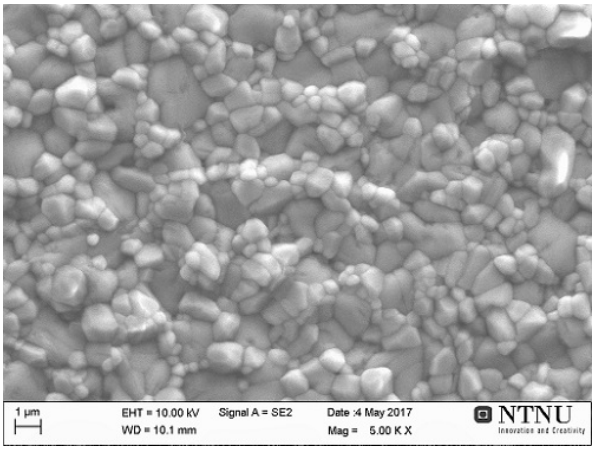

(d) 1050°C

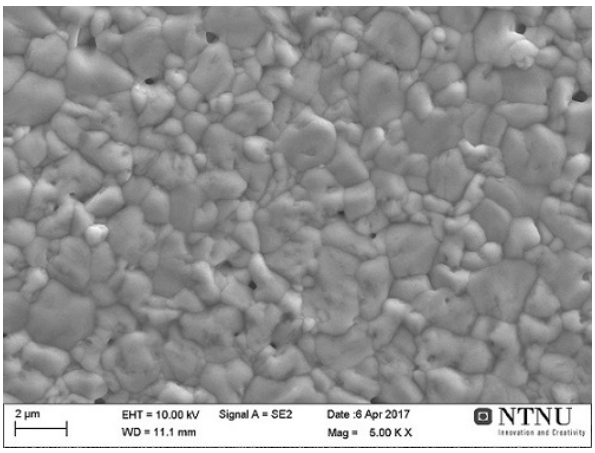

(e) 1150°C

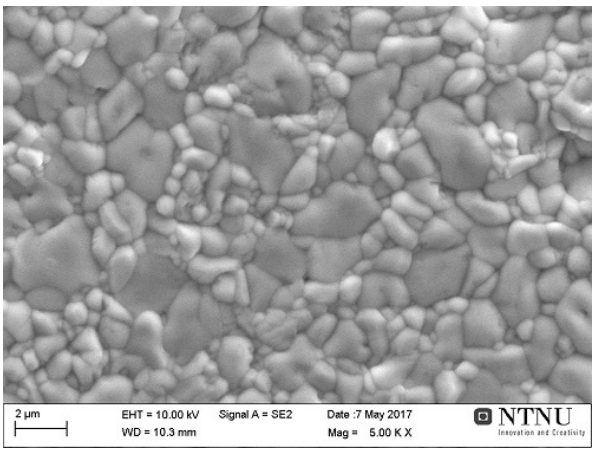

(f) 1250°C

Figure 4.17: SEM images of the surface of oxidized samples. Sintering temperature is presented in each image.

In addition to SEM images, crystallite sizes were found based on XRD-results, using Rietveldt analysis and Scherrer equation in Topas. The results are presented in Tab.4.5, and show that the secondary marokite phase has larger crystallites than the main CMO phase. The crystallite sizes of CMO are around 90 nm in all samples, while marokite has sizes between 95 nm and 123 nm. This is significantly smaller than the grain sizes observed in SEM images, indicating that the observed grains consist of many crystallites.

Table 4.5: Average crystallite size (d) in the oxidized samples sintered at given temperature. Based on XRD-results and calculated using TOPAS Software. ±errors are calculated by the software.

T[°C]	d($CaMnO_{3-\delta}$) [nm]	d ($CaMn_2O_4$)[nm]
850	86±2	105±5
950	87±2	116±6
1000	92±2	121±7
1050	90±2	111±7
1150	93±2	123±7
1250	87±2	95±4

4.3.4 Secondary phases

As presented, the result from HTXRD gives information about the formation of the secondary phase, marokite. It shows that marokite forms at a temperature between 800°C and 900°C, and that it is exsolved after the complete formation of perovskite CMO.

To study the exsolution of the secondary phase, BSE images were collected. The results are shown in Fig.4.18, where thermally etched samples are to the left and polished surfaces to the right. The sintering temperature is given in each image.

In the samples sintered at the four lowest temperatures, 850°C, 950°C, 1000°C and 1050°C, an evident difference between the main phase, $CaMnO_3$, and the secondary marokite phase, $CaMn_2O_4$, is seen, both in terms of morphology and contrast. The etched samples sintered at 950°C and 1050°C clearly show that marokite, the light grey phase, forms in much smaller grains than the CMO, which is opposite of the results conducted from the XRD-results, Tab.4.5. EDS point analysis confirms the same trend in the samples sintered in 850°C and 1000°C, although it is not clearly seen from the images. The images also show that marokite forms in clusters around the CMO-grains, and in some cases appears to be the continuous phase, Fig.4.18(d).

In the sample sintered at 1150°C, Fig.4.18 (i) and (j), it is difficult to see any marokite, and it is not detected either in EDS point analysis or line scan. In the sample sintered at 1250°C there is a clear contrast between the phases in BSE images of both thermally etched surface and polished surface, Fig.4.18 (k) and (l), and a similar trend as in 950°C and 1050°C with marokite surrounding CMO is observed.

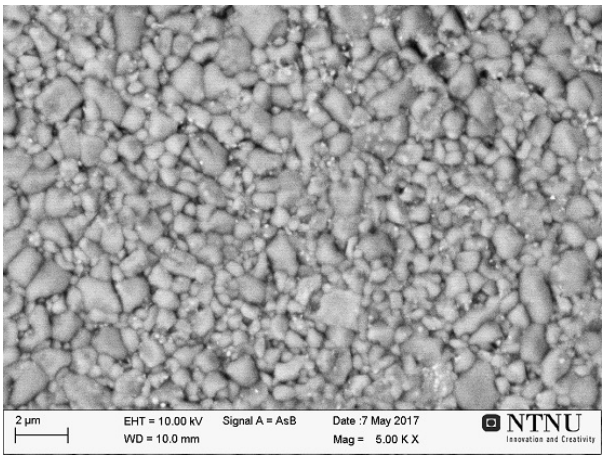

(a) 850 °C

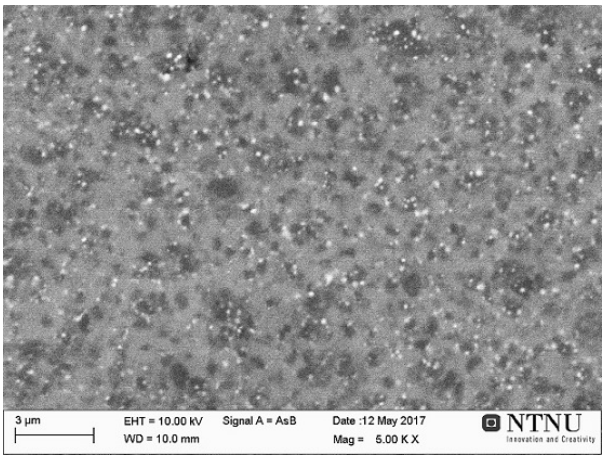

(b) 850 °C

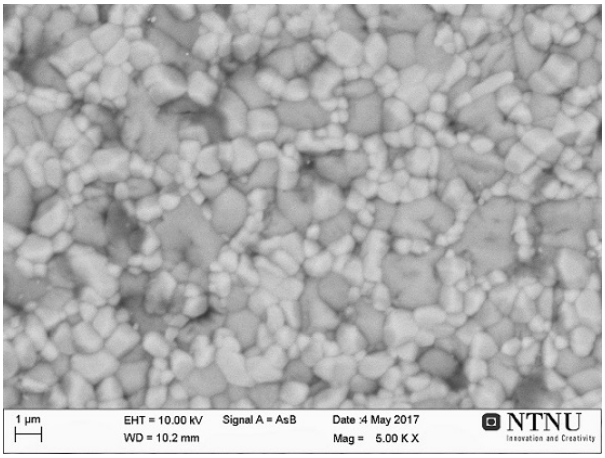

(c) 950°C

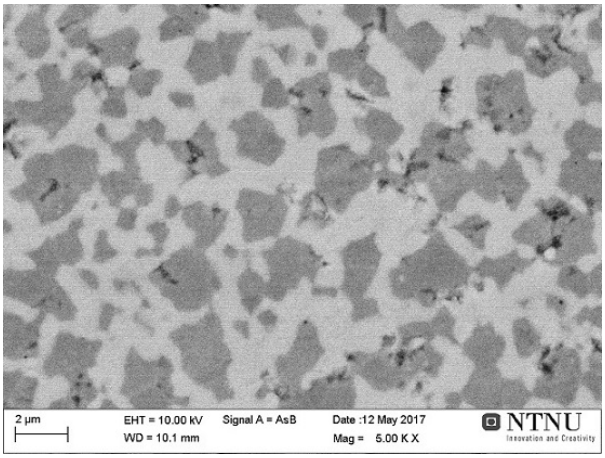

(d) 950°C

Figure 4.18: BSE SEM images of the surface of oxidized samples, thermally etched surface to the left and polished surface to the right. Sintering temperatures are presented in each image. Dark gray=CMO, light grey=$CaMn_2O_4$, white=$CaTa_2O_6$.

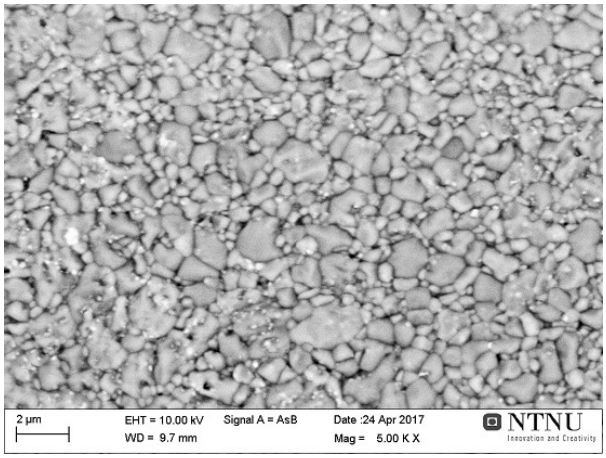

(e) 1000°C

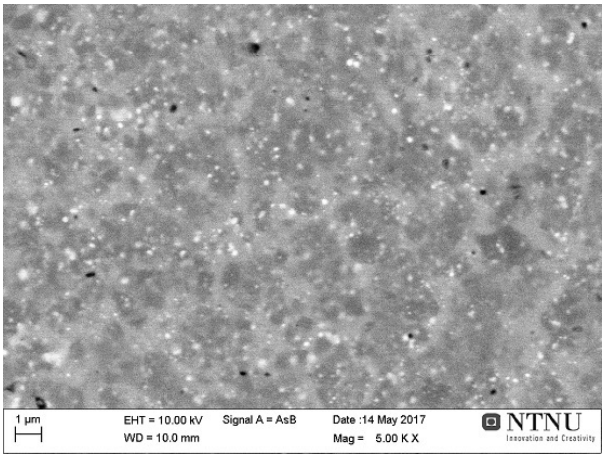

(f) 1000°C

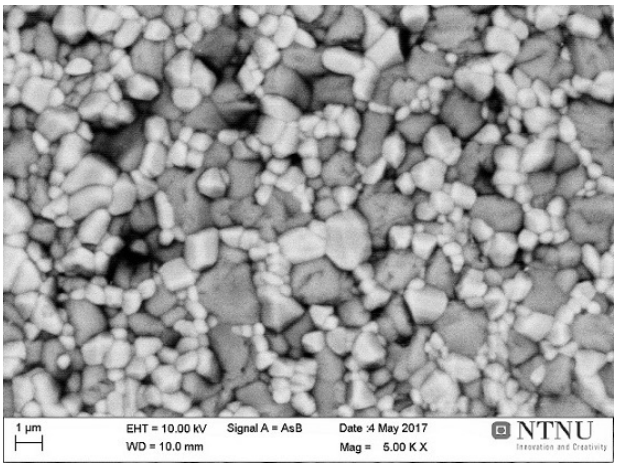

(g) 1050 °C

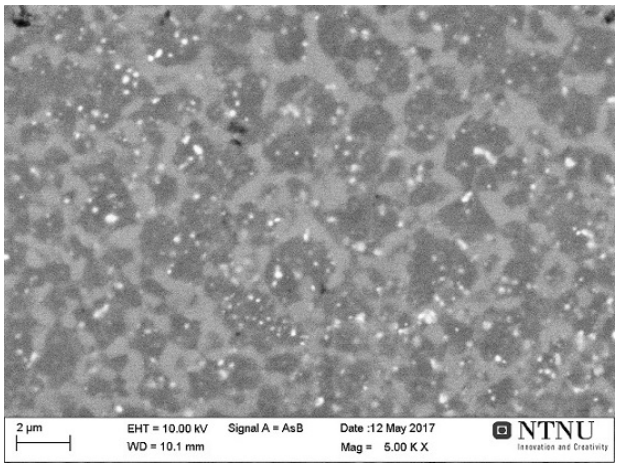

(h) 1050 °C

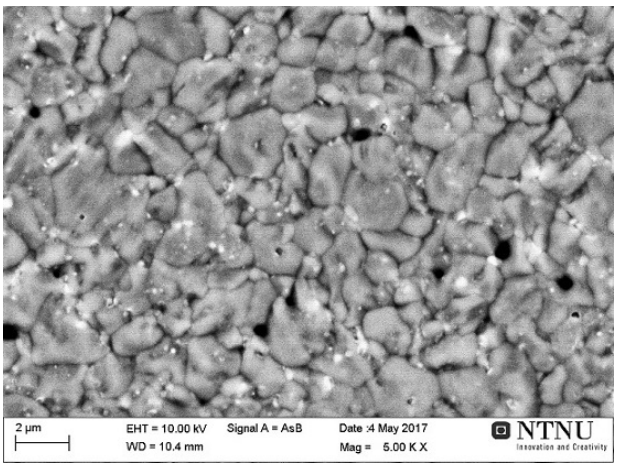

(i) 1150°C

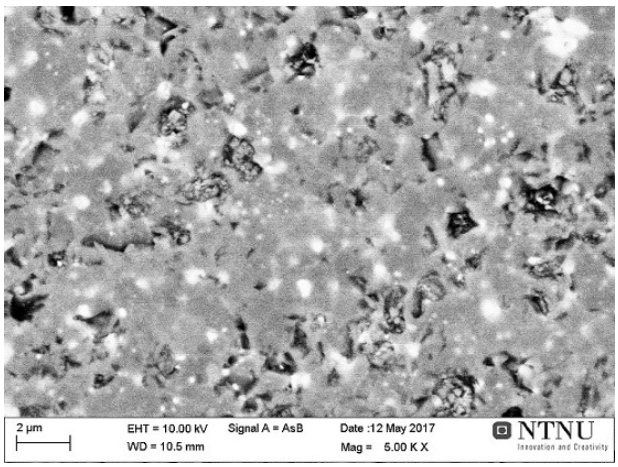

(j) 1150°C

Figure 4.18: BSE SEM images of the surface of oxidized samples, thermally etched surface to the left and polished surface to the right. Sintering temperatures are presented in each image. Dark gray=CMO, light grey=$CaMn_2O_4$, white=$CaTa_2O_6$.

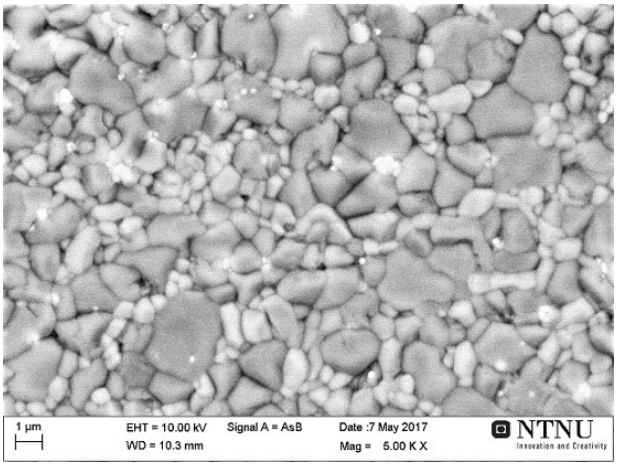

(k) 1250 °C

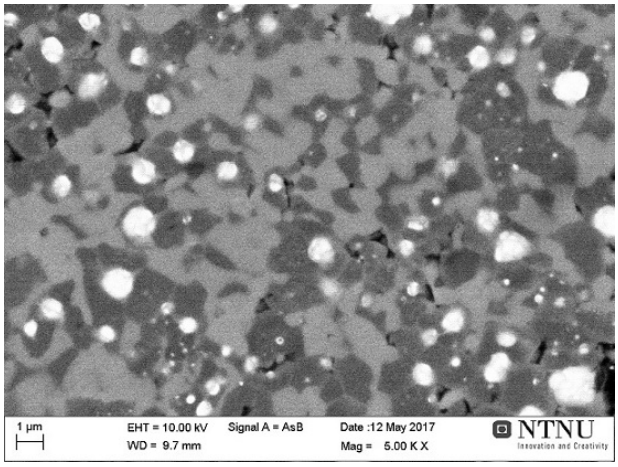

(l) 1250 °C

Figure 4.18: BSE SEM images of the surface of oxidized samples, thermally etched surface to the left and polished surface to the right. Sintering temperatures are presented in each image. Dark gray=CMO, light grey=$CaMn_2O_4$, white=$CaTa_2O_6$.

The relative amount of marokite was calculated using TOPAS software and Rietveld refinement based on the patterns from the XRD analyses. These results, presented in Tab.4.6, confirm a high content of marokite in all samples, including the 1150°C-sample where no marokite was detected by EDS. The largest amount of 25 vol% is detected in the sample sintered at the highest temperature, 23 vol% is observed in the sample sintered at the loweste temperature, while all other samples have a relative amount of around 20 vol%. However, most SEM images imply an even higher amount of secondary phase.

Table 4.6: Relative amount of phases in annealed samples, found from XRD results by using TOPAS.

T_{SPS} [°C]	Amount [vol%]	
	$CaMnO_{3-\delta}$	$CaMn_2O_4$
850	77	23
950	80	20
1000	81	19
1050	81	19
1150	81	19
1250	75	25

In addition to CMO and marokite, small white particles are observed in the etched samples sintered at 850°C, 1000°C, 1150°C and 1250°C, and they become more evident the higher the sintering temperature. These white areas are easily detected in polished surfaces, and are visible

in all samples except in the one sintered at 950°C. EDS analyses show that this phase is rich in Ta and has a higher content of Ca than Mn, implying that this is the same phase as observed in the as-sintered samples: $CaTa_2O_6$. All values from the EDS point analyses are presented in Tab.4.7, where "White", "Light grey" and "Dark grey", corresponding to $CaTa_2O_6$, $CaMn_2O_4$ and $CaMnO_3$ respectively, describe which area in the SEM image of polished surfaces the values correspond to. "X" means that no area of that color was observed.

Element	Atomic%		
	White	Light grey	Dark grey
O	55.50	51.39	54.85
Ca	22.69	18.34	22.66
Mn	21.36	30.19	22.38
Ta	0.35	0.09	0.11

(a) T_{sps}=850°C

Element	Atomic%		
	White	Light grey	Dark grey
O	x	52.41	54.93
Ca	x	17.14	22.65
Mn	x	30.46	22.8
Ta	x	0	0.05

(b) T_{sps}=950°C

Element	Atomic%		
	White	Light grey	Dark grey
O	57.27	54.15	56.41
Ca	21.76	17.30	21.87
Mn	20.29	28.46	21.61
Ta	0.69	0.10	0.10

(c) T_{sps}=1000°C

Element	Atomic%		
	White	Light grey	Dark grey
O	56.75	52.95	55.22
Ca	22.56	17.85	22.39
Mn	19.75	29.12	22.29
Ta	0.93	0.09	0.11

(d) T_{sps}=1050°C

Element	Atomic%		
	White	Light grey	Dark grey
O	50.61	x	53.78
Ca	25.59	x	23.14
Mn	23.35	x	22.94
Ta	0.46	x	0.17

(e) T_{sps}=1150°C

Element	Atomic%		
	White	Light grey	Dark grey
O	53.96	51.57	54.01
Ca	24.61	17.31	23.20
Mn	18.41	31.12	22.78
Ta	3.03	0.02	0.02

(f) T_{sps}=1250°C

Table 4.7: Values from EDS point analyses. Sintering temperatures are given for each table. "White", "Light grey" and "Dark grey", corresponding to $CaTa_2O_6$, $CaMn_2O_4$ and $CaMnO_3$ respectively, describe which area in the SEM image of polished surfaces the values correspond to. "X" means that no area of that color was observed.

Fig.4.19 shows EDS line scans of the samples sintered at 1050°C and 1250°C, Fig.4.18(b) and Fig.4.18(l) respectively. The element profile plots present weight percent on the y-axis and distance from point 1 on the x-axis.

Both element profile plots show a decrease in the weight percentage Mn as the composition changes from $CaMn_2O_4$ (light grey area) to $CaMnO_3$ (dark grey area). The amount of Ta is con-

firmed to be significantly higher in the white areas, presented with the peak in the light blue line. In addition, the amount of Mn is further decreased in these phases. The amounts of Ta in the $CaMnO_3$-phase is low and close to zero in the $CaMn_2O_4$-phase.

Same behavior is observed in all samples where the three phases are present, presented in Appendix G, but is most evident in these samples.

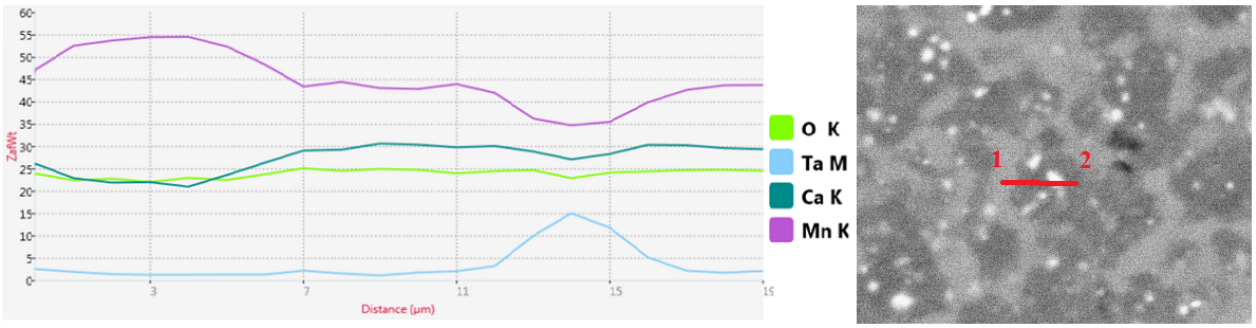

(a) T_{sps}=1050°C

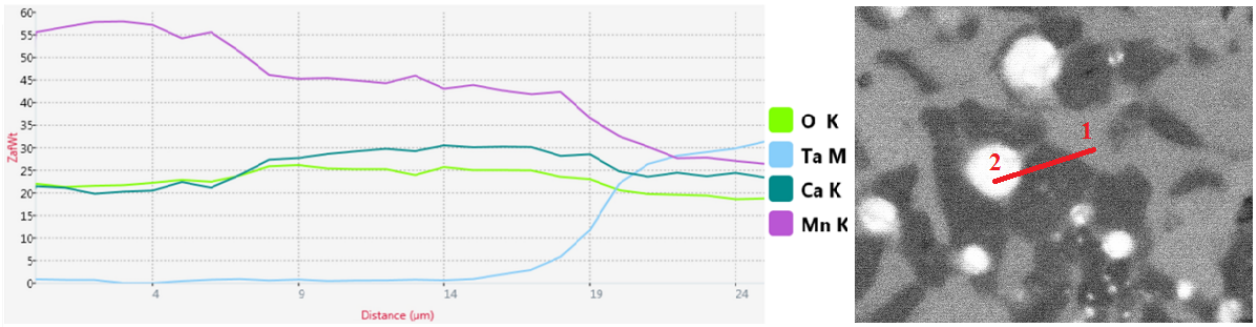

(b) T_{sps}=1250°C

Figure 4.19: Element profile plot from EDS line scan of polished sample sintered at 1050°C and 1250°C. Analysis along red line from point 1 to 2. Dark gray=CMO, light grey=$CaMn_2O_4$, white=$CaTa_2O_6$.

4.4 Thermal expansion coefficient

DIL measurements of $Ca_{0.5}Mn_{0.5}O$ in N_2 and CMTO in air were conducted to investigate if the cracking of the samples during annealing was due to difference in thermal expansion coefficient (TEC) between the reduced phase and the oxidized phase. Based on the slope of the curves, TEC was calculated using Eq.3.1.

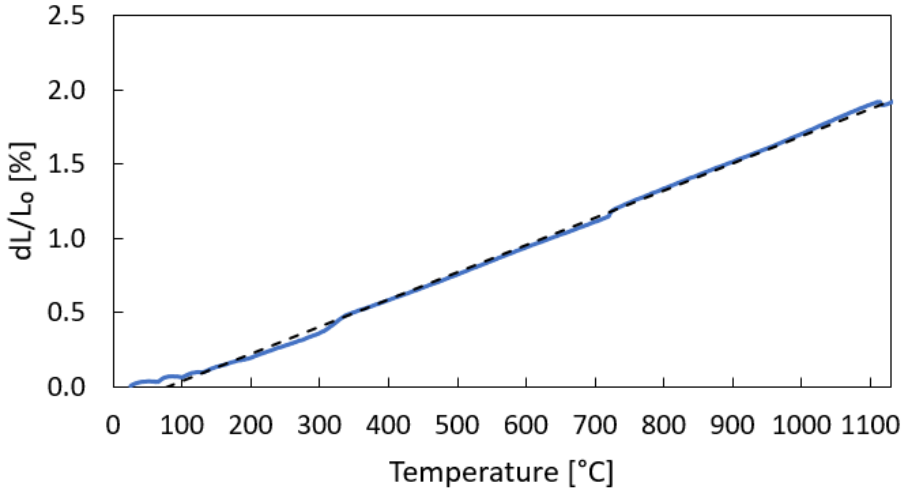

(a) DIL–analysis in N_2 of sintered $Ca_{0.5}Mn_{0.5}O$. Dotted lines represent the curve the calculation of TEC is based on. TEC=$18{\cdot}10^{-6}K^{-1}$.

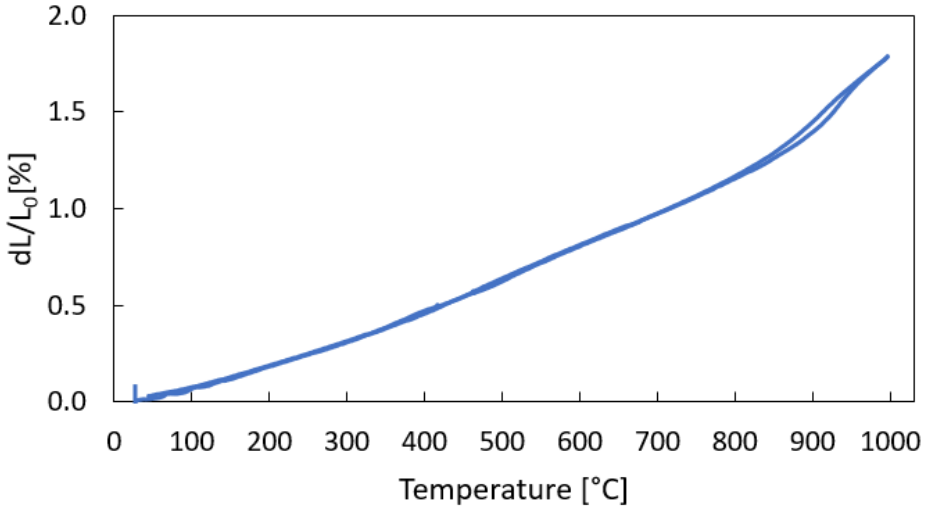

(b) DIL–analysis in air of sintered CMTO. TEC varies.

Figure 4.20: Investigation of thermal expansion coefficient (TEC).

Fig.4.20 (a) shows the result of sintered $Ca_{0.5}Mn_{0.5}O$, with a calculated TEC of $18{\cdot}10^{-6}$ °C^{-1}. Maximum temperature was set to 1300°C, but the sample melted at approximately 1280, which

is due to eutectic point at 1287°C in the CaO-MnO-Al_2O_3 phase diagram, presented in Appendix H. Alumina is from the alumina spacers placed at each end of the sample. TEC was therefore calculated from the heating curve prior to the melting, between room temperature and 1100°C.

Fig.4.20 (b) shows the obtained curve from analysing oxidized CMTO, and Tab.4.8 presents the resulting TEC values. The curve was divided into six temperature regions due to noticeable changes in the slope, hence six TECs. It can be observed that the change in slope occurs at nearly the same temperature upon heating and cooling. The change in slope around 850°C upon cooling is due to the phase transformations from cubic to tetragonal to orthorombic structure. TEC values upon cooling were also used in thermal conductivity measurements.

Table 4.8: Thermal expansion coefficients (TEC) for selceted temperature intervals obtained through DIL measurements of CMTO in air.

	Temperature [°C]	TEC [$°C^{-1}$]
Heating	25–380	$12.9 \cdot 10^{-6}$
	380–880	$17.5 \cdot 10^{-6}$
	880–1000	$41.5 \cdot 10^{-6}$
Cooling	1000–850	$35.1 \cdot 10^{-6}$
	850–350	$16.8 \cdot 10^{-6}$
	350–25	$12.6 \cdot 10^{-6}$

The TEC value for the reduced material is higher than the TEC values for the oxidized material at temperatures below around 850°C. At higher temperatures the thermal history of the material is of significance, and might affect the value.

4.5 Thermoelectric properties

This section presents the electrical conductivity, the Seebeck coefficient and the thermal conductivity of some chosen samples. Samples sintered at 850°C, 1000°C and 1250°C were characterized in order to compare properties at the lowest and the highest sintering temperature, in addition to a temperature in between. They all have well-defined structures after annealing, and they all consists of the three phases $CaMnO_3$, $CaMn_2O_4$ and $CaTa_2O_6$. Tab.4.9 shows details about the samples characterized.

Table 4.9: Samples chosen for thermoelectric characterization.

Sample-ID	T_{sps} [°C]	Density [%]	Grain size CMO [μm]	Grain size marokite [μm]
T850	850	95	1.2	0.6
T1000	1000	95	1.6	0.7
T1250	1250	95	1.9	0.9

4.5.1 Electrical conductivity

Electrical conductivity results are presented in Fig.4.21. The values are obtained upon cooling from 900°C to room temperature in air. The data obtained from the entire measurement is shown in Appendix I.

The plot shows that samples sintered at 850°C and 1000°C exhibit little variation in conductivity between 100°C and 700°C. The values increase significantly from 700°C to 900°C. The same trend is observed for T1250, except that there is a moderate increase in conductivity below 600°C and a significant increase above this temperature. At low temperatures there are large differences between the samples, but as the temperature increases, the curves converge, and at maximum temperature the conductivities are almost equal in all samples.

In addition, it is observed that there is no trend in sintering temperature. The sample sintered at the highest temperature exhibit lowest conductivity, whereas T850 shows lower conductivity than T1000.

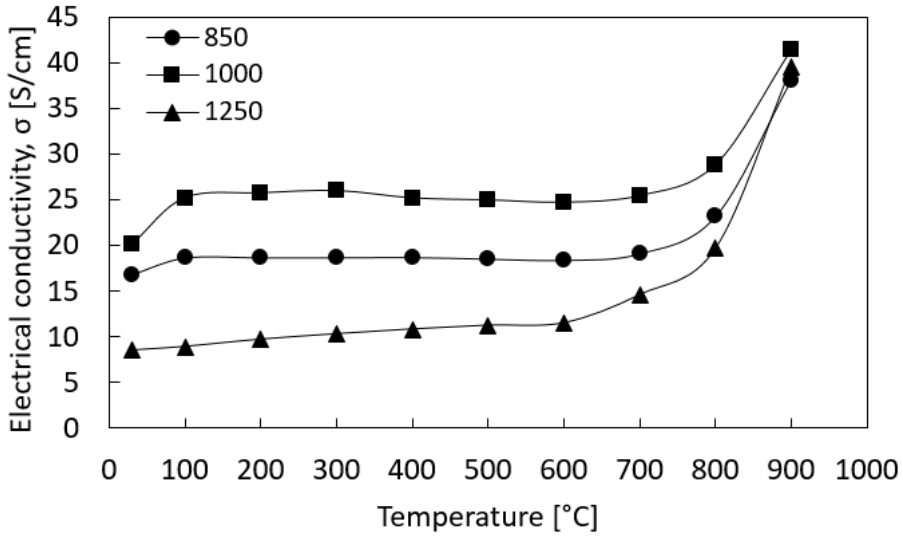

Figure 4.21: Electrical conductivity as a function of temperature, measured in air. Values are obtained upon cooling from 900 °C.

4.5.2 Seebeck coefficient

As for the electrical conductivity, the Seebeck coefficient values are obtained upon cooling from 900°C to room temperature. The values are presented in Fig.4.22. The data obtained from the entire measurements is shown in Appendix I.

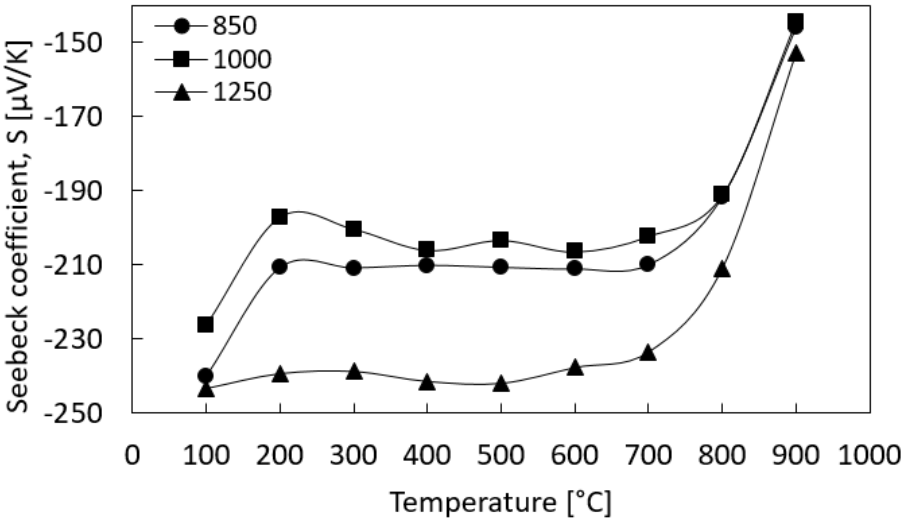

Figure 4.22: Seebeck coefficient values as a function of temperature, measured in air. Values are obtained upon cooling from 900 °C.

The Seebeck coefficients obtained for all three samples are negative. The plot shows the same trend in T850 and T1000; |S| decreases significantly from 100°C to 200°C, remains relatively

constant from 200°C to 700°C, before it greatly decreases. T1250 shows a rather constant |S| up to 600°C, where it starts to decrease. The most significant decrease occurs between 700°C and 900°C.

At low temperatures, excluding T=100°C, T1250 shows significantly higher Seebeck coefficient than the other two samples, which are quite similar in value. As the temperature increases the differences become smaller, and at maximum temperature the values are almost equal in all samples.

4.5.3 Thermal conductivity

The thermal conductivity was measured from 100°C to 900°C, and is presented in Fig.4.23. The plot shows that the thermal conductivity decreases with increasing temperature, a trend observed in all samples. The values obtained for the sample sintered at 1000°C are 1.1 times higher than for the other samples, at all temperatures. The thermal conductivity of T850 and T1250 are almost equal, but the latter has slightly lower values at most temperatures.

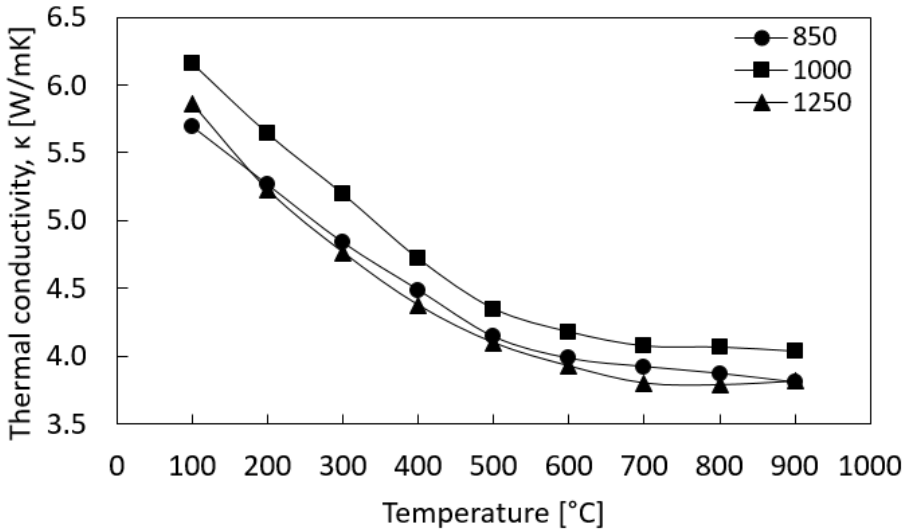

Figure 4.23: Thermal conductivity values as a function of temperature, from laser flash measurements in air.

Electronic and lattice contributions to the thermal conductivity are presented in Fig.4.24. The electronic contribution was calculated using Eq.2.12 with L=2.45·10^{-8} ΩW/K^2[22], making it possible to calculate the lattice contribution as the difference between the total and the electronic thermal conductivity. The curves show that the electronic contribution is low at low

temperatures. It increases significantly at higher temperatures, however, compared to the lattice contribution, the values are low. The lattice thermal conductivity shows exactly the same trend as the total thermal conductivity.

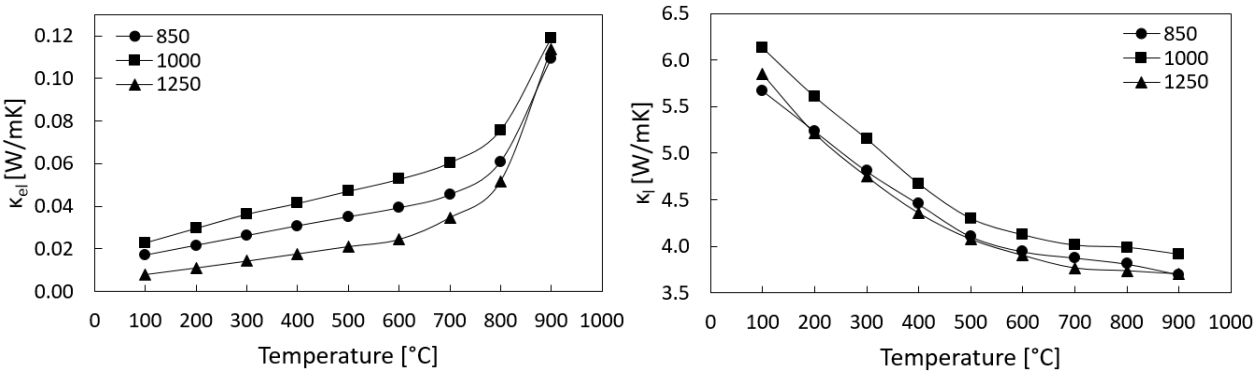

(a) Calculated electronic thermal conductivity, κ_{el}, from Eq.2.12.

(b) Calculated lattice thermal conductivity, κ_l, from Eq.2.11.

Figure 4.24: Calculated electronic and lattice contributions to the total thermal conductivity.

4.5.4 Power factor

Power factor, PF, was calculated from measured Seebeck coefficients and electrical conductivities. PF at different temperatures is presented in Fig.4.25, and shows that the sample sintered at the highest temperature exhibits an increasing PF with increasing temperature. PF of the other two samples decreases from 100°C to 200°C, remains close to constant up to 800°C and then decreases between 800°C and 900°C. This decrease is most significant in T1000, which exhibits highest PF at all temperatures except for at 900°C where it is exceeded by T1250.

4.5.5 Figure of merit

The dimensionless thermoelectric figure of merit, zT, was calculated from the values obtained from the measurements of electrical conductivity, Seebeck coefficient and thermal conductivity. The calculations were performed by using Eq.2.8 in the temperature range 100°C – 900°C. zT as a function of temperature is presented in Fig.4.26, and shows that zT increases greatly with temperature. However, zT of T1000, which has the highest values at all other temperatures, decreases from 800°C to 900°C, resulting in T1250 to reach the highest value, zT=0.028 at 900°C.

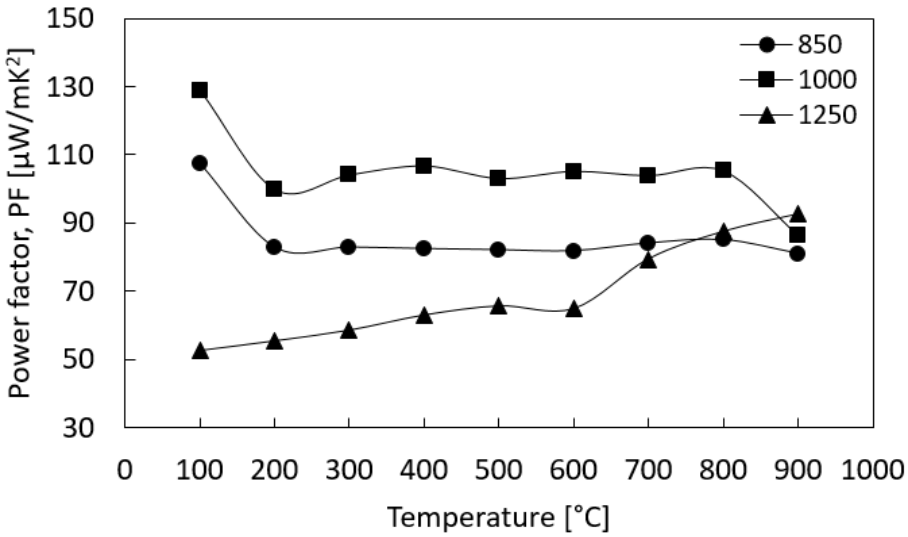

Figure 4.25: Calculated power factor (PF) values as a function of temperature. Based on measured electrical conductivity and Seebeck coefficient values: PF=σS^2.

At temperatures below 700°C this sample has the lowest zT.

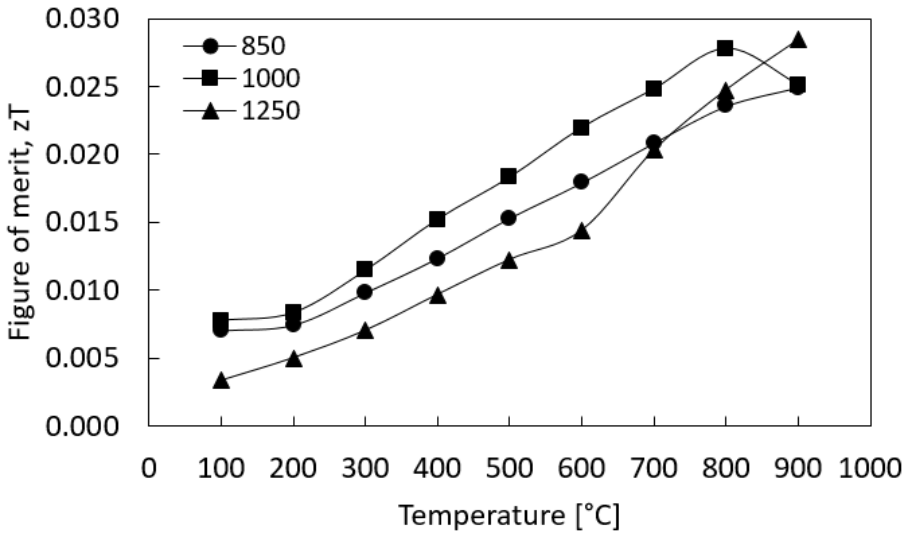

Figure 4.26: Calculated figure of merit values, zT, as a function of temperature. Based on measured electrical conductivity, Seebeck coefficient and thermal conductivity values, Eq.2.8.

5 | Discussion

5.1 Rock-salt structure

Phase composition

When heat treating the powder in reducing atmosphere, a single-phase rock-salt structure was achieved. However, after sintering, which was carried out at higher temperatures than the heat treatment, a secondary calcium tantalum oxide phase, $CaTa_2O_6$, becomes apparent.

Fig.5.1(a) emphasizes the evolution of this phase and the shift in the peaks with increasing sintering temperature. The shift to a higher 2θ indicates a reduction in lattice parameters, as shown in Fig.5.1(b). This shows that as more secondary phase is exsolved, the more the cubic rock-salt lattice contracts, because some Ca^{2+} is removed from the structure to form $CaTa_2O_6$ with Ta^{5+}. As there are no additional peaks in the sample sintered at 850°C, it is assumed that Ta is in solid solution with the rock-salt structure at this temperature, hence no secondary phase.

The formation of $CaTa_2O_6$ could indicate that the Ta-ions do not fit in the cubic rock-salt structure, and hence exsolves as a secondary phase. This is supported by the lattice parameter of the sample sintered at 850°C, where the value is higher than for pure $Ca_{0.5}Mn_{0.5}O$, implying that Ta dissolved in the rock-salt structure expands the lattice. However, the atomic radius of Ta^{5+} is not larger than the atomic radius of Mn^{2+}, as reported in Tab.5.1. Hence, the size is not the reason for exsolution of $CaTa_2O_6$.

Table 5.1: Shannon radii of the ions [42]

Ion	Ionic Radius [nm]
Ca^{2+}	0.1
Mn^{2+}	0.083
Ta^{5+}	0.064

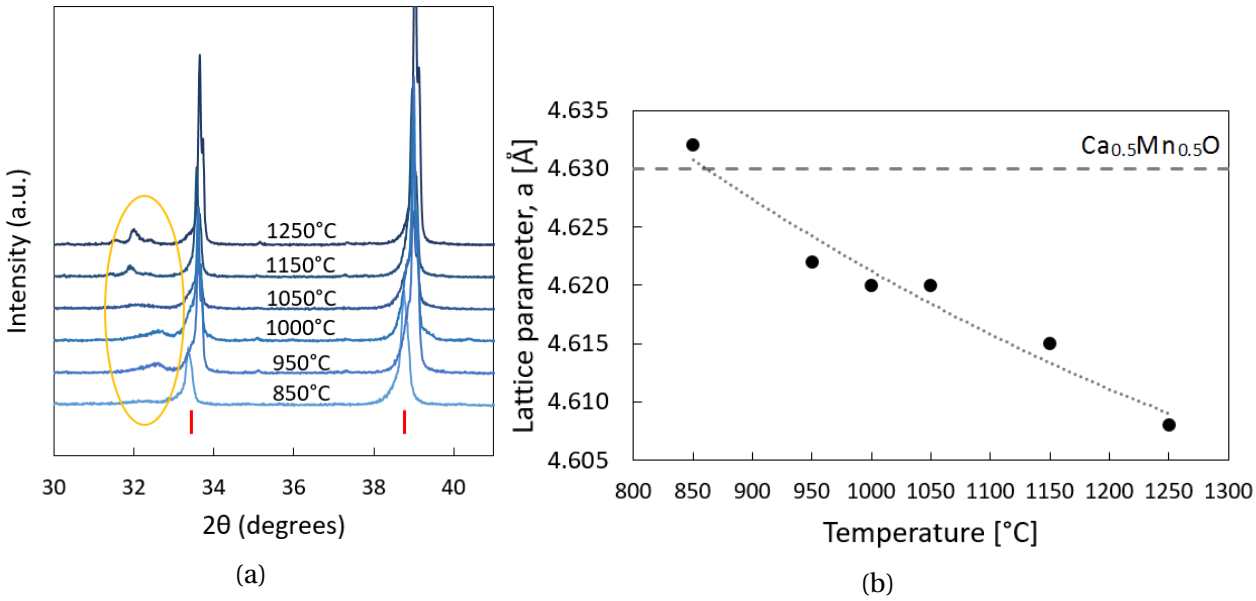

Figure 5.1: (a) Cut out from the diffractogram presented in Fig.4.5, showing evolution of the secondary phase (circled) as the peaks shift. (b) Variation in lattice parameter with sintering temperature for the primary phase. Lattice parameter for pure $Ca_{0.5}Mn_{0.5}O$ is added as horizontal, broken line.[52]

Another explanation for the formation of the secondary phase $CaTa_2O_6$ is that CaO is basic while Ta forms a mildly acidic oxide, hence they form a stable composition. In addition, this is a composition where Ta has oxidation state +5, which is tantalum's most stable oxidation state.

The observations made in the diffractograms are supported by SEM images of etched surfaces. By studying Fig.5.2 an increasing amount of $CaTa_2O_6$ is observed, given the assumption that the small round particles are $CaTa_2O_6$. However, this could not be confirmed by BSE nor EDS as the conduction of the material was too poor to obtain adequate detection signals, even with carbon coating.

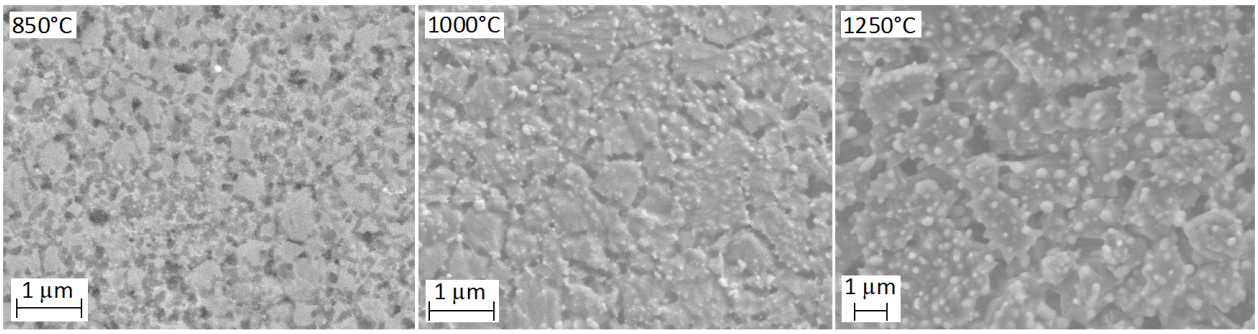

Figure 5.2: SEM images of thermally etched surfaces, to study evolution of $CaTa_2O_6$. The higher the sintering temperature (given in each image), the more white particles.

From these observations it is shown that a secondary phase is present at most sintering temperatures, but it is necessary to conduct a detailed TEM (transmission electron microscopy) investigation combined with EDS analysis to further explain the formation of this phase.

Density

The density measurements show that the as-sintered samples are highly dense, close to 100%, with no closed porosity. However, some open porosity is measured. According to sintering theory, there should be no open pores at this high density[23], hence this result is most likely due to measurement errors. When measuring the weight of wet pellet, excess liquid should be removed by damped paper. The used paper was probably wet and not damped, leading to a liquid film on top of the sample. This results in an incorrect weight, which in turn leads to a too high measured open porosity (Eq.C.3). The apparent open porosity might also be due to microcracks. Regardless of measurement errors and cracks, it is valid to conclude that the samples are highly dense, which is confirmed by SEM images of fracture surfaces.

The behaviour of the curves obtained from the SPS, Fig.4.4, corresponds well with the measured high density. The curves, showing change in sample thickness as a function of temperature, show no further densification above 880°C–930°C (depending on the sample), indicating that highly dense samples are achieved. This is not observed in the curve of the sample sintered at a maximum temperature of 850°C, indicating incomplete densification. However, as the density is in fact close to 98% after sintering, it is likely that the same trend would be observed if the temperature was increased with 20°C–30°C or the dwell time increased.

Grain size

According to SEM images, the average grain size of sintered samples increase with temperature. As the material is highly dense at all sintering temperatures, the densification process is almost finished and grain growth dominates. This is also shown by the curves obtained from SPS, Fig.4.4, where most curves flat out between 880°C and 930°C, indicating that higher temperatures do not result in further densification but rather further grain growth. As grain growth should be opposed to maintain the nanostructure, sintering temperatures between 850°C and 950°C would be preferable. In addition, sintering time shorter than five minutes should be in-

vestigated in order to reduce the grain size. Lower sintering temperatures could also be considered. However, by studying the curve showing grain size as a function of sintering temperature, Fig.4.8, it is observed that the slope between 850°C and 950°C is moderate. Hence, if this trend continues at lower temperatures, a decrease to for example 800°C would probably not reduce the grain size significantly.

5.2 Oxidation of rock-salt structure

After sintering, the material was annealed in oxidizing atmosphere to obtain the two initial phases: CMO with perovskite structure and marokite with spinel structure. Hence, different analyses were conducted in order to understand the oxidation process and to determine annealing program.

HTXRD, DIL curves and TG analysis show that corresponding compositions start to oxidize at different temperatures. Samples in HTXRD and TG start to oxidize at lower temperature (respectively 500°C–560°C and 400°C) than the samples in DIL (700°C). This is because the samples are in powder form, which gives larger surface area that is exposed to oxygen and shorter diffusion path. This results in earlier oxidation than in DIL, where the samples were sintered pellets.

The result from HTXRD shows that the main CMO-phase and the secondary phase are not formed simultaneously during the oxidation, but the perovskite is formed before the marokite is exsolved. The diffractograms show that the formation of the secondary marokite phase starts between 800°C and 900°C, which agrees well with the phase diagram in Fig.2.7. The phase diagram shows that manganese rich samples go through a 2:3-phase, $Ca_2Mn_3O_8$, at lower temperatures before transforming to marokite. This phase is not observed in HTXRD, most likely due to too short time. At lower temperatures oxygen deficient perovskite is observed.

By studying the DIL curves it is seen a moderate expansion above 820°C, even during the dwell time at 1300°C. This is probably not caused by further oxidation but cation diffusion that occurs to form the spinel phase from the Mn-supersaturated perovskite. This is supported by the results from the HTXRD that show that the rock-salt structure is completely transformed at 800°C, and above this temperature formation of marokite is the only change in the structure. In addition, XRD of the samples used in DIL showed no traces of remaining rock-salt, hence

incomplete oxidation at 1300°C is unlikely. Expansion caused by formation of secondary phase can be explained with the fact that the molar volume of marokite is much larger than the molar volume of the perovskite. Values are given in Appendix D.

The TG curves show that when the temperature is increased above 400°C, $Ca_{0.5}Mn_{0.5}O$ is being oxidized to $CaMnO_3$ through a topotactic reaction mechanism[21], hence the rapid mass increase. The result indicates that $Ca_{0.5}Mn_{0.5}O$ is completely converted to $CaMnO_3$ between 730°C and 850°C as the mass is stabilized. However, there is a moderate increase probably caused by the formation of the secondary phase with four oxygen atoms, $CaMn_2O_4$. This behavior of rapid increase followed by a slower rate is similar as in DIL measurements. When the temperature is further increased, the structure releases oxygen according to the reaction Eq.5.1, and reaches equilibrium at maximum temperature. Upon cooling the reaction is reversed and the structure recovers from the oxygen loss completely at 730°C. This supports the suggestion that the mass change between 730°C and 850°C mainly is due to formation of marokite.

Similar behavior, with mass loss upon heating and mass increase upon cooling, was observed in $CaMn_{1-x}Nb_xO_{3-\delta}$ described by Bocher *et al.*[22] and in $CaMn_{1-x}W_xO_{3-\delta}$ showed by Thiel *et al.*[55].

$$CaMnO_3 \rightarrow CaMnO_{3-\delta} + \frac{\delta}{2}O_2 \tag{5.1}$$

HTXRD, DIL and TGA show that complete transformation from rock-salt to perovskite occurs around 800°C, and the secondary phase is formed between 800°C and 900°C. Based on these results, a heat treatment program to anneal the samples in air was worked out, and different approaches were investigated to avoid cracking. Due to differences in the unit cell volumes and molar volumes between the reduced phase and the oxidized phases (Appendix.D), the material will chemically expand. Because of the expansion, it is easiest to oxidize materials with low density, as high porosity prevents crack propagation. Porosity also gives free space, making it possible for the structure to expand without causing internal strains or stresses. This is not the case in high density materials, like the resulting samples in this project, hence sufficiently high temperature during oxidation is needed to induce creep in the material. In addition, sufficiently high creep rate is required to provide high enough flexibility within the material for cations to move around freely and prevent crack formation. This is because the material is calcium de-

ficient, and cation rearrangement is needed to form the secondary phase, marokite. This will cause greater stresses in the material than the transformation from rock-salt structure to perovskite, which follows the topotactic reaction mechanism with no cation rearrangement[44].

However, high temperature during annealing can additionally result in grain growth. Hence, there is a trade-off to account for when determining the maximum temperature.

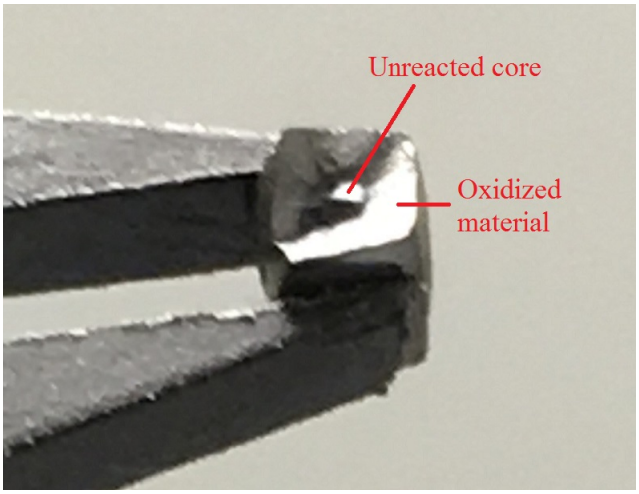

Figure 5.3: Image taken with a camera, showing incomplete oxidation, with a core of rock-salt surrounded by oxidized material. Fracture occurred around the unreacted core. Annealing dwell time=3h.

Another important parameter to consider is the holding time at maximum temperature. Enough time to ensure complete oxidation of the material is needed, and the higher the density, the more time is required. Required time is also dependant on the dimensions of the sample, as they will effect the oxygen diffusion length. As the transformation to form perovskite starts at the surface and continues inwards, an incomplete oxidation process will result in a core of rock-salt structured material surrounded by oxidized material. The reduced material has a higher TEC, hence it will have a higher shrinking rate than the oxidized material upon cooling, creating "shrinking core" presented in Section 2.3.3. As illustrated in Fig.5.3, this causes fracture in the interface between the two structures. This is the reason the 1250°C-sample cracked when oxidized for three hours, but not when kept for six hours. This is supported by XRD-results, Fig.4.13, showing remains of the rock-salt in the three hours-sample.

5.3 Phase relations and microstructure of CMTO annealed in air

Density and porosity

Like the as-received samples from SPS, the annealed samples are highly dense, with a relative density of approximately 95%. In some samples, open porosity is reported, which according to classic sintering theory should not be present at density higher than 92%[23]. As it was challenging to produce crack-free samples, it is possible that these measured open pores are due to microcracks. It could also be caused by measurements errors, as discussed in section 5.1.

The theoretical density of CMTO is calculated based on 20 vol% marokite, without including $CaTa_2O_6$. This is because the Ta-rich phase is not apparent in XRD-results, hence it is not possible to calculate the quantitative amount of this phase. Due to this, the relative density might be somewhat incorrect. However, as the amount is low compared to the amount of CMO and marokite, seen from the SEM images, this will most likely have little affect on the total density. In addition, Ta is taken into account when using the theoretical density of stoichiometric CMTO instead of undoped CMO. Some of the annealed samples do not have exactly 20 vol% marokite, but as the theoretical density of marokite and stoichiometric CMTO are almost equal, 4.68 g/cm^3 vs. 4.70 g/cm^3 (App.D), this will have minimal effect.

As all samples are dense after sintering and after annealing, it is shown that a sintering temperature of 850°C is sufficiently high to achieve a dense material by using spark plasma sintering. Sintering the same material with the same composition with conventional pressure-less sintering requires 1050°C to obtain a density of 92% and 1150°C to obtain a density over 97% according to a study[25]. This shows that by using SPS it is possible to lower the sintering temperature by approximately 300°C, which agrees well with previous studies[46].

Grain size

The grain size increase with increasing temperature in the as-sintered samples, as well as in the annealed samples. However, the grain growth show different rate. By studying Fig.5.4 it is observed that the rock-salt structure experiences extensive grain growth between 1000°C and

1250°C, while the annealed material shows moderate growth. This is mainly due to the formation of secondary phase in the oxidized material, as secondary phases along grain boundaries restrict further grain growth. From the SEM images taken of the oxidized material it is seen that the secondary phase surrounds the grains of CMO, limiting the growth. A secondary phase is also observed in the reduced material, but the amount is probably too small to affect the grain growth.

From the plot in Fig.5.4 it is also observed that the grain size in the oxidized material is larger than the grain size in the as-sintered samples at some temperatures and smaller at others. When rock-salt is oxidized, the rock-salt grains are transformed to grains of both CMO and marokite, resulting in smaller grains in the oxidized material. However, samples sintered at lower temperatures than the annealing temperature of 1100°C experience extensive grain growth, especially in the CMO-phase, as seen from Fig.5.4(a).

Considering the grain sizes after annealing, most grains are not in the nanorange, which was desired. Nanosized grains are beneficial as they lower the thermal conductivity of the material, and limiting grain growth was one of the main reasons SPS was utilized instead of conventional pressure-less sintering. However, the grains are larger than the sizes obtained in the study by Ledezma[25], where the same material was investigated but with the use of conventional sintering. In that study, a sintering temperature of 1150°C resulted in 97% density and an average grain size of 800 nm.

As discussed, SPS resulted in relatively small grains at the lowest sintering temperatures, however, in these samples significant grain growth occurred during annealing. Hence, to obtain smaller grains annealing programs should be optimized for each sample. However, lowering the annealing temperature will create challenges regarding cracking during oxidation, and the best compromise needs to be pursued.

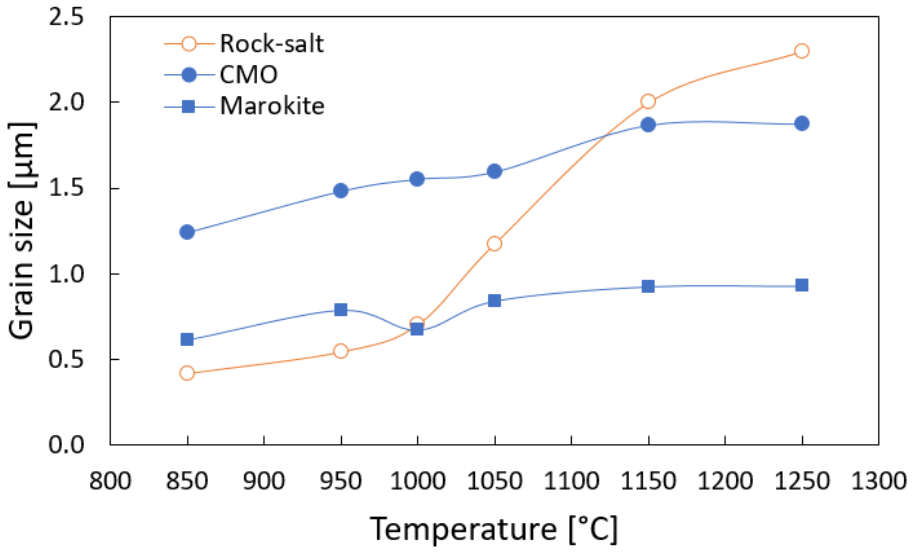

(a) Average grain size estimated from SEM images as a function of sintering temperature. Comparison of grain sizes in as-sintered samples and annealed samples.

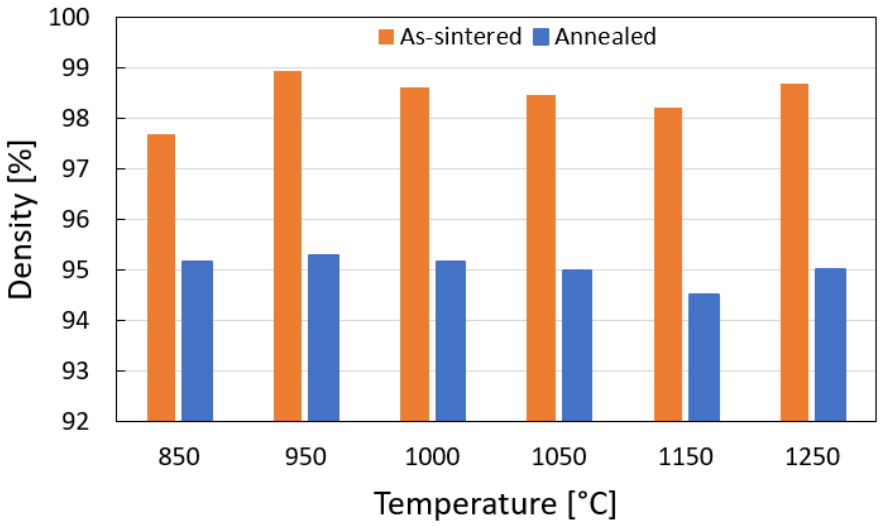

(b) Relative density as a function of sintering temperature. Orange bars are as-sintered samples and blue bars represent the density of the material after annealing in air.

Figure 5.4: Microstructural comparison of as-sintered material (rock-salt) and annealed material (CMO+marokite).

5.3.1 Secondary phases

$CaMn_2O_4$

An important motivation for investigating an A-site-deficient compound such as $Ca_{0.931}Mn_{0.98}Ta_{0.02}O_{3-\delta}$ was the enhanced possibility to promote exsolution of secondary phases able to scatter phonons and accordingly reduce thermal conductivity. Results from SEM images and XRD analyses clearly show that a orthorombic spinel phase with composition $CaMn_2O_4$ is formed. This marokite phase is most evident in BSE images, Fig.4.18, which show that smaller marokite grains surround larger CMO grains. This indicates that the nucleation and growth of the secondary phase takes place at grain boundaries. However, due to extensive growth it is difficult to state the origin of the nucleation.

The as-received CMTO powder was synthesized to contain 10 vol% secondary phase, while results of the sintered and annealed material show around 20 vol% marokite. One potential reason for this difference is related to uncertainties in the information from the supplier of the precursor powder. The powder was spray pyrolysed, where the atmosphere might be slightly reducing. It is then calcined in air, oxidizing the potentially reduced powder. However, there is a possibility that the composition had not reached equilibrium during the calcination time, causing some Mn-supersaturated perovskite to still be present. This will result in further formation of marokite when heating the material in air, as the formation of $CaMn_2O_4$ is a result of excessive amounts of Mn in CMO.

Another explanation for the increased amount of marokite, is related to the formation of $CaTa_2O_6$. $CaTa_2O_6$ is formed in the main phase of CMO and not in the marokite, which will be shown in the next section. Hence, Ca^{2+} needed to form $CaTa_2O_6$ is provided from the CMO perovskite, leaving a Mn-supersaturated structure which causes exsolution of more marokite.

Tab.4.6 presents relative amounts of marokite based on XRD results. Although the values of around 20 vol% seem too low when studying the SEM images of polished surfaces, the trend corresponds well. The calculations result in 23 vol% marokite in the sample sintered at 850°C, 19 vol% in the sample sintered at 1000°C and 25 vol% in the sample sintered at 1250°C, and by studying Fig.5.5 it can be observed more marokite, light grey areas, in the 850°C- and 1250°C-sample than in the 1000°C-sample.

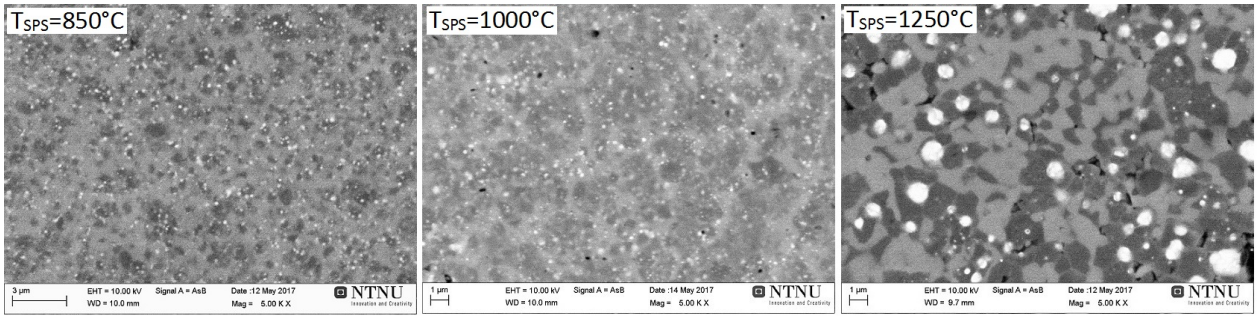

Figure 5.5: BSE images of polished surfaces, to study amount of marokite. Sintering temperature is given in each image. Dark gray=CMO, light grey=$CaMn_2O_4$, white=$CaTa_2O_6$. Magnification = 5.00 K X

$CaTa_2O_6$

In SEM images of polished surfaces a third phase becomes evident. EDS scans confirm that these white areas consist of O, Ca, Mn and are rich in tantalum. As presented in Section 4.2.3, small white particles were also observed in the reduced samples, most evident at higher temperatures. XRD-analysis showed that those particles are $CaTa_2O_6$. This is a very stable composition, with Ta with its stable oxidation number +5 and Ca that does not change its oxidation state during oxidation. Hence, it is reasonable to deduce that the Ta-rich phase observed in the oxidized material is $CaTa_2O_6$.

However, this phase is not confirmed by XRD. By studying the diffractograms in Fig.4.14, no Ta is detected in any of the samples. Fig.5.6 shows the diffractogram corresponding to the sample sintered at 1250°C, which is the sample with highest amount of the Ta-rich phase according to SEM images, both in reduced and oxidized phase. Yellow marks illustrate where the phase should appear, showing that there is no clear trace of $CaTa_2O_6$.

Despite this XRD-result, the third phase is most likely to be $CaTa_2O_6$. EDS point analyses show an increasing atomic percentage of Ta in these areas. However, the analyses also detect Mn in the composition, and the reported amounts of Ta and Ca (Tab.4.7) do not correspond with the stoichiometry. That is probably because a large amount of the background is additionally detected, as the white areas are small. The phase is also supported by EDS line scans performed on several samples.

Further, EDS analyses show that there are no or negligible amounts of Ta in marokite, but small amounts in the CMO phase. In addition, based on SEM images, $CaTa_2O_6$ is formed in the

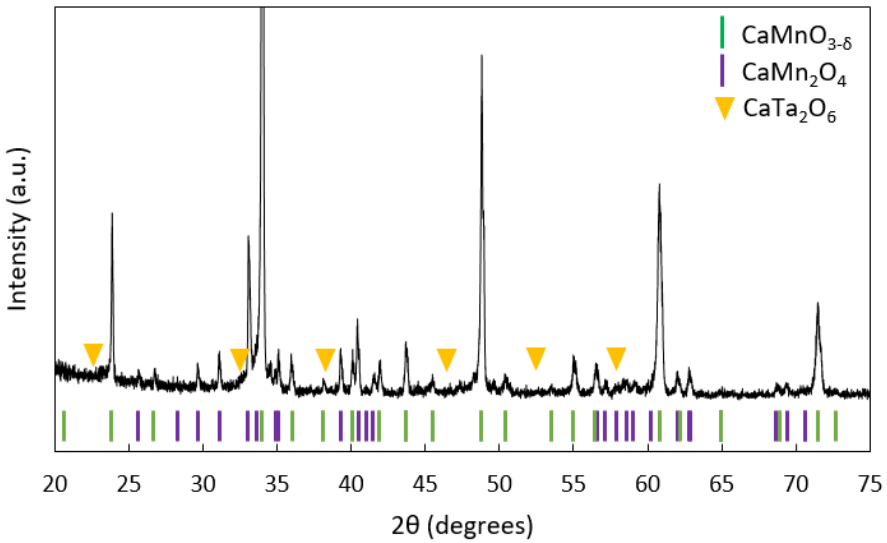

Figure 5.6: XRD result of sample sintered at 1250°C, showing presence of CMO and marokite, but no Ta-rich phase. Yellow marks show where the peaks of $CaTa_2O_6$ should be present.

CMO perovskite, as emphasized in Fig.5.7, showing cut-outs from SEM images of the sample sintered at 1250°C. These results show that Ta is insoluble in marokite and somewhat soluble in the perovskite, however, not enough to completely dissolve Ta. Hence, exsolution of $CaTa_2O_6$. Due to the formation of this phase, the reaction presented in Eq.2.20 is incorrect as it assumes that all Ta is dissolved in CMO. However, to develop an equation with correct stoichiometry including $CaTa_2O_6$ is difficult as the amount of Ca^{2+} removed from CMO to form $CaTa_2O_6$ is unkown.

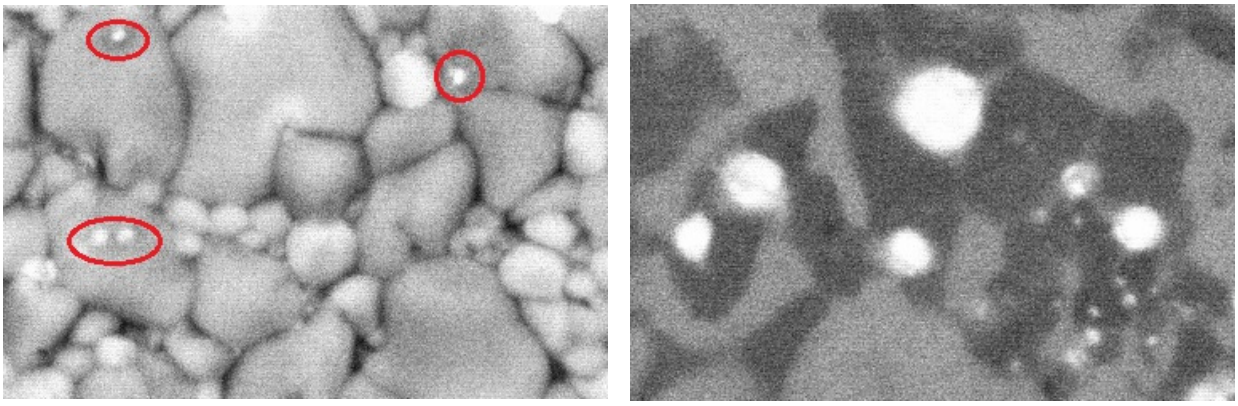

(a) Etched surface. $CaTa_2O_6$ in red circles.

(b) Polished surface. White areas are $CaTa_2O_6$.

Figure 5.7: Cut-out from SEM images showing that the $CaTa_2O_6$-phase is formed in the CMO perovskite. In polished surface: Dark gray=CMO, light grey=$CaMn_2O_4$, white=$CaTa_2O_6$.

SEM images, Fig.4.18, also show that $CaTa_2O_6$ is homogeneous distributed at lower sintering temperature, but the higher the temperature the more concentrated the white areas appear. This development might be connected to the evolution of $CaTa_2O_6$ in the reduced phase, as there were exsolved more of this phase as the sintering temperature was increased. At 850°C, Ta is in solid solution with the main phase and nucleation does not start until the material is heated during annealing. At higher temperatures, the nucleation has started and the higher the sintering temperature the more growth occurs, both during the sintering and the annealing. This can explain why the $CaTa_2O_6$–grains are small and evenly distributed in the annealed sample sintered at 850°C, while they are larger and inhomogeneously distributed in the sample sintered at 1250°C. However, according to XRD-results shown in Fig.4.14, there is no shift in the lattice parameters in the CMO-phase, implying an equal total amount of $CaTa_2O_6$ in all samples.

5.4 The conflict of assessment of grain size by Debye-Scherrer (XRD) and SEM

Both as-sintered samples and annealed samples have grains that consist of smaller crystallites, as there are large differences between crystallite sizes calculated from XRD-results with Debye-Scherrer method and grain sizes estimated from SEM images. Values are presented in Fig.4.8, Tab.4.3, Fig.4.16 and Tab.4.5. Figures where the results are plotted together are shown in Appendix J.

One potential reason for the large differences is related to the Debye Scherrer method. The Scherrer equation only addresses peak broadening that is entirely caused by size effects and does not include factors such as strain[56]. Strain in the material will cause peak broadening in the XRD-pattern and result in an apparent crystallite sizes smaller than the actual size. However, as $Ca_{0.5}Mn_{0.5}O$ is isotropic with a cubic structure, this is less likely in the reduced samples. Oxidized samples obtain cubic structure above 913°C[19] and strain in the material is limited, but at lower temperatures the structure is tetragonal or orthorombic and the material anisotropic. However, the peaks in the XRD-patterns are symmetric and do not disclose any strain, hence, strain is not the main reason for the apparent small crystallites in either reduced or oxidized samples.

It can also be a microstructural reason for the small crystallite sizes. A lamellar microstructure is observed in several as-sintered samples, most evident in Fig.4.6 (f). It is possible that these lamellae reflect the crystallite size, as the sizes correspond well. However, to confirm this deduction, detailed TEM analysis is necessary.

5.5 Thermoelectric properties

5.5.1 Electrical conductivity

Study of electrical conductivity has shown that it decreases with increasing amount of secondary phase. The sample sintered at 1250°C, T1250, has the highest content of secondary phase, while T850 has a higher amount than T1000, which is reflected in the electrical conductivity trend. The secondary phase is confirmed to be marokite, $CaMn_2O_4$, which is highly insulating[37]. Consequently, a significant amount of marokite will reduces the overall electrical conductivity. This effect is most pronounced at low temperatures and it gradually decreases as the temperature increases.

Grain size can also affect the electrical conductivity. Small grains might lower the conductivity as they create more grain boundaries which can scatter conduction electrons and inhibit the free flow. However, as the results show that the sample with the largest grains (1.9 μm vs. 1.6μm and 1.2μm) is the poorest conductor, it can be concluded that the effect of secondary phase has a larger impact on the conductivity than the grain size.

The plot in Fig.4.21 shows little variation in conductivity below 700°C, from where it increases significantly. This evident increase occurs because the material becomes oxygen deficient above around 700°C. As explained in Section 2.3.3, the oxygen stoichiometry affects the electrical conductivity in perovskites, as an increase in the oxygen vacancy concentration, δ, causes a rise in the charge carrier concentration, Eq.2.15. The additional charge is compensated by changing the ratio $\frac{Mn^{3+}}{Mn^{4+}}$. Since the conduction mechanism in $CaMnO_{3-\delta}$ is governed by small polaron hopping, it is proportional to $\frac{Mn^{3+}}{Mn^{4+}}$. Hence, an increase in δ leads to a strong increase in electrical conductivity.[16] Due to this effect, thermally activated polaron hopping is the dominating conduction mechanism at higher temperatures. In addition, the higher the temperature,

the more cubic the CMO structure becomes[19], which enhances the mobility and increases the conductivity.

Based on previous studies, the electrical conductivity does not behave as anticipated at lower temperatures. In a study by Ledezma[25], the same CMTO precursor powder as used in this work was sintered with conventional pressure-less sintering. Two routs were investigated; one where sintering was conducted only in oxidizing atmosphere (denoted "O"), and one where the samples were sintered via the reduced rock-salt phase (denoted "R/O"). Unlike the procedure in this work, the reduction and annealing were performed in one step in the furnace. This sintering method resulted in an electrical conductivity with metallic behaviour below 800°C and polaron hopping between 800°C and 900°C. By comparing those results to the results in this work, Fig.5.8(a), it can be concluded that the material has lost the metallic behavior. Instead, the material exhibit similar trend as observed in undoped CMO, presented in Fig.5.8(b) and reported in multiple publications[16, 27, 20]. Below 700°C, the values of CMTO are higher than CMO as a result of the substitution of Ta^{5+}, which leads to generation of Mn^{3+} in the Mn^{4+} matrix[29]. The metallic-type conduction in substituted CMO is also reported by others[29, 37, 57].

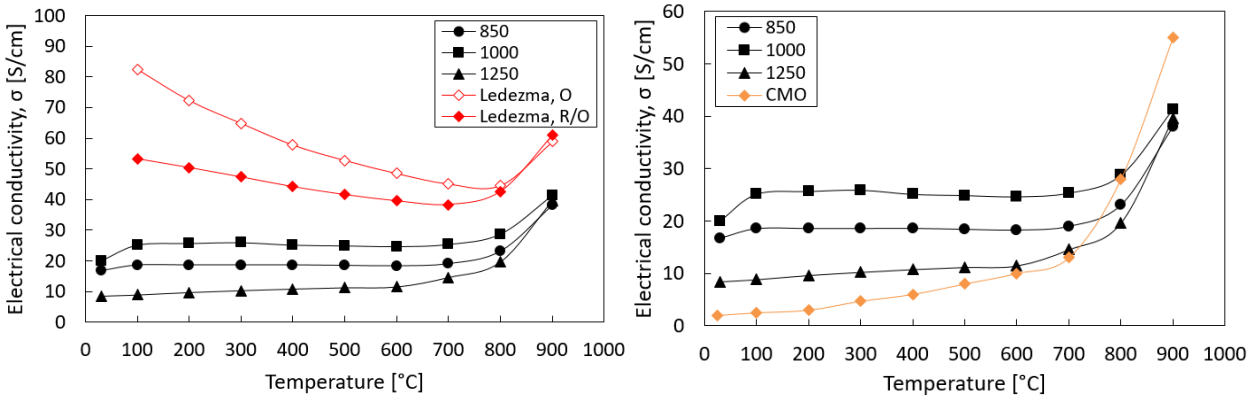

(a) Results compared with study by Ledezma (red), where the samples are 97% dense[25].

(b) Results compared with undoped CMO with density 90% (orange)[37].

Figure 5.8: Electrical conductivity results compared with other studies. Samples are 95% dense.

The main reason for the loss of metallic conduction and the significant decrease in overall conductivity, Fig.5.8(a), is the formation of secondary phase. The samples from the study by Ledezma consisted of approximately 10 vol% marokite, while in the investigated samples in this

study the amount of marokite was at least 20 vol%. In addition, the relative density is 2% lower in this work, which might have lowered the value to some extent.

5.5.2 Seebeck coefficient

The negative values for the Seebeck coefficient confirm that CMTO is an n-type semiconductor. The measured values, presented in Fig.4.22, decrease in absolute value with increasing temperature, which can be connected to the material's semiconductor behaviour. Further, values increase with increasing amount of secondary phase. This trend is the opposite of the trend observed for the electrical conductivity, which is expected as the S and σ have inverse dependency on the charge carrier concentration[7].

Further, it is observed that at low temperatures, the secondary phase has the strongest influence on $\frac{Mn^{3+}}{Mn^{4+}}$ ratio, resulting in the largest difference between the investigated samples.

The values of T850 and T1000 correspond well with data for CMTO reported by Thiel *et al.* [29] and CMTO by Ledezma[25]. T1250 exhibits higher Seebeck coefficient, as a results of the secondary phase. This increase is positive as the S should be as high as possible in order to obtain good conversion of heat to electricity. The values are, however, lower than in stoichiometric pristine CMO, which has values between -260μVK^{-1} and -480μVK^{-1}[27]. This is due to the electron doping.

5.5.3 Thermal conductivity

By studying the two contributions to the total thermal conductivity, it is seen from the values presented in Fig.4.24 that the electronic contribution (κ_{el}) is significantly smaller than the lattice contribution (κ_l), and accounts for less than 3% of the total thermal conductivity. This is a result of the low electrical conductivity. A dominating κ_l indicates that CMTO is a semiconductor, as seen in Fig.2.3, and promising for thermoelectric applications as the total κ can be lowered without further decreasing the electrical conduction.

From the measured data, Fig.4.23, it is seen that the thermal conductivity decreases with increasing temperature. Due to the low κ_{el}, this trend is due to the reduction in the lattice phonon conduction, κ_l. κ_l decreases because the mean free path of phonons is reduced at high temper-

atures (Eq.2.13), and the Umklapp-type phonon-phonon scattering starts to dominate, instead of scattering due to mass difference or grain boundaries[12]. This result corresponds well with literature on TE materials in general[11], as well as for electron doped $CaMnO_3$[22].

According to the theory, the smaller the grains in the material, the lower the thermal conductivity [32], as grain boundaries limit phonon propagation. The results obtained in this work do not not show this trend. This is because the average grain sizes in the samples are in micrometer scale, while the effect of grain boundaries on phonon scattering is most significant when the grains are of nanosize, especially when their size becomes comparable to the phonon mean free path.[31, 30]. Besides, Kuomoto *et al.*[32] and Loland *et al.*[33] state that the effect on thermal conductivity is most significant when reducing the grain size below 100 nm, and as the grain sizes obtained is this work are between 600 nm and 1.9 μm, the grain size effect is probably less significant. Hence, it is difficult to predict how significantly smaller grains would have affected the thermal conductivity.

This indicates that there is another factor that affects the thermal conductivity, which is the secondary phase, marokite. The trend of the thermal conductivity corresponds with the trend in amount of marokite. As marokite exhibits low electrical conductivity, the electronic thermal conductivity will be lowest in the sample with the most marokite. This is in agreement with the results presented in Fig.4.24(a), however, as discussed, this contribution is very small and therefore has little influence on the total thermal conductivity. This is supported by Fig.4.24(b), showing the same trend in the lattice contribution as in the total thermal conductivity. Regardless of this, marokite reduces the thermal conductivity because the total thermal conductivity is lower in this material, Fig.2.13(b), compared to stoichiometric CMO and CMTO.[37] Beside, secondary phases represent additional interfaces that can scatter phonons.

Furthermore, if more marokite is a result of more $CaTa_2O_6$, as discussed, this could also contribute to the trend. SEM and EDS has shown that the $CaTa_2O_6$-phase is distributed inside the CMO-phase, as emphasized in Fig.5.7. This makes the structure less homogeneous, and as $CaTa_2O_6$ has a cubic structure and 50% higher density than CMO (Appendix. D), this phase might work as phonon scattering centers. As a result, T1250 with the highest amount of $CaTa_2O_6$ (according to SEM), will exhibit lowest thermal conductivity.

By comparing the results with the study by Ledezma[25], Fig.5.9, it is observed that the ther-

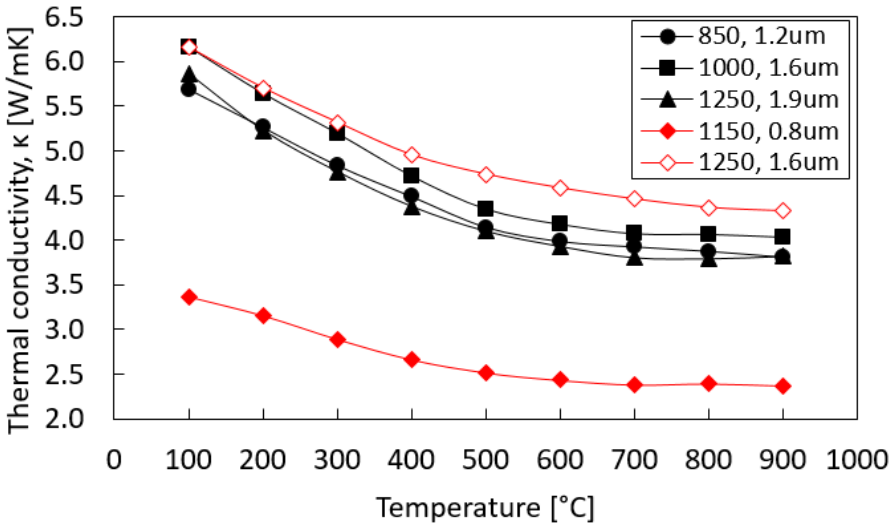

Figure 5.9: Thermal conductivity results compared with study by Ledezma[25] (red curves). Samples from that study have density of 97%, while samples from this work are 95% dense. Sintering temperatures and grain size are given in the figure.

mal conductivity values correspond with the values of the conventional sintered sample with grain size 1.6 μm, however somewhat lower due to a 2% lower relative density and the effect of secondary phase. A secondary phase (10 vol%) was introduced in the samples sintered with conventional sintering as well, and significantly smaller grains were obtained in the sample sintered at 1150°C through the reduced phase. This combination resulted in thermal conductivity reduced by ≈46% compared to the best result from this study.

5.5.4 Power factor and Figure of merit

Calculated power factor, PF, is presented in Fig.4.25, and indicates that secondary phase has a negative effect on PF at low temperatures. At higher temperatures, above 700°C the effect on charge carrier concentration becomes less significant, as shown for σ and S. Due to this, PF of T1250 exceeds T1000 and T850 at the highest temperature.

Calculated figure of merit (zT), presented in Fig.4.26, shows that T1250 provides the highest value with zT = 0.028 at 900°C. As seen from Fig.2.5 and Fig.2.9, this value is much lower than zT of conventional TE materials and zT of doped $CaMnO_3$. In addition, zT is reduced by a factor of 4.3 compared to the highest value (zT=0.12) achieved in the study by Ledezma, where the same composition was investigated[25]. This is due the significantly lower electrical conductivity and

the high thermal conductivity. Besides, the sample from Ledezma's study with κ-values in the same area as the values obtained in this study (Fig.5.9), showed a maximum zT over twice as high as 0.028, due to significantly higher σ (Fig.5.8(a)). This illustrates how important is it to obtain a material with high electrical conductivity.

In applications at lower temperatures, there are well-developed metal-based TE materials with higher efficiency than oxides. However, between 500°C and 900°C many of these materials are unstable in air, and melting and oxidation are known problems[1]. Therefore, in case of TE oxides, it is most important to optimize zT in this high-temperature range. By focusing on the trend between 500°C and 800°C in Fig.4.26, the thermoelectric results show that the sample with the highest σ-values exhibits highest zT. Hence, it is again shown that it is important to obtain high electrical conductivity.

In addition to avoid reduction in electrical conductivity, the thermal conductivity should be reduced in order to increase the figure of merit. In theory, based on Eq.2.14, zT can be enhanced when $\kappa_l/\kappa_{el} << 1$. By studying Fig.4.24 it is clear that the ratio is much larger than 1, as $\kappa_l >> \kappa_{el}$. Hence, the criterion is not fulfilled and a significant reduction in the lattice contribution is necessary. To achieve a material with finer grain structure, an optimal program for spark plasma sintering should be further investigated, e.g. effect of sintering time. An annealing program, optimized for each sample based on sintering temperature, should in addition be carried out as high annealing temperature induces significant grain growth.

5.6 Further work

In further work, the effect of using spark plasma sintering should be investigated. Dwell time, heating- and cooling rate, and pressure, as well as maximum temperature, should be varied in order to optimize the SPS program. The goal should be to obtain dense materials at as low temperature and short time as possible, as this will limit the grain growth and thus contribute to the reduction of the thermal conductivity.

In this study it has been shown that a sintering temperature of 850°C is sufficient to achieve highly dense samples of substituted $CaMnO_3$. At this temperature grains in the nanosize scale are obtained before annealing, hence this sample is a possible starting point for enhancing zT.

To achieve this, the microstructure of the material should be changed as to obtain smaller grains with more grain boundaries after annealing. In this investigation, an annealing temperature of 1100°C was applied and a dwell time of 6 hours, which resulted in the grain size of CMO to increase by a factor of 3. Hence, a lower temperature and possibly shorter time should be investigated. However, by lowering the temperature, the risk of cracking increases as less creep will be induced in the material. Too short time will result in incomplete oxidation. In applications where lower density is acceptable, the annealing process might be less challenging, as it is easier to oxidize materials with high porosity. In addition, spark plasma sintering of CMTO in its oxidized phase should be investigated, as this eliminates the challenges related to annealing the samples after sintering.

Introduction of secondary phase is beneficial to some extent, as it causes interfaces to scatter phonons. However, from this study it is seen that an amount of marokite over 20 vol% reduces the electrical conductivity significantly. The microstructure should therefore be altered to obtain enough marokite to lower the thermal conductivity, but at the same time be restricted as it has a negative impact on the electrical conductivity. As the increase in marokite is partly due to the formation of $CaTa_2O_6$ in the reduced material, this phase should be further investigated, both in terms of how it affects the end-result and how it can be avoided. TEM and EDS are possible analysis techniques.

Regarding reduction of grain size, simulations could be performed to predict the optimal grain size to achieve the theoretical minimum of thermal conductivity, beneficial for enhancing zT. Such calculations were conducted by Wang *et al.*[30], studying $SrTiO_3$.

6 | Conclusion

Nanosized ceramic powder with composition $Ca_{0.931}Mn_{0.98}Ta_{0.02}O_{3-\delta}$ (CMTO) was heat treated and reduced to a single-phase rock-salt structure, which then was spark plasma sintered (SPS), followed by annealing in air. Structural and thermoelectric (TE) properties of the material were investigated in order to determine correlations between material's microstructure, composition and TE properties. The following conclusions were made:

- Sintering temperature of 850°C was sufficiently high to produce dense samples (≈98%) in SPS with pressure of 50 MPa and dwell time 5 minutes.
- Nanosized grains were obtained in SPS at sintering temperatures below 1000°C. However, when annealing these samples in air, significant grain growth occurred. Hence, the annealing temperature of 1100°C was too high to preserve the nanostructure.
- Annealing in air at 1100°C completely oxidized the rock-salt structure to perovskite $CaMnO_3$, and resulted in exsolution of the secondary phase marokite ($CaMn_2O_4$). Additionally, a third phase, $CaTa_2O_6$, was identified, which was first observed in the reduced samples. This Ta-rich phase caused more marokite to be formed.
- The electrical conductivity increased with increasing temperature and decreased with increasing amount of marokite, due to marokite's extremely low conductivity.
- Seebeck coefficient values are negative and they decreased in absolute value with increasing temperature. This confirms that CMTO is an n-type semiconductor.
- The thermal conductivity decreased with increasing amount of secondary phase, due to additional interfaces and the relatively low thermal conductivity of marokite compared to

the main $CaMnO_3$-phase. The obtained grain sizes were not in the nanosize scale, hence, the effect on thermal conductivity is small and a reduction with reduced grain size was not observed.

- Highest figure of merit (zT) was obtained in the sample with highest electrical conductivity at temperatures in the TE oxide application range 500°C to 800°C. Hence, it is important to obtain high electrical conductivity to achieve high zT.

- The amount of the insulating marokite should be reduced in order to enhance the power factor (PF). However, as secondary phases result in additional phonon scattering agents, some marokite in the structure is desired, and an optimized vol% needs be pursued. Further, the thermal conductivity should be lowered to enhance zT. Taking the sample sintered at 850°C as a starting point, since it resulted in the smallest grains after SPS, grains in the nanorange could be achieved by optimizing the annealing program in terms of lowering the annealing temperature.

Bibliography

[1] J. He, Y. Liu, and R. Funahashi, "Oxide thermoelectrics: The challenges, progress, and outlook," *Journal of Materials Research*, vol. 26, no. 15, pp. 1762–1772, 2011.

[2] J. W. Fergus, "Oxide materials for high temperature thermoelectric energy conversion," *Journal of the European Ceramic Society*, vol. 32, no. 3, pp. 525–540, 2012.

[3] G. J. Snyder and E. S. Toberer, "Complex thermoelectric materials," *Nature materials*, vol. 7, no. 2, pp. 105–114, 2008.

[4] D. M. Rowe, *Modules, systems, and applications in thermoelectrics*. CRC Press, 2012, vol. 2.

[5] D. D. Pollock, *Thermoelectricity: Theory, thermometry, tool*. ASTM International, 1985, no. 852.

[6] W. R. Fahrner and S. Schwertheim, *Semiconductor thermoelectric generators*. Trans Tech Publ., 2009.

[7] D. M. Rowe, *Thermoelectrics handbook: macro to nano*. CRC Press, 2005, ch. General principles and basic consideration, pp. 1–14.

[8] H. J. Goldsmid, *Introduction to thermoelectricity*. Springer, 2010, vol. 121.

[9] L. Bocher, "Synthesis, structure, microstructure, and thermoelectric properties of perovskite-type manganate phases," Ph.D. dissertation, University of Augsburg, 2009.

[10] N. M. Mazur, "Microstructural design of $CaMnO_3$ and its thermoelectric properties," Master's thesis, Norwegian University of Science and Technology, 2015.

[11] M. Ohtaki, "Recent aspects of oxide thermoelectric materials for power generation from mid-to-high temperature heat source," *Journal of the Ceramic Society of Japan*, vol. 119, no. 1395, pp. 770–775, 2011.

[12] C. Kittel, *Introduction to Solid State Physics*, 8th ed. John Wiley & Sons, Inc, 2005.

[13] J. P. Doumerc, M. Blangero, M. Pollet, D. Carlier, J. Darriet, R. Berthelot, C. Delmas, and R. Decourt, "Transition-metal oxides for thermoelectric generation," *Journal of electronic materials*, vol. 38, no. 7, pp. 1078–1082, 2009.

[14] S. Hebert and A. Maignan, *Functional oxides*. John Wiley & Sons, 2011, vol. 12, ch. Thermoelectric Oxides, pp. 203–252.

[15] D. T. Crane and L. E. Bell, "Design to maximize performance of a thermoelectric power generator with a dynamic thermal power source," *Journal of Energy Resources Technology*, vol. 131, no. 1, p. 012401, 2009.

[16] M. Schrade, R. Kabir, S. Li, T. Norby, and T. Finstad, "High temperature transport properties of thermoelectric CaMnO3-δ—indication of strongly interacting small polarons," *Journal of Applied Physics*, vol. 115, no. 10, 2014.

[17] H. S. Horowitz and J. M. Longo, "Phase relations in the Ca–Mn–O system," *Materials Research Bulletin*, vol. 13, no. 12, pp. 1359–1369, 1978.

[18] S. E. Olsen, S. Olsen, M. Tangstad, and T. Lindstad., *Production of manganese ferroalloys*. Tapir Academic Press, 2007.

[19] H. Taguchi, M. Nagao, T. Sato, and M. Shimada, "High-temperature phase transition of $CaMnO_{3-\delta}$," *Journal of Solid State Chemistry*, vol. 78, no. 2, pp. 312–315, 1989.

[20] M. Molinari, D. A. Tompsett, S. C. Parker, F. Azough, and R. Freer, "Structural, electronic and thermoelectric behaviour of CaMnO3 and CaMnO(3- delta)," *Journal of Materials Chemistry A*, vol. 2, no. 34, pp. 14 109–14 117, 2014.

[21] J. Du, T. Zhang, F. Cheng, W. Chu, Z. Wu, and J. Chen, "Nonstoichiometric perovskite $CaMnO_{3-\delta}$ for oxygen electrocatalysis with high activity," *Inorganic chemistry*, vol. 53, no. 17, pp. 9106–9114, 2014.

[22] L. Bocher, M. Aguirre, D. Logvinovich, A. Shkabko, R. Robert, M. Trottmann, and A. Weidenkaff, "$CaMn_{1-x}Nb_xO_3$ (x<0.08) perovskite-type phases as promising new high-temperature n-type thermoelectric materials," *Inorganic chemistry*, vol. 47, no. 18, pp. 8077–8085, 2008.

[23] D. Richerson, D. W. Richerson, and W. E. Lee, *Modern ceramic engineering: properties, processing, and use in design*, 3rd ed. CRC press, 2005.

[24] M. M. Jorge, A. C. dos Santos, and M. Nunes, "Effects of synthesis method on stoichiometry, structure and electrical conductivity of CaMnO(3- δ)," *International Journal of Inorganic Materials*, vol. 3, no. 7, pp. 915–921, 2001.

[25] K. Ledezma, "Sintering and thermoelectric properties of CMTO Ca(0.931)Mn(0.98)Ta(0.02)O(3-δ)," NTNU, Tech. Rep., 2016.

[26] R. Kabir, T. Zhang, D. Wang, R. Donelson, R. Tian, T. T. Tan, and S. Li, "Improvement in the thermoelectric properties of CaMnO3 perovskites by w doping," *Journal of Materials Science*, vol. 49, no. 21, pp. 7522–7528, 2014.

[27] G. Xu, R. Funahashi, Q. Pu, B. Liu, R. Tao, G. Wang, and Z. Ding, "High-temperature transport properties of nb and ta substituted CaMnO3 system," *Solid State Ionics*, vol. 171, no. 1, pp. 147–151, 2004.

[28] Y. Zhou, I. Matsubara, R. Funahashi, G. Xu, and M. Shikano, "Influence of Mn-site doped with ru on the high-temperature thermoelectric performance of CaMnO3-delta," *Materials research bulletin*, vol. 38, no. 2, pp. 341–346, 2003.

[29] P. Thiel, S. Populoh, S. Yoon, G. Saucke, K. Rubenis, and A. Weidenkaff, "Charge-carrier hopping in highly conductive $CaMn_{1-x}M_xO_{3-\delta}$ thermoelectrics," *The Journal of Physical Chemistry C*, vol. 119, no. 38, pp. 21 860–21 867, 2015.

[30] Y. Wang, K. Fujinami, R. Zhang, C. Wan, N. Wang, Y. Ba, and K. Koumoto, "Interfacial thermal resistance and thermal conductivity in nanograined SrTiO3," *Applied physics express*, vol. 3, no. 3, p. 031101, 2010.

[31] B. Murty, P. Shankar, B. Raj, B. Rath, and J. Murday, *Textbook of Nanoscience and Nanotechnology*. Springer & Universities Press, 2013.

[32] K. Koumoto, Y. Wang, R. Zhang, A. Kosuga, and R. Funahashi, "Oxide thermoelectric materials: a nanostructuring approach," *Annual review of materials research*, vol. 40, pp. 363–394, 2010.

[33] T. E. Loland, J. Sele, M.-A. Einarsrud, P. E. Vullum, M. Johnsson, and K. Wiik, "Thermal conductivity of A-site cation-deficient la-substituted SrTiO3 produced by spark plasma sintering," *Energy Harvesting and Systems*, vol. 2, no. 1-2, pp. 63–71, 2015.

[34] J. Lan, Y.-H. Lin, H. Fang, A. Mei, C.-W. Nan, Y. Liu, S. Xu, and M. Peters, "High-temperature thermoelectric behaviors of fine-grained Gd-doped CaMnO3 ceramics," *Journal of the American Ceramic Society*, vol. 93, no. 8, pp. 2121–2124, 2010.

[35] B. F. Donovan, B. M. Foley, J. F. Ihlefeld, J.-P. Maria, and P. E. Hopkins, "Spectral phonon scattering effects on the thermal conductivity of nano-grained barium titanate," *Applied Physics Letters*, vol. 105, no. 8, p. 082907, 2014.

[36] C. Wan, Y. Wang, N. Wang, W. Norimatsu, M. Kusunoki, and K. Koumoto, "Development of novel thermoelectric materials by reduction of lattice thermal conductivity," *Science and Technology of Advanced Materials*, vol. 11, 2010.

[37] S. P. Singh, "Development of n-type oxide TE-materials," Ph.D. dissertation, Norwegian university of science and technology (NTNU), 2017, to be published November 2017.

[38] J. Zagorac, A. Zarubica, A. Radosavljevic-Mihajlovic, D. Zagorac, and B. Matovic, "Structural study of nanosized yttrium-doped $CaMnO_3$ perovskites," *Bulletin of Materials Science*, vol. 37, no. 3, pp. 407–416, 2014.

[39] B. White, J. Souza, C. Chiorescu, J. Neumeier, and J. Cohn, "Magnetic, transport, and thermodynamic properties of $CaMn_2O_4$ single crystals," *Physical Review B*, vol. 79, no. 10, p. 104427, 2009.

[40] P. Villars, "Springer materials, CaMn2O4 crystal structure," http://materials.springer.com/isp/crystallographic/docs/sd_1810135, accessed: 2017-03-28.

[41] K. Takahashi, H. Yamamura, K. Muramatsu, S.-i. Shirasaki, and K. Suehiro, "A new phase of compound $CaMnO_{2+\delta}$," *Bulletin of the Chemical Society of Japan*, vol. 55, no. 2, pp. 619–620, 1982.

[42] R. Shannon, "Database of ionic radii," Revised Effective Ionic Radii and Systematic Studies of Interatomic Distances in Halides and Chalcogenides, Acta Cryst. A32 751-767„ 1976, accessed: 2017-02-27. [Online]. Available: http://abulafia.mt.ic.ac.uk/shannon/ptable.php

[43] P. Villars, "Springer and material phases data system, Ca0.5Mn0.5O," http://materials.springer.com/isp/crystallographic/docs/sd_1500211, accessed: 2017-03-28.

[44] A. Varela, S. d. Dios, M. Parras, M. Hernando, M. T. Fernandez-Diaz, A. R. Landa-Cánovas, and J. M. González-Calbet, "Ordered rock-salt related nanoclusters in CaMnO2," *Journal of the American Chemical Society*, vol. 131, no. 24, pp. 8660–8668, 2009.

[45] A. Reller, G. Davoodabady, and H. Oswald, "Reversible topotactic reduction of perovskite-related calcium manganese oxides," *Thermochimica Acta*, vol. 83, no. 1, pp. 121–124, 1985.

[46] C. Bréchignac, P. Houdy, and M. Lahmani, *Nanomaterials and nanochemistry*. Springer Science & Business Media, 2008, ch. Bulk Nanostructured Materials Obtained by Powder Sintering, pp. 489–495.

[47] J. G. Noudem, D. Kenfaui, S. Quetel-Weben, C. S. Sanmathi, R. Retoux, and M. Gomina, "Spark plasma sintering of n-type thermoelectric Ca0.95Sm0.05MnO3," *Journal of the American Ceramic Society*, vol. 94, no. 8, pp. 2608–2612, 2011.

[48] Z. Shen, M. Johnsson, Z. Zhao, and M. Nygren, "Spark plasma sintering of alumina," *Journal of the American Ceramic Society*, vol. 85, no. 8, pp. 1921–1927, 2002.

[49] M. Tokita, "Trends in advanded SPS systems and FGM technology," in *NEDO International Symposium on Functionallly Graded Materials. ToKyo: Mielparque*, vol. 23, 1999.

[50] S. Labonnote-Weber, "Re: Camta-powder," E-mail, Nov. 2016.

[51] CerPoTechAS, "CerPoTech, about us," http://www.cerpotech.com, accessed: 2016-11-01.

[52] "Bruker eva software," https://www.bruker.com/products/x-ray-diffraction-and-elemental-analysis/x-ray-diffraction/xrd-software/overview/eva.html., accessed: 2017-05-18.

[53] "Bruker topas software," https://www.bruker.com/products/x-ray-diffraction-and-elemental-analysis/x-ray-diffraction/xrd-software/topas.html, accessed: 2016-12-10.

[54] W. Parker, R. Jenkins, C. Butler, and G. Abbott, "Flash method of determining thermal diffusivity, heat capacity, and thermal conductivity," *Journal of applied physics*, vol. 32, no. 9, pp. 1679–1684, 1961.

[55] P. Thiel, J. Eilertsen, S. Populoh, G. Saucke, M. Döbeli, A. Shkabko, L. Sagarna, L. Karvonen, and A. Weidenkaff, "Influence of tungsten substitution and oxygen deficiency on the thermoelectric properties of $CaMnO_{3-\delta}$," *Journal of Applied Physics*, vol. 114, no. 24, p. 243707, 2013.

[56] P. Scardi, M. Leoni, and R. Delhez, "Line broadening analysis using integral breadth methods: a critical review," *Journal of Applied Crystallography*, vol. 37, no. 3, pp. 381–390, 2004.

[57] L. Bocher, M. H. Aguirre, R. Robert, D. Logvinovich, S. Bakardjieva, J. Hejtmanek, and A. Weidenkaff, "High-temperature stability, structure and thermoelectric properties of CaMn(1-x)NbxO3 phases," *Acta Materialia*, vol. 57, no. 19, pp. 5667–5680, 2009.

[58] P. Villars, "Springer and material phases data system, CaTa2O6," http://materials.springer.com/isp/crystallographic/docs/sd_2060479, accessed: 2017-03-28.

[59] ——, "Springer materials, CaMnO3 crystal structure," http://materials.springer.com/isp/crystallographic/docs/sd_1621032, accessed: 2017-03-28.

[60] Y.-B. Kang, I.-H. Jung, S. A. Decterov, A. D. Pelton, and H.-G. Lee, “Critical thermodynamic evaluation and optimization of the CaO-MnO-SiO2 and CaO-MnO-Al2O3 systems,” *ISIJ international*, vol. 44, no. 6, pp. 965–974, 2004.

A | List of symbols and abbreviations

Roman symbols

Symbol	Description
A	Cross-sectional area
C_v	Heat capacity at constant volume
d	Sample thickness
D	Particle diameter
e	Electron charge
h	Planc's constant
I	Electric current
k_B	Boltzman's constant
l	Phonon mean free path (Eq.2.13)
l	Distance between voltage probes (Eq.3.2)
L	Lorentz number
m*	Effective carrier mass
n	Charge carrier concentration
S	Seebeck coefficient
$t_{1/2}$	Half-time
T	Temperature
T_h	Temperature at hot end
T_c	Temperature at cold end
V	Voltage drop
zT	Dimensionless thermoelectric figure of merit

Greek symbols

Symbol	Description
α	Thermal diffusivity
β	Thomson coefficient
κ	Total thermal conductivity
$\kappa_e l$	Electronic thermal conductivity
κ_l	Lattice thermal conductivity
μ	Carrier mobility
ν	Average phonon velocity
Π	Peltier coefficient
Π_{closed}	Closed porosity
Π_{open}	Open porosity
Π_{true}	True porosity
ρ	Electrical resistivity (Eq.2.10)
ρ	Density
ρ_t	Theoretical density
ρ_{bulk}	Bulk density of material
ρ_{liq}	Density of isopropanol
ρ_{rel}	Relative density in %
σ	Electrical conductivity

Abbreviations

Abbreviation	Description
BSE	Backscatter electron microscopy
CMO	Calcium Manganite $CaMnO_3$
DIL	Dilatometry
EDS	Energy dispersive spectrocopy
Eq.	Equation
Fig.	Figure
PF	Power factor
SEM	Scanning electron microscopy
tc	Thermocouple
TE	Thermoelectric
TEC	Thermal expansion coefficient
TGA	Thermogravimetric analysis
XRD	X-ray diffraction

B | Sintering properties of CMTO

DIL–analysis was conducted to investigate sintering properties of as-received CMTO. The obtained sintering curve is presented in Fig.B.1, and indicates that the sintering process begins at around 930°C, where the material starts to shrink. The highest shrinkage rate is between 1150°C and 1160°C. This analysis was carried out during specialization project fall 2016.[25]

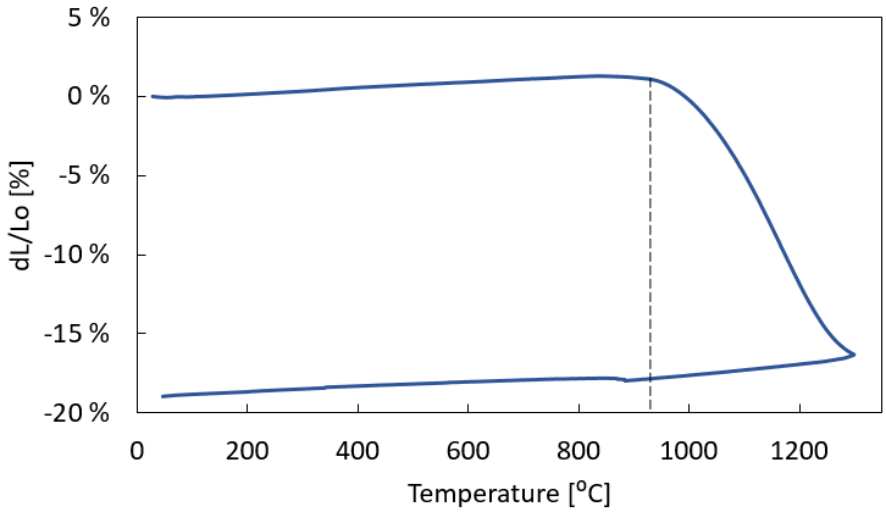

Figure B.1: Investigation of sintering properties of the CMTO powder. DIL–measurement in air with 1300 °C as maximum temperature, and heating- and cooling rate 2°C/min. The densification begins at around 930°C, marked with a dotted line.[25]

C | Archimedes' method

Archimedes method was used to measure the density and porosity of the sintered samples by using the following equations.

The density of the liquid is found from the density-temperature correlation:

$$\rho_{liq} = -0.0009T + 0.8018 \tag{C.1}$$

where T is temperature in °C.

By relating the obtained masses to sample buoyancy and the density of the liquid, bulk density and porosity can be calculated. The bulk porosity, ρ_{bulk}, was found from Eq.C.2, where m_1 is the weight of dry pellet, m_2 is the weight of immersed pellet and m_3 is wet pellet removed from the isopropanol.

$$\rho_{bulk} = \frac{m_1}{m_3 - m_2} \cdot \rho_{liq} \tag{C.2}$$

Open porosity, true porosity and closed porosity were calculated by following equations, respectively, where ρ_t is the theoretical density of CMTO (4.70 g/cm^3[29]) or of the reduced rock-salt phase (4.35 g/cm^3[43].:

$$\pi_{open} = \frac{m_3 - m_1}{m_3 - m_2} \cdot 100 \tag{C.3}$$

$$\pi_{true} = \frac{\rho_t - \rho_{liq}}{\rho_t} \cdot 100 \tag{C.4}$$

$$\pi_{closed} = \pi_{true} - \pi_{open} \tag{C.5}$$

D | Numerical values and calculations

Theoretical densities were calculated through rule of mixture:

$$\rho_{red} = \rho_{Ca(0.5)Mn(0.5)O} V_{Ca(0.5)Mn(0.5)O} + \rho_{CaTa2O6} V_{CaTa2O} \tag{D.1}$$

$$\rho_{ox} = \rho_{CMTO} V_{CMTO} + \rho_{CaMn2O4} V_{CaMn2O4} \tag{D.2}$$

where ρ_{red} is the theoretical density of the reduced material with rock-salt structure, $\rho_{Ca(0.5)Mn(0.5)O/CaTa2O6}$ and $V_{Ca(0.5)Mn(0.5)O/CaTa2O6}$ is the theoretical density and volume fraction, respectively, of either $Ca_{0.5}Mn_{0.5}O$ or $CaTa_2O_6$. ρ_{ox} is the theoretical density of the oxidized material with perovskite structure and a secondary spinel phase, and $\rho_{CMTO/CaMn2O4}$ and $V_{CMTO/CaMn2O4}$ is the theoretical density and volume fraction, respectively, of either $CaMn_{0.98}Ta_{0.02}O_3$ or $CaMn_2O_4$. Calculated values are presented in Tab.D.1 Theoretical densities of pure materials are presented in Tab.D.2.

Table D.1: Calculated theoretical densities of two-phase materials, with given amount of secondary phase. Reduced = $Ca_{0.5}Mn_{0.5}O$ + $CaTa_2O_6$, Oxidized = CMTO + $CaMn_2O_4$

Material	Reduced (ρ_{red})	Oxidized (ρ_{ox})
Vol% secondary phase	2	20
Theoretical densiy [g/cm^3]	4.354	4.696

Table D.2: Theoretical densities of single-phase materials used in the calculations.

Material	$Ca_{0.5}Mn_{0.5}O$	$CaTa_2O_6$	CMTO	$CaMnO_3$	$CaMn_2O_4$
Theoretical densiy [g/cm^3]	4.25[43]	7.02[58]	4.70[29]	4.58[59]	4.68[40]

Tab.D.3 and Tab.D.4 give information about structure and values for molar volumes, respectively.

Table D.3: Information about unit cell and structure of the discussed materials. From XRD-results and Eva Software.

Material	Unit cell vol. [Å^3]	Crystal structure	PDF-file
$Ca_{0.5}Mn_{0.5}O$	99.25	Rock-salt	04-007-8378
$CaTa_2O_6$	470.9	Cubic	00-036-0805
$CaMnO_3$	207.2	Perovskite	04-014-8192
$CaMn_2O_4$	303.6	Spinel	04-015-3975

Table D.4: Molar volumes calculated from theoretical density and molar mass.

Material	$Ca_{0.5}Mn_{0.5}O$	CMTO	$CaMnO_3$	$CaMn_2O_4$
Molar volume [cm^3/mol]	14.94	30.95	31.22	45.72

E | Thermal etching

In order to study grain boundaries at the surface of the sintered samples, thermal etching was required. Different heating programs were investigated, which is why the samples sintered at 850°C, 950°C and 1250°C have dwell time of four hours, while for the remaining three samples a dwell time of 30 minutes was applied, as presented in Fig.E.1. Four hours dwell time resulted in over-etched surfaces.

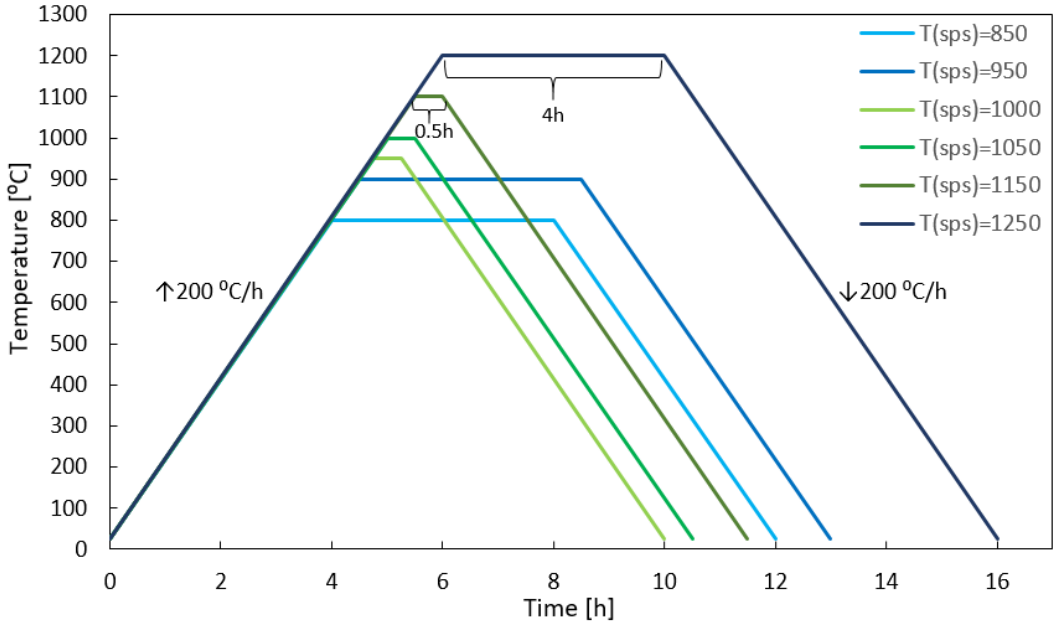

Figure E.1: The heating program used to thermally etch the sintered samples. Each curve represents a sample, and the sintering temperature is given in the figure. For three samples 4 hours dwell time was applied. For the three other samples the dwell time was set to 30 minutes.

F | Additional DIL measurement

DIL measurements were conducted to investigate oxidation properties of $Ca_{0.5}Mn_{0.5}O$. Fig.F.1 shows the result of the analysis conducted on the sample sintered at 950°C.

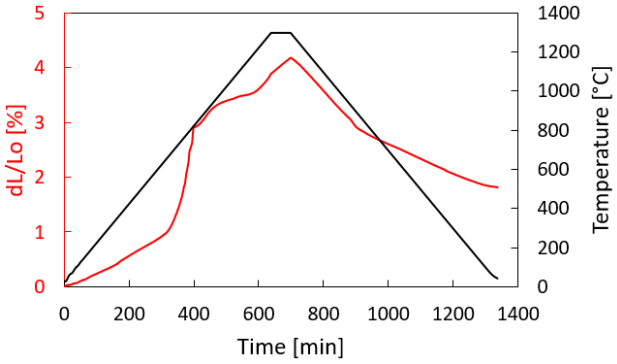

(a) T_{sps}=950°C

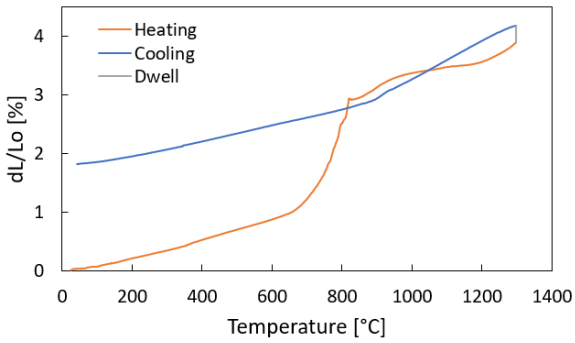

(b) T_{sps}=950°C

Figure F.1: Investigation of oxidizing properties of the sintered rock-salt structure. DIL–analysis in air with 1300 °C as maximum temperature, heating- and cooling rate 2°C/min, and 1h dwell time. The sample analyzed was sintered at 950°C and was highly dense.

G | EDS line scans

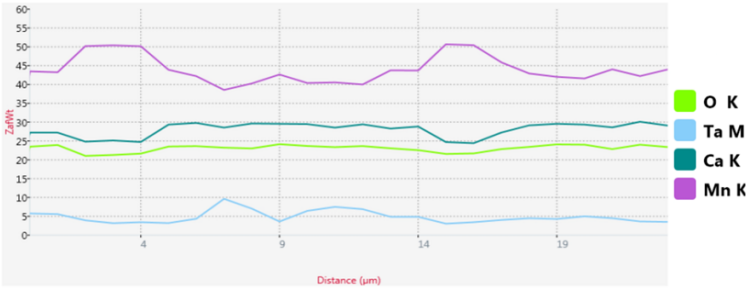

(a) T_{sps}=850°C.

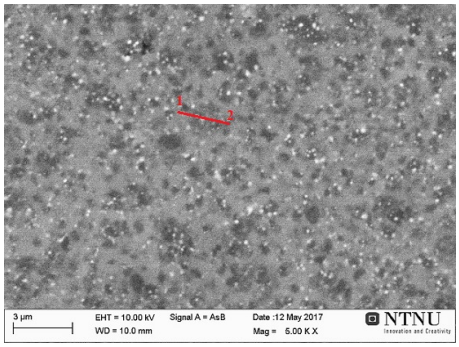

(b) T_{sps}=850°C.

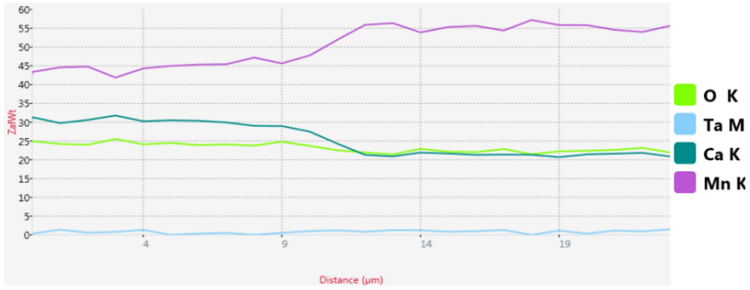

(c) T_{sps}=950°C.

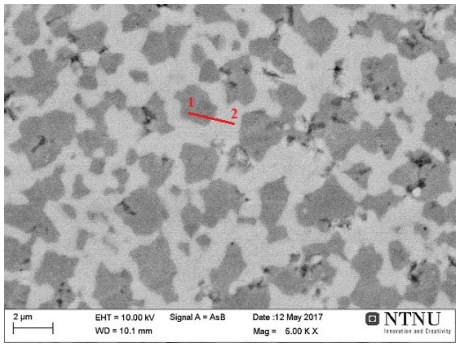

(d) T_{sps}=950°C.

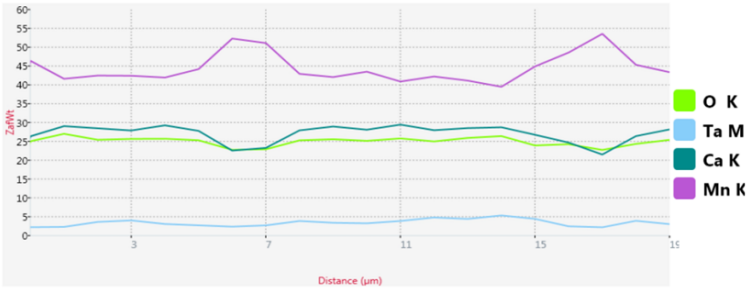

(e) T_{sps}=1000°C.

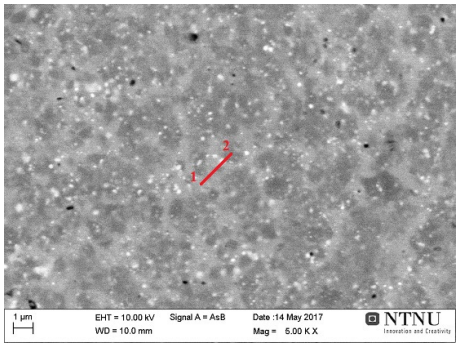

(f) T_{sps}=1000°C.

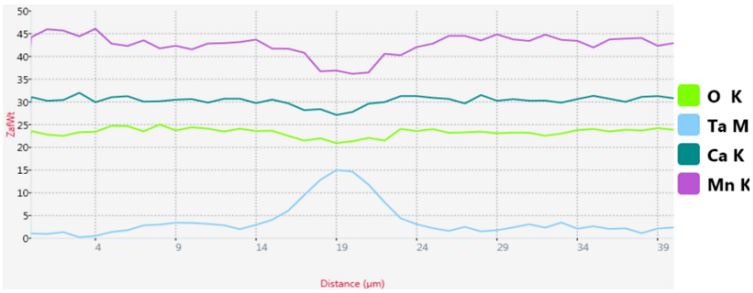

(g) T_{sps}=1150°C.

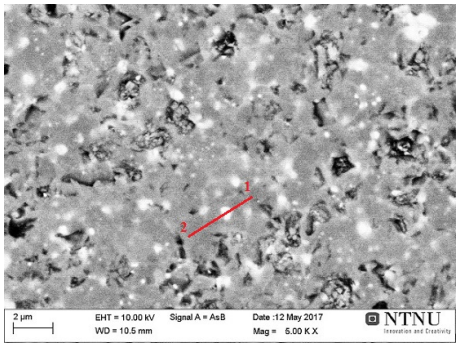

(h) T_{sps}=1150°C.

Figure G.1: Element profile plots from EDS line scans of polished samples. Analysis is performed along red line marked in the SEM images. Sintering temperature is given i each image.

H | Additional phase diagram

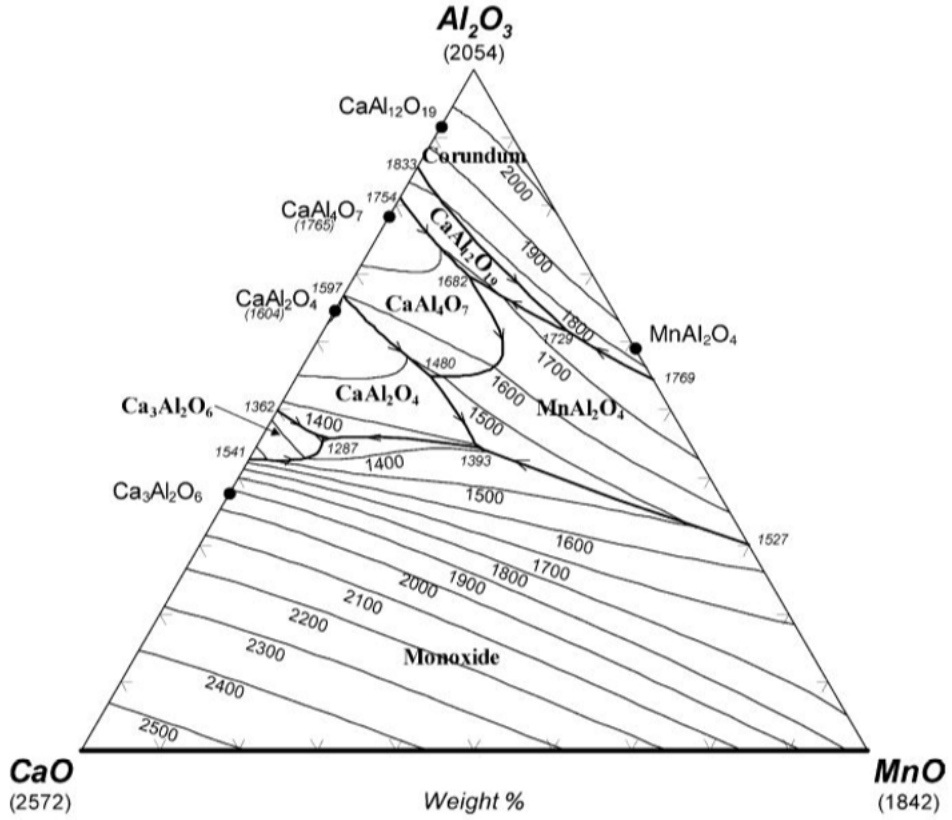

Figure H.1: CaO-MnO-Al_2O_3 phase diagram[60]

I | Electrical conductivity and Seebeck data

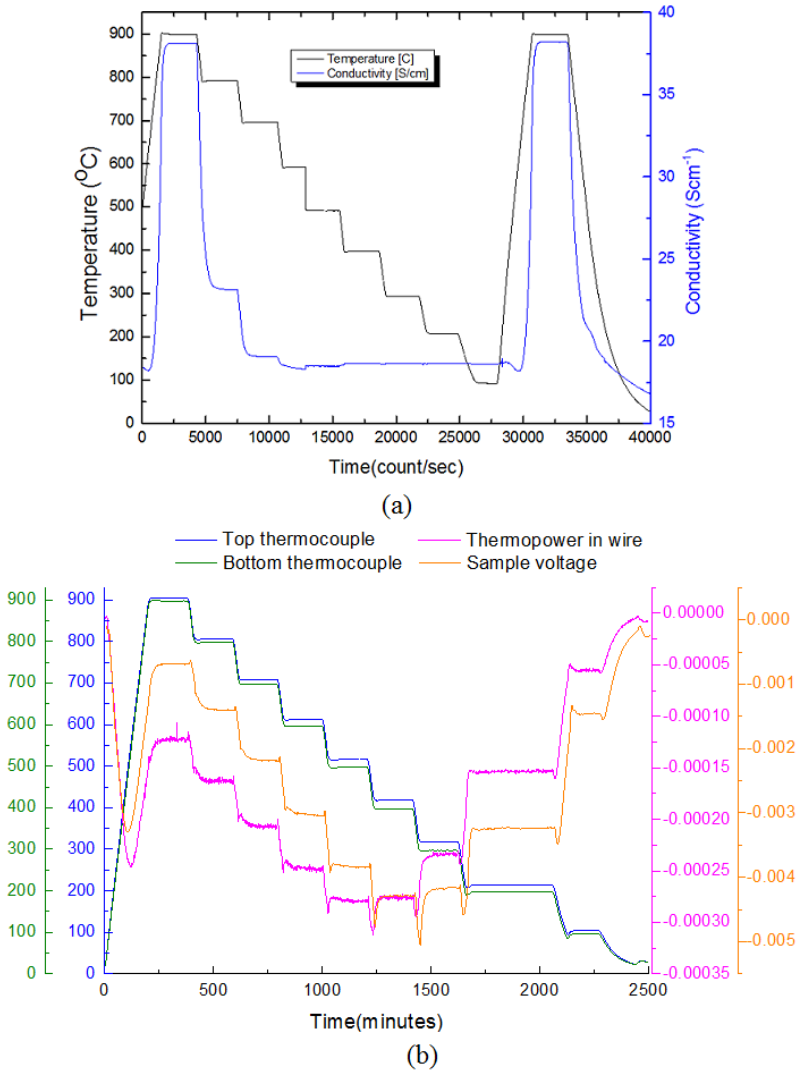

Figure I.1: (a) Complete dataset from electrical conductivity measurement (blue) including temperature program (black). (b) Complete curves from the Seebeck measurement, including temperature program (blue and green), thermopower in wire (pink) and sample voltage (orange).

J | Grain size from XRD and SEM

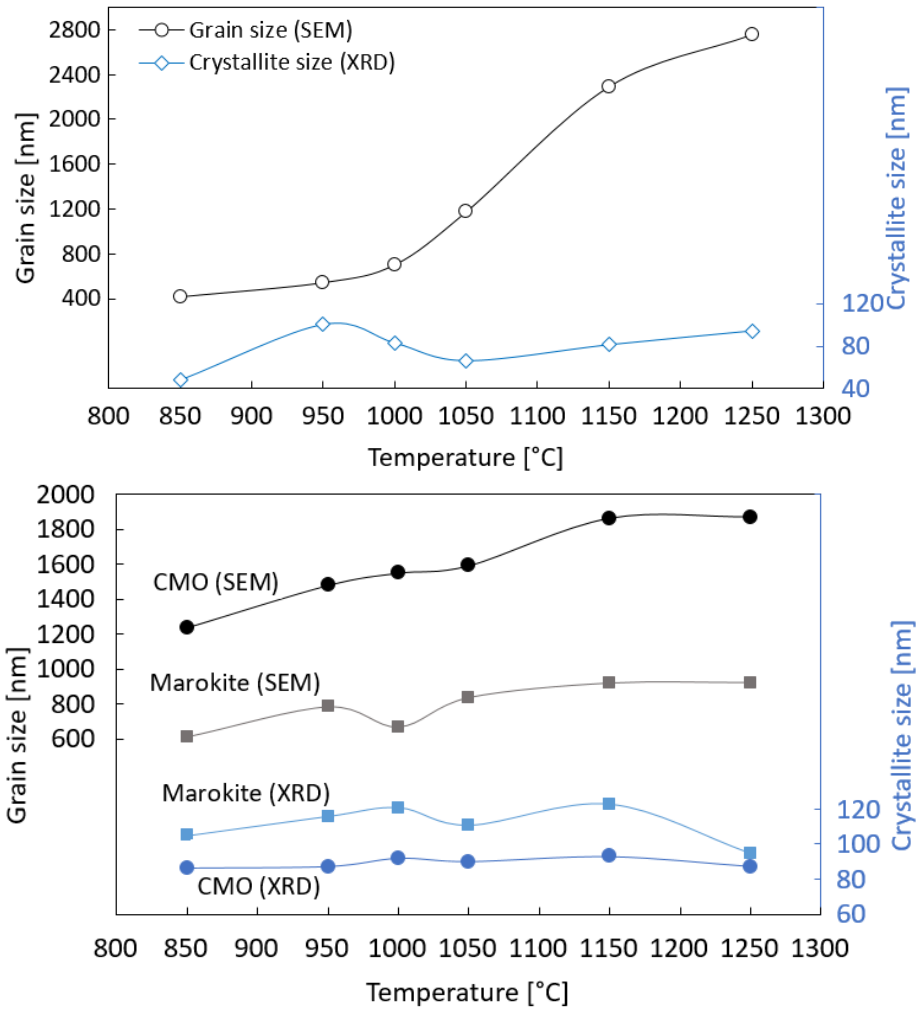

Figure J.1: (a) as-sintered samples. (b) Oxidized samples. Average grain sizes as a function of sintering temperature. Comparison of grain size estimated from SEM images (black and grey ponits) and crystallize size reported from Debye-Scherrer (blue points). Grain size based on SEM-images on primary y-axis, and grain size calculated from XRD-results on secondary y-axis.